3-23-2018

Two-Photon Excitation of Cesium Alkali Metal Vapor 7^2D, 8^2D Kinetics and Spectroscopy

Ricardo C. Davila

TWO-PHOTON EXCITATION OF CESIUM ALKALI METAL VAPOR

7^2D, 8^2D KINETICS AND SPECTROSCOPY

DISSERTATION

Ricardo C. Davila, Civilian, USAF

AFIT-ENP-DS-18-M-076

DEPARTMENT OF THE AIR FORCE
AIR UNIVERSITY

AIR FORCE INSTITUTE OF TECHNOLOGY

Wright-Patterson Air Force Base, Ohio

The views expressed in this dissertation are those of the author and do not reflect the official policy or position of the United States Air Force, the Department of Defense, or the United States Government.

AFIT-ENP-DS-18-M-076

TWO-PHOTON EXCITATION OF CESIUM ALKALI METAL VAPOR 7^2D, 8^2D KINETICS AND SPECTROSCOPY

DISSERTATION

Presented to the Faculty

Graduate School of Engineering and Management

Air Force Institute of Technology

Air University

Air Education and Training Command

in Partial Fulfillment of the Requirements for the

Degree of Doctorate of Philosophy in Engineering Physics

Ricardo C. Davila, M.S.

Civilian, USAF

March 2018

AFIT-ENP-DS-18-M-076

TWO-PHOTON EXCITATION OF CESIUM ALKALI METAL VAPOR 7^2D, 8^2D KINETICS AND SPECTROSCOPY

Ricardo C. Davila, M.S.
Civilian, USAF

Committee Membership:

Glen P. Perram, PhD
Chairman

Kevin C. Gross, PhD
Member

Mark E. Oxley, PhD
Member

ADEDJI B. BADIRU, PhD
Dean, Graduate School of Engineering
and Management

Abstract

Pulsed excitation on the two-photon Cs $6^2S_{1/2} \rightarrow 7^2D_{3/2,5/2}$ transition results in time-resolved fluorescence at 697 *nm* and 672 *nm*. The rates for fine structure mixing between the $7^2D_{3/2,5/2}$ states have been measured for helium and argon rare gas collision partners. The mixing rates are very fast, $1.26 \pm 0.05 \times 10^{-9}$ $cm^3/(atom\ sec)$ for He and $1.52 \pm 0.05 \times 10^{-10}$ $cm^3/(atom\ sec)$ for Ar, driven by the small energy splitting and large radial distribution for the valence electron. The quenching rates are considerably slower, $6.84 \pm 0.09 \times 10^{-11}$ $cm^3/(atom\ sec)$ and $2.65 \pm 0.04 \times 10^{-11}$ $cm^3/(atom\ sec)$ for He and Ar, respectively. The current results are placed in context with similar rates for other alkali-rare gas collision pairs using adiabaticity arguments.

Pulsed excitation on the two-photon Cs $6\,^2S_{1/2} \rightarrow 8\,^2D_{3/2,5/2}$ transition results in time-resolved fluorescence at 601 *nm*. The rates for fine structure mixing between the $8\,^2D_{3/2,5/2}$ states have been measured for helium and argon rare gas collision partners. The mixing rates are very fast, $2.6 \pm 0.2 \times 10^{-9}$ $cm^3/(atom\ s)$ for He and $5.2 \pm 0.4 \times 10^{-10}$ $cm^3/(atom\ s)$ for Ar, about 2-3 times faster than for the Cs $7\,^2D_{5/2} \rightleftharpoons 7\,^2D_{3/2}$ relaxation. The quenching rates are also rapid, $1.07 \pm 0.04 \times 10^{-10}$ $cm^3/(atom\ s)$ and $9.5 \pm 0.7 \times 10^{-11}$ $cm^3/(atom\ s)$ for He and Ar, respectively. The rapid fine structure rates are explained by the highly impulsive nature of the collisions and the large average distance of the valence electron from the nucleus. Quenching rates (inter-multiplet transfer) are likely enhanced by the closely spaced, $9\,^2P$ levels.

Stimulated emission on the ultraviolet and blue transitions in Cs has been achieved by pumping via two-photon absorption for the pump transition $6^2S_{1/2} \rightarrow 7^2D_{5/2,3/2}$. The performance of the optically-pumped cesium vapor laser operating in ultraviolet and blue has been extended to 650 nJ/pulse for 387 nm, 1.3 μJ/pulse for 388 nm, 200 nJ/pulse for 455 nm and 500 nJ/pulse for 459 nm. Emission performance improves dramatically as the

cesium vapor density is increased and no scaling limitations associated with energy pooling or ionization kinetics have been observed.

Acknowledgments

First, I would like to thank my wife and daughter for putting up with me during the many hours I spent on course work, research and work demands. Balancing work and family time is not my forte; but, it's my family's support and encouragement that keeps me going each day.

Second, my mother, father and brother are role models – I can't thank them enough for the parts they played in my upbringing and encouragement they continue to provide today.

Third, I received assistance and friendship from the AFIT laser research team (Capt Wooddy Miller, Ben Eshel, Capt Nate Haluska, Capt. AJ Wallerstein, and Capt Bill Bauer) and my AFRL leadership and co-workers. Many thanks to AFIT ENP's lab techs, Greg Smith and Mike Ranft, for all their support and special kudos to Chris Rice and Aaron Archibald, whose assistance in my experimental configurations was critical. It was Aaron's optical bench setup that allowed me to work my two spin-orbit rate experiments.

Fourth, I appreciate the help I received from my committee members. Dr Kevin Gross and Dr Mark Oxley were my professors for quantum physics, spectroscopy and mathematics. I enjoyed your courses and your teaching styles. Thank you for giving me a deeper appreciation of physics and math.

Finally, I would like to thank Dr. Glen Perram. I can't thank you enough for your patience, mentorship and advisement. I'm glad our paths continue to cross in my current AFRL work.

Ricardo C. Davila

Table of Contents

Page

List of Figures

List of Tables

List of Symbols

Symbol Page

TWO-PHOTON EXCITATION OF CESIUM ALKALI METAL VAPOR

7^2D, 8^2D KINETICS AND SPECTROSCOPY

I. Introduction

Diode Pumped Alkali Lasers (DPALs) combined approach for high power and multi-wavelength output offer a unique benefit to military applications, to include laser weapons, not found in other laser systems [95]. Diode laser bars are used to pump the D_2 (historical designation for DPAL pump transition) $^2S_{1/2} \rightarrow^2 P_{3/2}$, and collisional energy transfer to the spin-orbit split $^2P_{1/2}$ energy state leads to lasing on the D_1 (historical designation for DPAL lasing transition) $^2P_{1/2} \rightarrow^2 S_{1/2}$ transition in potassium (K), rubidium (Rb), or cesium (Cs) vapor [102]. A rubidium DPAL was first demonstrated in 2003 [72] and in less than 10 years, these laser systems have been scaled to kilowatt power levels [15, 102], analytic lasing models have been developed [47, 48, 135] and operating DPAL wavelengths have been verified to span the atmospheric transmission window [101, 106].

For DPAL lasing on the D_1 $^2P_{1/2} \rightarrow^2 S_{1/2}$ transition, scaling output power and system efficiency depend on pump sources that closely match the center wavelength of the alkali D_2 transition to efficiently couple to the spectrally narrow bandwidth of the atomic transitions and sufficient pump intensity to bleach ground state alkali atoms to achieve an optical gain-to-loss ratio within the laser cavity to lase on the D_1 transition [71]. Additionally, rapid collision-induced spin-orbit mixing between the $^2P_{1/2,3/2}$ fine structure states is critical to prevent bottlenecking of the laser cycle [71] and mixing rates for the first excited $^2P_{1/2,3/2}$ states for K, Rb and Cs haven been documented in the literature [41, 66, 99]. Mixing cycle times of 74 ps were reported in potassium using helium as the rare gas collision partner, 380 times faster than the D_1, $4P_{1/2} \rightarrow 4S_{1/2}$, radiative lifetime [54]. Spin-orbit

mixing rates induced by rare gases are smaller in Rb, requiring higher pressures, from 10 atm [131] up to 25 atm for Rb-Helium (He) [9]. For Cs, the spin-orbit mixing rates are smaller and require hydrocarbon buffer gas [15, 65, 128] to provide sufficient population transfer between Cs $6P_{3/2} \rightleftarrows 6P_{1/2}$. While hydrocarbons have shown promising results as a buffer gas due to their high spin-orbit mixing and low quenching cross sections, under certain conditions, these gases can break down leaving deposits on cell windows resulting in poor beam quality [145]. A key assessment of the DPAL system performance requires temperature dependent rate coefficients for fine-structure mixing processes. For this dissertation work, experiments used rare gases He and Argon (Ar) as collision partners with Cs alkali to measure spin-orbit mixing rates and add to and re-validate previous Cs n^2D spin-orbit mixing rate measurements with rare gas collision partners [55, 76, 77].

Measurements of spin-orbit mixing rates of alkali-metal atoms in collisions with rare gases have been ongoing for the past 50 years [10–12, 27, 37, 41, 44, 53, 55, 57, 66, 68, 77, 78, 83, 85, 90, 98, 99, 112, 120, 121, 130, 144]. Recent experimental focus has shifted to measuring higher-lying Rydberg alkali n^2D states and alkali-metal to alkali-metal collisions [12, 31, 53, 55, 76, 77, 108, 123, 125, 130]. Since the 1960s, when alkali spin-orbit mixing rates measurements began in earnest, a key goal which still exists today was to develop a theory and associated first principle physics model that describes the interaction between the two colliding atoms and could predict the sizes of the various cross sections [66]. While theoretical foundations for predicting the cross sections of non-adiabatic collisions are ongoing, recent work using adiabaticity arguments [38] organized alkali spin-orbit cross sections according to trends observed experimentally by Gallagher [41], Krause [66], and Elward-Berry [37]. This study uses these same adiabaticity arguments to explain measured results and extend the alkali adiabaticity database for Cs in [38] to include first-ever spin-orbit mixing rates for Cs $7^2D_{5/2,3/2}$ with He and Ar buffer gases, revalidated Cs $8^2D_{5/2,3/2}$

with these same buffer gases and extend the database to include Cs Rydberg alkali n^2D rare gas collision partners [55, 76, 77].

Optically-pumped alkali vapor lasers have also been developed using single photon excitation of higher lying P-states, stimulated Raman processes, two-photon excitation of alkali S and D states, and electric quadruple excitation on S-D transitions [94]. Using pump sources to excite higher P and D-states in alkali vapors allows exploration of alternative emission wavelengths extending from ultraviolet (UV) to far infrared. Alternative wavelengths from these optically-pumped alkali lasers are desirable for several applications including underwater communication [19, 29, 30, 84, 119], beacons and illuminators [40, 84, 102], and infrared countermeasures [29, 30, 84, 119, 139].

An additional focus area of this research is to explore DPAL's alternate wavelengths in an effort to understand the feasibility of the alkali laser's potential use in an integrated military weapon system [23, 129]. For example, DPAL's high output power and wavelength lasing agility make DPAL a potential laser candidate for an overall directed countermeasure system. This dissertation explores the kinetics and ultraviolet laser dynamics in optically-pumped cesium (Cs) alkali vapor in the excited low-lying D states. This is an additional rationale for focusing on cesium's 7^2D and 8^2D spin-orbit mixing rates (k_{12}, k_{21}) measurements. These two states were chosen given the mid-wave infrared, short-wave infrared, visible and ultraviolet wavelength transitions from the respective excited state back to Cs $6^2S_{1/2}$ ground state. For the ultraviolet laser output, lasing is observed and characterized from the Cs 7^2D state using the two-photon pump transition $6^2S_{1/2} \rightarrow 7^2D_{5/2,3/2}$

There are three research focus areas for this dissertation study. First, pulsed excitation on the two-photon Cs $6^2S_{1/2} \rightarrow 7^2D_{3/2,5/2}$ transition results in time-resolved fluorescence at 697 *nm* and 672 *nm*. The rates for fine structure mixing between the $7^2D_{3/2,5/2}$ states have been measured for helium and argon rare gas collision partners. The mixing rates are

very fast, $1.26 \pm 0.05 \times 10^{-9}$ $cm^3/(atom\ sec)$ for He and $1.52 \pm 0.05 \times 10^{-10}$ $cm^3/(atom\ sec)$ for Ar, driven by the small energy splitting and large radial distribution for the valence electron. The quenching rates are considerably slower, $6.84 \pm 0.09 \times 10^{-11}$ $cm^3/(atom\ sec)$ and $2.65 \pm 0.04 \times 10^{-11}$ $cm^3/(atom\ sec)$ for He and Ar, respectively. The current results are placed in context with similar rates for other alkali-rare gas collision pairs using adiabaticity arguments.

Second, the rates for fine structure mixing and quenching of the moderately excited $8\,^2D_{5/2}$ and $8\,^2D_{3/2}$ states of cesium under collision with argon and the more impulsive helium have been measured using two-photon pulsed excitation and time-resolved fluorescence techniques. The pressure dependence for the eigenvalues of the rate matrix yield very rapid rate coefficients of $2.6\pm0.2\times10^{-9}$ $cm^3/(atom\ s)$ for He and $5.2\pm0.4\times 10^{-10}$ $cm^3/(atom\ s)$ for Ar, are nearly three times faster than for the Cs $7\,^2D_{5/2} \rightleftharpoons 7\,^2D_{3/2}$ relaxation. The quenching rates are also rapid, $1.07 \pm 0.04 \times 10^{-10}$ $cm^3/(atom\ s)$ and $9.5 \pm 0.7 \times 10^{-11}$ $cm^3/(atom\ s)$ for He and Ar, respectively. The rapid fine structure rates are explained by the highly impulsive nature of the collisions and the large average distance of the valence electron from the nucleus. Quenching rates (intra-multiplet transfer) are likely enhanced by the closely spaced, $9\,^2P$ levels. The observed rates are compared with the predictions from time dependent perturbation theory.

Third, stimulated emission on the ultraviolet and blue transitions in Cs has been achieved by pumping via two-photon absorption for the pump transition $6^2S_{1/2} \rightarrow 7^2D_{5/2,3/2}$. The performance of the optically-pumped cesium vapor laser operating in ultraviolet and blue has been extended to 650 nJ/pulse for 387 nm, 1.3 μJ/pulse for 388 nm, 200 nJ/pulse for 455 nm and 500 nJ/pulse for 459 nm. Performance improves dramatically as the cesium vapor density is increased and no scaling limitations associated with energy pooling or ionization kinetics have been observed.

II. Background and Literature Review

2.1 Diode Pumped Alkali Laser (DPAL)

Despite an optically-pumped potassium vapor laser proposed by Schawlow and Townes in 1958, it was not until 2003 and 2005 when the first efficient lasing events in pulsed and continuous wave in Rubidium (Rb) and Cesium (Cs) vapors, respectively, were achieved [139]. Several comprehensive DPAL reviews [42, 71, 102, 136, 139] outline the benefits of the high quantum efficiency, gaseous gain medium, reduced thermal issues, diode pumping and scalability to high output powers.

The DPAL is a three-level laser employing an alkali vapor as the gain medium [71]. Optical excitation on the D_2 transition occurs between the ground $n^2S_{1/2}$ state and the excited $n^2P_{3/2}$ state where n, the radial quantum number, takes the values for n = 2, 3, 4, 5, 6 for the alkalis lithium (Li), sodium (Na), potassium (K), Rb and Cs, respectively. A population inversion between the $n^2P_{1/2}$ and ground states is achieved by rapid collisional relaxation and the DPAL laser transition from the $n^2P_{1/2}$ back to the ground $n^2S_{1/2}$ electronic level is designated by the historical label D_1. A buffer gas mixture at near atmospheric pressure is typically required to broaden the absorption line shape and induce the collisional relaxation. This three level system is outlined below in Figure 2.1.

DPAL performance is optimized when spin-orbit relaxation, with the help of a buffer gas (usually a rare gas such as helium, argon, krypton and/or small molecular hydrocarbon molecules), is much faster than the excitation transition rate [71]. Analytic quasi-two level analytic models has been developed and used to study DPAL kinetics and to investigate loss mechanisms [20, 46, 89, 103, 119, 133, 135]. The interactions that occur within the DPAL gain cell can be complex and lead to multiple deleterious processes as outlined in Oliker et al. [89].

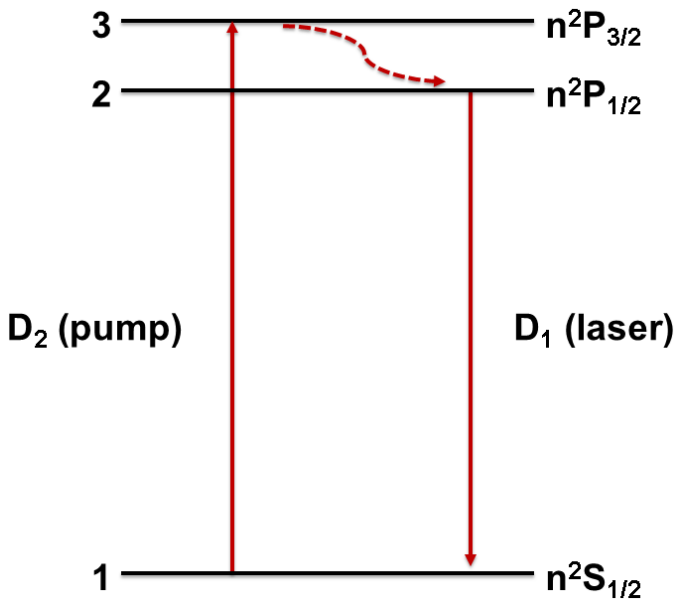

Figure 2.1: DPAL energy levels (ground $n^2S_{1/2}$ and excited $n^2P_{3/2}$ and $n^2P_{1/2}$ levels), pump (D_2) and laser (D_1) transitions.

A major emphasis of DPAL research to date has been scaling the alkali laser to higher laser output power [102, 139]. Significant results include 10 W output power for a continuous wave (cw) Cs D_1 transition ($6^2P_{1/2} \rightarrow 6^2S_{1/2}$) using 500 torr of ethane buffer gas [138], 17 W output power for a cw Rb D_1 transition ($5^2P_{1/2} \rightarrow 5^2S_{1/2}$) using 600 torr of ethane buffer gas [141], 28 W output power for a pulsed Rb D_1 transition using 2100 torr of He buffer gas [145], 16 W output power for a pulsed K D_1 transition ($4^2P_{1/2} \rightarrow 4^2S_{1/2}$) using 600 torr of He buffer gas [140], $\sim$1 kW output power for a cw Cs D_1 transition [15], and 1.5 kW pumped potassium (K) DPAL with a slope efficiency of 50% [102].

In addition to high power output, Zhdanov and Knize [139] outline and discuss several additional benefits of the DPAL laser. One focus is the spectral diversity of DPALs operating wavelengths. Several articles describe alkali laser lasing or amplified spontaneous emission for various spectral bands extending from visible [21, 119], near infrared [137], mid-wave infrared and long-wave [103]; however, very few experimental

results have been reported on DPAL ultraviolet (UV) transition [24, 28, 75, 91, 97]. Given the benefits of one laser, or a laser consisting of various alkali gases, having the capability to lase from spectral bands ranging from UV to long wave infrared may prove beneficial to military operations.

The need for high power lasers with diverse lasing transition outputs cannot be overstated. One immediate need is to use lasers to help counter emerging air-to-air and air-to-ground missile threats [56]. By 2020, with respect to laser countermeasure techniques, defeating next generation missile seekers may require a laser (or suite of lasers) with in-band lasing requirements for UV, visible, short-wave infrared (SWIR) and mid-wave infrared (MWIR) with average powers ranging from 10s to several 100s Watts to jam and/or damage seeker optics/electronics [23, 129]. Table 2.1 depicts percent atmospheric transmissions of possible DPAL alkali laser emissions taken from a previous study [103] and Rb and Cs blue and UV laser emissions for mid-latitude summer conditions for a nose-to-nose air engagement at 25 kft for various close-in conditions (3, 6 and 10 nautical miles). Table 2.1 is just a subset of the potential DPAL transitions; however, in general, the laser emissions span the atmospheric window and exhibit high transmission values except where laser lines fall in key absorption lines for oxygen (O_2), carbon dioxide (CO_2) and water vapor (H_2O).

2.2 Alkalis

To date, of the alkalis listed in Table 2.2, only potassium (K), rubidium (Rb) and cesium (Cs) have been used to create a three-level DPAL laser system. Lithium (Li) and sodium (Na) DPAL variants have not been achieved and are problematic, as they approach a two level system due to the close energy spacing of their respective $n(= 2,3)^2P_{3/2}$ and $n(= 2,3)^2P_{1/2}$ states. The challenge in pumping DPALs efficiently is maintaining the narrow alkali gain cell absorption band (on the order of 0.01 nm) while increasing power. In addition, recent diode pump laser advancements for K, Rb and Cs DPALs

Table 2.1: Atmospheric transmissions of select DPAL alkali laser emissions for potassium (K) rubidium (Rb) and cesium (Cs) for mid-latitude summer conditions for an air-to-air engagement at 25 kft.

			Atmospheric path transmission		
Alkali	Transition	Wavelength (μm)	3 NM	6 NM	10 NM
K	$4^2D_{5/2,3/2} \rightarrow 5^2P_{3/2}$	3.73	0.98	0.96	0.94
	$6^2S_{1/2} \rightarrow 5^2P_{1/2,3/2}$	3.63, 3.62	0.99, 0.98	0.99, 0.96	0.99, 0.93
	$5^2D_{3/2} \rightarrow 5^2P_{1/2,3/2}$	1.82, 1.83	0.53, 0.20	0.29, 0	0.12, 0
Rb	$5^2D_{3/2} \rightarrow 6^2P_{1/2,3/2}$	5.04, 5.24	0.98, 0.34	0.96, 0.11	0.93, 0.03
	$7^2S_{1/2} \rightarrow 6^2P_{1/2,3/2}$	3.85, 3.97	0.99, 0.99	0.98, 0.98	0.97, 0.96
	$6^2D_{3/2} \rightarrow 6^2P_{1/2,3/2}$	2.01, 2.04	0.92, 0.98	0.85, 0.97	0.77, 0.95
	$6^2P_{3/2,1/2} \rightarrow 5^2S_{1/2}$	0.420, 0.421	0.93, 0.93	0.86, 0.86	0.78, 0.78
	$7^2P_{3/2,1/2} \rightarrow 5^2S_{1/2}$	0.358, 0.359	0.87, 0.87	0.75, 0.76	0.62, 0.63
Cs	$6^2D_{3/2} \rightarrow 7^2P_{1/2,3/2}$	12.14, 15.57	0.99, 0	0.99, 0	0.99, 0
	$8^2S_{1/2} \rightarrow 7^2P_{1/2,3/2}$	3.92, 4.22	0.85, 0	0.73, 0	0.59, 0
	$7^2D_{3/2} \rightarrow 7^2P_{1/2,3/2}$	2.34, 2.44	0.75,0.99	0.56, 0.99	0.38, 0.98
	$9^2S_{1/2} \rightarrow 7^2P_{1/2,3/2}$	1.94, 2.01	0.13, 0.93	0, 0.86	0, 0.77
	$7^2P_{3/2,1/2} \rightarrow 6^2S_{1/2}$	0.455, 0.459	0.95, 0.95	0.90, 0.90	0.84, 0.84
	$8^2P_{3/2,1/2} \rightarrow 6^2S_{1/2}$	0.387, 0.388	0.90, 0.90	0.81, 0.82	0.71, 0.71

[60, 63, 64, 81], these same diode advancements can, in principle, be extended towards creating powerful laser sources for the Na and Li pump transition wavelengths. Besides the alkali atoms, Table 2.2 also contains the radial quantum number (n), pump and laser transitions, spin-orbit splitting energy, ΔE, between $n^2P_{3/2,1/2}$ electronic states and the quantum energy defect, $\Delta E/E_{\text{pump}}$, where $E_{\text{pump}} = hc/\lambda_{\text{pump}}$. The quantum defect is the fractional amount of waste heat deposited in the alkali gain medium per atomic excitation. For comparison, the alkali quantum energy defects are much lower than the standard solid state lasers Nd (0.27) and Yb (0.10) [71]. Only cesium was used during the present research, and information on this element is presented below. Tables 2.2, 2.3, 2.4, and 2.5 list many of the physical parameters for the cesium D_1 and D_2 transitions.

Table 2.2: Pump and laser transition wavelengths and spin-orbit splitting energies [71].

Alkali	n	D_2 λ_{pump} (nm)	D_1 λ_{laser} (nm)	ΔE (cm^{-1})	$\Delta E/E_{\text{pump}}$
Li	2	670.96	670.98	0.34	0.000023
Na	3	589.16	589.76	17.20	0.00101
K	4	766.70	770.11	57.70	0.0044
Rb	5	780.25	794.98	237.50	0.019
Cs	6	852.35	894.59	554.10	0.047

The number density of alkali in the system is based on the vapor pressure at the surface of the alkali pool. The relationship between temperature and pressure is given by the equations below for ^{133}Cs for temperatures below melting (solid phase, Equation (2.1)), and temperature above melting point (liquid phase, Equation (2.2)) [4]:

$$\log_{10}(P_v) = 2.881 + 4.711 - \frac{3999}{T} \tag{2.1}$$

$$\log_{10}(P_v) = 2.881 + 4.165 - \frac{3830}{T} \tag{2.2}$$

where the vapor pressure, P_v, is given in Torr and the temperature (T) given in Kelvin (K). Using the ideal gas law, the vapor pressure is converted into a number density. The ^{133}Cs number density curve is shown in Figure 2.2. As seen in Figure 2.2, the Cs number density increases rapidly for increasing temperature. In the experiments conducted in this study, the Cs gain cell temperatures ranged from 25°C to 200°C which translates to a Cs number density of 5.13×10^{10} cm^{-3} and 1.82×10^{15} cm^{-3}, respectively. This is a five orders of magnitude change in the Cs number density in this 175°C change.

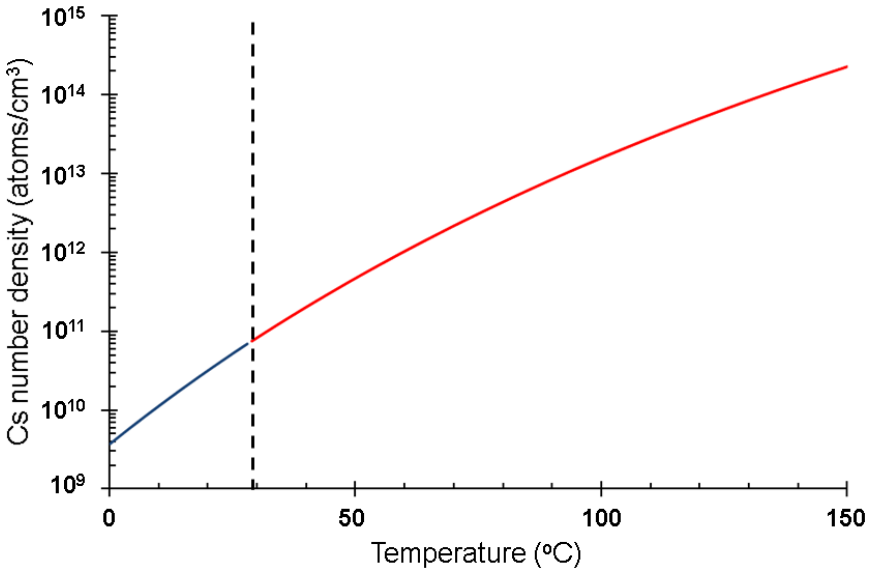

Figure 2.2: Combined Cs number density curves as a function of temperature [118]. The blue line represents the Rb density before melting point, shown as (- - -), with the red line representing the Cs density after the melting point.

Table 2.3: ^{133}Cs Physical Properties [118].

Atomic Number	Z	133	
Relative Natural Abundance	$\eta(^{133}Cs)$	100%	[74]
Nuclear Lifetime	τ_n	(stable)	[74]
Atomic Mass	m	132.905 451 931(27) amu	[17]
Density at 25°C	ρ_m	1.93 g/cm^3	[74]
Melting Point	T_M	28.5°C	[74]
Boiling Point	T_B	671°C	[74]
Nuclear Spin	I	7/2	

Table 2.4: ^{133}Cs D_2 Transition Optical Properties [118].

Frequency	ω_0	2π·351.725 718 50(11) THz	[8, 134]
Transition Energy	$\hbar\omega_0$	1.454 620 563(35) eV	
Wavelength (Vacuum)	λ_{vac}	852.347 275 82(27) nm	
Wavelength (Air)	λ_{air}	852.120 532(26) nm	
Wave Number (Vacuum)	$k_L/2\pi$	11 732.307 104 9(32) cm^{-1}	
Lifetime	τ	30.405(77) ns	[14, 45, 116, 127]
Natural Line Width (FWHM)	Γ	2π·5.234(13) MHz	

Table 2.5: ^{133}Cs D_1 Transition Optical Properties [118].

Frequency	ω_0	2π·335.116 048 807(41) THz	[6, 8]
Transition Energy	$\hbar\omega_0$	1.385 928 495(34) eV	
Wavelength (Vacuum)	λ_{vac}	894.592 959 86(10) nm	
Wavelength (Air)	λ_{air}	894.355 151(27) nm	
Wave Number (Vacuum)	$k_L/2\pi$	11 178.268 160 7(14) cm^{-1}	
Lifetime	τ	34.791(90) ns	[45, 116, 127]
Natural Line Width (FWHM)	Γ	2π·4.575(12) MHz	

2.3 DPAL Spin-orbit Rate Kinetics

The DPAL kinetics describe the rates of various reactions within the system. The two points of concern are the spin-orbit (SO) mixing rate, also known as relaxation, and the quenching rates. Since this study focuses on the alkali $n\,^2D$ states (for $n = 7, 8$), the SO mixing rate determines how fast the alkali transitions between the excited $^2D_{5/2}$ and $^2D_{3/2}$ states. The quenching rates correspond to the rate of transitions between $^2D_{5/2} \rightarrow {}^2S_{1/2}$ and $^2D_{3/2} \rightarrow {}^2S_{1/2}$ through non-radiative means which removes population that could otherwise contribute to the laser system. The transition for exciting the alkali $n\,^2D$ states by two-photon absorption with a buffer gas is illustrated in Figure 2.3. In a DPAL, the goal is to have the highest possible SO rate while minimizing the quenching rate. This study examines the SO mixing rates and cross sections for the Cs $7^2D_{5/2,3/2}$ and $8^2D_{5/2,3/2}$ states.

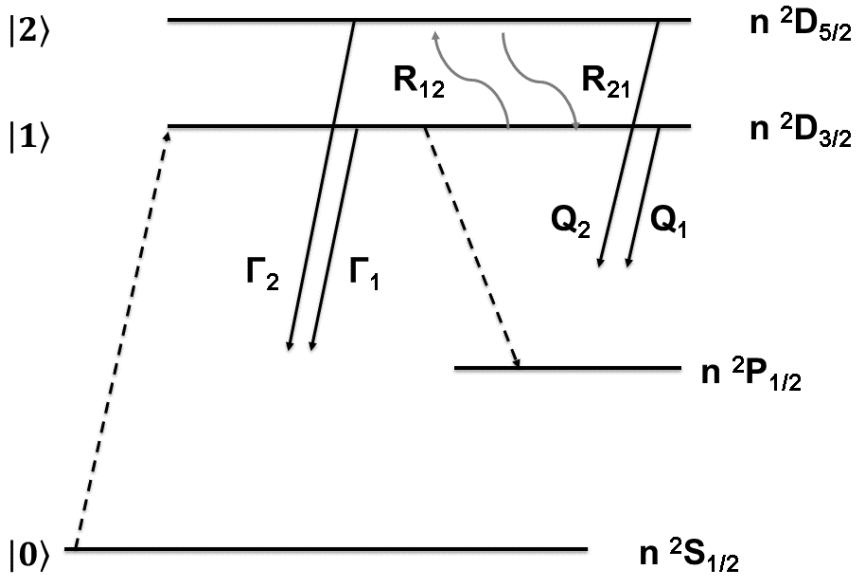

Figure 2.3: Alkali energy levels for n^2D fine structure collisional mixing where Γ_2 and Γ_1 are the radiative decay rates, Q_2 and Q_1 are the collisional quenching rates and R_{21} and R_{12} are the collisional mixing rates.

High precision spectroscopy of atomic alkali structures plays an important role in determining and verifying transition rates, atomic cross sections, collisional quenching rates, spin-orbit rates and validated models that attempt to predict these complex atomic interactions. Excitation from the cesium $6^2S_{1/2}$ to 7^2D states by two-photon transitions has been performed to determine hyperfine coupling constants for 7^2D states [59, 73] and indirectly researching cesium blue lasing as a result of transitions from the 7^2D to 7^2P states and eventually back to the $6^2S_{1/2}$ state [21, 119]. However, despite the work done on the 7^2D hyperfine structure, the fine-structure spin-orbit relaxation and collisional quenching of the $7^2D_{5/2,3/2}$ states have not been measured for any rare gas or hydrocarbon collision partners. Lifetimes for the $7^2D_{5/2,3/2}$ have been reported as 88.9 ns and 89.4 ns, respectively [124]; however, to the best of our knowledge, mixing rates and/or cross sectional areas with buffer gases have not been reported for the 7^2D states. It is the intent of part of this research to measure the spin-orbit and collisional quenching rates for the 7^2D states.

The fine structure mixing in cesium with rare gas collision partners has been studied previously for the $n = 6 - 8\,^2P_{3/2,\,1/2}$ and $n = 8 - 14\,^2D_{5/2,\,3/2}$ states [33, 41, 55, 67, 68, 77, 85, 98, 115]. The prior cw laser induced florescence (LIF) work by Jackowska [55] and Lukaszewski [77] for the $n = 8$ and $9\,^2D$ states exhibit cross-sections at 29% and 14% of the quantum defect values, respectively. In the present work we re-examine the $8\,^2D_{3/2,\,5/2}$ mixing rates induced by helium and argon using pulsed lifetime techniques. The combined advantages of pulsed and cw energy transfer studies are often useful in rate validation [125].

2.3.1 Pulsed Experiment.

The transitions considered for exciting the $7^2D_{3/2,5/2}$ and $8^2D_{3/2,5/2}$ levels of the cesium atom by two-photon absorption with a buffer gas are illustrated in Figure 2.3. The buffer gases used in this study were helium (He) and argon (Ar). The radiative decay rates from states $|2\rangle, |1\rangle$ are labeled as Γ_2 and Γ_1. The collisional mixing rates from state $|2\rangle \rightarrow |1\rangle$ and $|1\rangle \rightarrow |2\rangle$ are labeled as R_{21} and R_{12}, respectively. The mixing rates R_{12} and R_{21} adhere

to the principle of detailed balance

$$\frac{R_{12}}{R_{21}} = \frac{g_2}{g_1} e^{-\Delta E/k_b T} = \rho, \tag{2.3}$$

where $g_2 = 6$ and $g_1 = 4$ represent the degeneracies of the respective $7^2D_{5/2,3/2}$ and $8^2D_{5/2,3/2}$ atomic states, ΔE is the energy difference between these states (21 cm^{-1} for the 7^2D and 11 cm^{-1} for the 8^2D states), k_b is the Boltzmann constant and T is the temperature.

The spin-orbit mixing rate is related to the thermally averaged collision cross-section, σ_{21}, via the average relative speed of the collision pair, $\bar{v}$:

$$R_{21} = (n)(\sigma_{21})(\bar{v}) = (n)k_{21}, \tag{2.4}$$

where n is the rare gas density and k_{21} is the spin-orbit mixing rate coefficient. The average relative speed of the collision pair, $\bar{v}$, is given by $\bar{v} = 8k_bT/\pi\mu$ where T is the cell temperature and μ is the reduced mass of the alkali and buffer gas pair. Last, the collisional quenching rates associated with the depopulation of states $|2\rangle$ and $|1\rangle$ are labeled Q_2 and Q_1.

The time evolution of the population densities in states $|2\rangle$ and $|1\rangle$ after pulsed excitation is described by the first-order system of differential equations:

$$\frac{dn_2(t)}{dt} = -(\Gamma_2 + R_{21} + Q_2)n_2(t) + R_{12}n_1(t), \tag{2.5}$$

$$\frac{dn_1(t)}{dt} = -(\Gamma_1 + R_{12} + Q_1)n_1(t) + R_{21}n_2(t) \tag{2.6}$$

Defining $\alpha_2 = -(\Gamma_2 + R_{21} + Q_2)$ and $\alpha_1 = -(\Gamma_1 + R_{12} + Q_1)$, the general solution takes the form of a double exponential

$$n_1(t) = Ae^{\lambda_+ t} + Be^{\lambda_- t}, \tag{2.7}$$

where λ_+, λ_- are given by the eigenvalues [21, 108, 112],

$$\lambda_\pm = \frac{1}{2}\{-(\alpha_1 + \alpha_2) \pm \sqrt{(\alpha_1 - \alpha_2)^2 + 4R_{12}R_{21}}\} \tag{2.8}$$

and A and B are constants to be determined.

For initial conditions where the near instantaneous pump populates the $7^2D_{5/2}$ state, $n_1(t = 0) = 0$ and $n_2(t = 0) > 0$, the solution for the parent, n_2, and satellite, n_1 states become:

$$n_1(t) = A\left(\exp^{\lambda_+ t} - \exp^{\lambda_- t}\right) \tag{2.9}$$

$$n_2(t) = \frac{A\left((\alpha_1 + \lambda_+)\exp^{\lambda_+ t} - (\alpha_1 + \lambda_-)\exp^{\lambda_- t}\right)}{R_{21}} \tag{2.10}$$

For high rare gas densities where $R_{12} - R_{21} \gg \Gamma_1 - \Gamma_2$ and assuming $Q_1 = Q_2 = Q$, Equation (2.8) can be approximated in this limit as [21, 108, 112]

$$\lambda_+ = \frac{\Gamma_1 + \Gamma_2}{2} - \left(\frac{\rho - 1}{\rho + 1}\right)\frac{\Gamma_1 - \Gamma_2}{2} + \sigma_Q(n)(\overline{v}), \tag{2.11}$$

$$\lambda_- = \frac{\Gamma_1 + \Gamma_2}{2} + \left(\frac{\rho - 1}{\rho + 1}\right)\frac{\Gamma_1 - \Gamma_2}{2} + [\sigma_Q + \sigma_{21}(\rho + 1)](n)(\overline{v}), \tag{2.12}$$

where ρ is given by Equation (2.3), σ_{21} by Equation (2.4), $\sigma_Q = Q/[(n)(\overline{v})]$ and we define $k_Q = \sigma_Q(n)$ as the quenching rate coefficient.

2.3.2 Adiabaticity Theory.

In 1966, Krause used adiabaticity arguments to describe interaction between an alkali-metal atom and a rare gas collision partners [66]. Krause determined that Rb and Cs alkali interactions with rare gases were considered adiabatic due to low relative velocity and large spin-orbit splitting and further validated using the Massey adiabaticity parameter as defined in [37]. This is not the case for rare gas collisions with lithium (Li), sodium (Na), and potassium (K) where Krause determined these interactions to be non-adiabatic but did not develop a theory to explain the relationship between adiabaticity and magnitude of the spin-orbit cross section. In 1968, Gallagher extended Krauses work by developing an empirical

relationship between measured spin-orbit cross sections for the first excited P states for Rb and Cs and reduced mass-adjusted temperature [41]. Besides the empirical relationship developed in Gallagher's work, adiabaticity theory was not advanced beyond Krause's 1966 study. In 1980, Elward-Berry applied the Massey adiabaticity parameter as part of analysis of Li first excited P states and rare gas spin-orbit cross sections [37]. Combined with Krause and Gallagher's work, the Massey adiabaticity parameter provided a correlation methodology to organize spin-orbit cross sections for the various alkali-metalrare gas pairs.

In 2017, Eshel et. al. [38] showed collision cross sections for alkali and rare gas spin-orbit mixing between the $n^2P_{3/2} \rightarrow n^2P_{1/2}$ energy levels trend strongly with the Massey parameter [37]. Eshel further develops a theoretical model that captures the temperature dependence of the spin-orbit mixing rates for all measured alkali P state collisions with rare gas partners and captures the adiabaticity trends observed by Gallagher [41], Krause [66] and Elward-Berry [37].

As detailed in [38, 39], the extent to which the alkali doublet transfer collision with the rare gas species is sudden or adiabatic depends on the interatomic velocity as well as the spin-orbit splitting [41]. For the alkali-rare gas collision the adiabaticity is defined as [37]

$$\zeta = \frac{\tau_c}{\tau_\nu} = \frac{\Delta L}{\bar{v}} \tag{2.13}$$

where τ_c is the duration of the collision (atom-atom interaction time), τ_ν is the period of oscillation defined by the spin-orbit splitting $\left(\tau_\nu = 1/\nu = h/\Delta_{fs}\right)$, Δ_{fs} is the spin-orbit splitting, L is the interaction length and $\bar{v}$ is the mean relative speed. Using the results of [39], we set the interaction length, L, to 10Å despite not knowing how the potential energy surfaces trend.

The energy-transfer probability per collision can also be defined by dividing the experiment cross section, σ_{exp}, by the quantum-defect cross section, σ_{QD}. Since the alkalis are well represented by hydrogenic approximations [124], the expectation value of the

electron position, $\langle r \rangle$, is given by

$$\langle r \rangle = a_\mu (n^*)^2 \left(1 + \frac{1}{2}\left(1 - \frac{l(l+1)}{(n^*)^2}\right)\right) \tag{2.14}$$

where a_μ is the effective Bohr radius of the alkali, l is the angular momentum quantum number and n^* is the effective quantum number given by

$$n^* = \sqrt{\frac{E_{Ryd}}{T - E}} \tag{2.15}$$

In Equation (4.7) E_{Ryd} is the Rydberg energy (109737.32 cm^{-1}), T is the ionization energy and E is the energy level corresponding to the effective quantum number. For example, the effective quantum number for $8^2D_{5/2,3/2}$ are 5.53 and 5.52, respectively.

The fine structure transition probability, whether it be $^2P_{3/2} \rightarrow^2 P_{1/2}$ or $^2D_{5/2} \rightarrow^2 D_{3/2}$, can be defined by the ratio of the experimentally measured cross section, σ_{exp} and the quantum defect cross section, σ_{QD},

$$P = \frac{\sigma_{exp}}{\sigma_{QD}} \tag{2.16}$$

with

$$\sigma_{QD} = \pi \left(\langle r \rangle + r_{Rg}\right)^2 \tag{2.17}$$

where $\langle r \rangle$ is the expectation value of the Cs atom's electron position and r_{Rg} is the effective radius of the rare gas atom [39]. Using this probability instead of the experimental cross section improves the correlation with adiabaticity [38].

Figure 2.4 shows the natural log probabilities for collisions pairs organized by adiabaticity. Cross sections were derived from the fine structure mixing rates measured for Li ($2p$) [37], Na ($3p$) [57, 90, 99], K ($4p$) [27, 57, 66, 83], K ($5p$) [11], Rb ($5p$) [10, 66, 99, 112], Rb ($6p$) [85, 114], Rb ($7p$) [85], Cs ($6p$) [66, 68], Cs ($7p$) [85], and Cs ($8p$) [98] in collisions with rare gases at a fixed temperature. Figure 2.4 shows the He and Ne data form lower bound curve, regardless of alkali-metal collision partner. This study extends the analysis in [38] to include higher order Cs 7^2D and 8^2D and higher-lying Cs Rydberg states [55, 77].

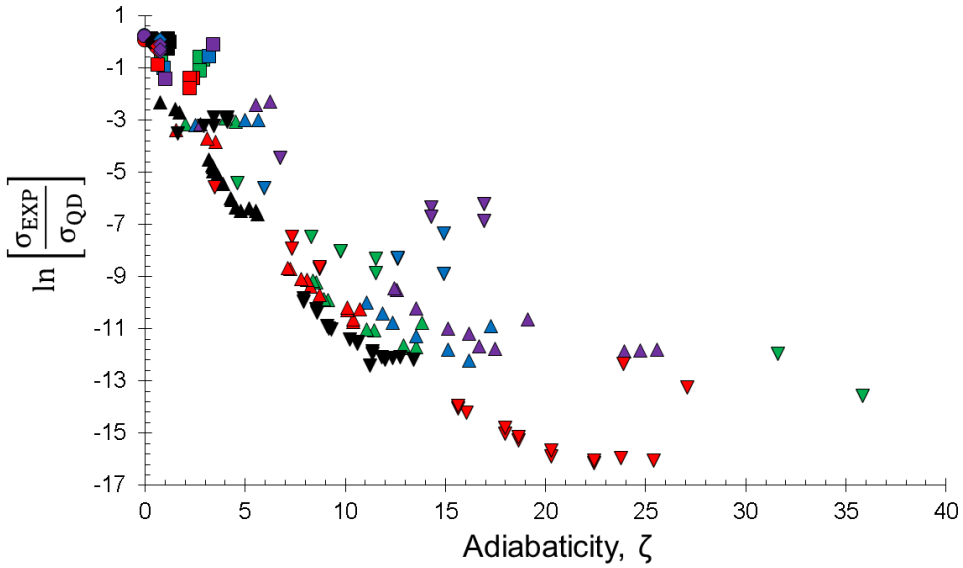

Figure 2.4: Alkali probabilities versus adiabaticity with fixed interaction length, $L = 10$Å. The alkalis are depicted by ∘, Li; ⋄, Na; □, K; △, Rb; ▽, Cs with colors corresponding to He (black), Ne (red), Ar (green), Kr (blue), and Xe (magenta).

2.4 Cs UV and blue laser emission study

Alternative wavelengths from these optically-pumped alkali lasers are desirable for several civilian and military applications. In 1958 Schawlow and Townes [109] proposed an optically-pumped potassium laser pumped in the blue ($4^2S_{1/2} \rightarrow 5^2P_{3/2}$) with lasing at 2.71 μm ($5^2P_{3/2} \rightarrow 5^2S_{1/2}$) or 3.14 μm ($5^2P_{3/2} \rightarrow 3^2D_{3/2}$). In 1962, Rabinowitz, et al. [104] proposed an similar lasing scheme for Cs for pump a Cs vapor in the UV ($6^2S_{1/2} \rightarrow 8^2P_{1/2}$) with lasing at 7.18 μm ($8^2P_{1/2} \rightarrow 8^2S_{1/2}$) or 3.20 μm ($8^2P_{1/2} \rightarrow 6^2D_{3/2}$). These cascading lasing systems were followed in 1972 by a tunable potassium infrared laser operating at 25.4 μm using four-wave mixing [117]. Recently efforts have demonstrated for K, Rb and Cs alkali lasers operating in the blue via both single and two-photon pump schemes [2, 3, 19, 82, 103, 111, 119].

Recent DPAL trends is to extend alkali alternative wavelengths to the blue-violet or ultraviolet beam lasing [29, 30, 40, 132]. Recent measurements in [40] reported ultraviolet $\left(8^2P_{3/2} \rightarrow 6^2S_{1/2}\right)$ and blue $\left(7^2P_{3/2} \rightarrow 6^2S_{1/2}\right)$ emissions after using a two-photon pumping the $6^2S_{1/2} \rightarrow 7^2D_{5/2}$ transition. Maximum powers achieved in this experiment were 700 nJ and 150 nJ for the ultraviolet and blue emissions, respectively for pump pulse power of 0.8 mJ [40]. Additional modulation studies conducted in [40] led to 4-wave mixing as the method for producing these ultraviolet and blue emissions. Current alkali UV analysis does not adequately address competing cascading and/or 4-wave mixing methods as leading to the blue-violet lasing. A full analysis of the kinetic mechanism is required to explore the contributions of cascade and 4-wave mixing to blue-violet lasing. Ultraviolet lasers have a variety of uses including material cutting and drilling, micro-lithography, grating fabrication, and eye surgery. Military uses include light detection and ranging for helicopter survivability, battlefield awareness, and data storage [122].

Lasers that can generate light directly in the near-ultraviolet (300 nm to 400 nm) directly include gallium nitride laser diodes, solid-state bulk lasers based on cerium-doped crystals, neodymium-doped fluoride fibers, xenon-fluoride excimer lasers, argon ion lasers, nitrogen lasers and free electron lasers [50]. Indirect generation of UV light can be achieved by nonlinear frequency conversion such as 355 nm based on frequency tripling the output of a 1064 nm neodymium-doped yttrium aluminum garnet (Nd:YAG) or neodymium-doped yttrium vanadate Nd:YVO4 laser [51].

Recently Gai et al. [40] used a Nd:YAG laser to pump an ND6000 dye laser to excite the Cs transition $6^2S_{1/2} \rightarrow 7^2D_{5/2}$ and characterized the resulting $7^2P_{3/2} \rightarrow 6^2S_{1/2}$ blue (455.6 nm) and $8^2P_{3/2} \rightarrow 6^2S_{1/2}$ UV (387.7 nm) laser emissions. Maximum powers achieved in this experiment were 700 nJ and 150 nJ for the UV and blue emissions, respectively, for pump pulse power of 0.8 mJ [40]. Additional modulation studies conducted in [40] led to four-wave mixing as the method for producing these ultraviolet

and blue emissions. This study extends the work in [40] and characterizes the blue and UV laser emissions resulting from pump transitions $6^2S_{1/2} \rightarrow 7^2D_{5/2,3/2}$.

III. Spin-orbit Relaxation of Cesium 7^2D in Mixtures of Helium and Argon

3.1 Introduction

Despite an optically pumped potassium vapor laser being proposed by Schawlow and Townes in 1958 [109], it was not until 2003 when the first efficient, diode-pumped lasing in rubidium (Rb) and cesium (Cs) vapors were achieved [70, 72]. The Diode Pumped Alkali Laser (DPAL), a three-level laser system, is pumped by diode bars or stacks through the alkali's D_2 transition to its $^2P_{3/2}$ state, then collisionally relaxed to the $^2P_{1/2}$ state where it lases in the near-infrared (NIR) along the D_1 transition. Lasing is achieved at 770 *nm* (K), 795 *nm* (Rb) and 894 *nm* (Cs). DPAL performance is optimized when spin-orbit relaxation, with the help of a buffer gas (usually a rare gas or small hydrocarbon), is much faster than the optical excitation rate [46, 48, 71]. Several comprehensive DPAL reviews [42, 71, 139] outline the benefits of this laser's high quantum efficiency, gaseous gain medium, reduced thermal issues, diode pumping and scalability to high output powers.

Several optically pumped alkali lasers operating at alternative wavelengths have also been demonstrated and require excitation above the first $^2P_{3/2}$ excited state [5, 19, 21, 22, 28, 52, 93, 103, 113, 119]. Optically pumped alkali lasers at far/mid infrared, near infrared, visible and ultraviolet wavelengths may be useful as beacons or illuminators for laser weapons, or for infrared countermeasures [92]. Like the traditional DPAL, these higher energy states require knowing the transition rates, optical cross sections, collisional quenching and spin-orbit rates to understand the competing and cascading laser transitions. One such excitation scheme, depicted in Figure 3.1, involves two-photon direct excitation of the Cs ground state to Cs $7^2D_{5/2,3/2}$ followed by primary infrared and visible transitions to the Cs 8^2P, Cs 7^2P and Cs 6^2P and secondary ultraviolet, blue and NIR transitions to the Cs $6^2S_{1/2}$ ground state. Indeed, blue lasers have been demonstrated by optically pumping in the near infrared using this scheme [103, 119]. However, the fine-structure spin-orbit and

collisional quenching rates of the Cs $7^2D_{5/2,3/2}$ states have not been reported. Excitation from the Cs $6^2D_{1/2} \rightarrow 7^2D_{5/2,3/2}$ states by two-photon transitions has been performed to determine hyperfine coupling constants for Cs 7^2D states [59, 73].

A thorough investigation of fine-structure mixing rates database for 8^2P, 7^2P and 6^2P states in alkali vapor collisions with rare gases reveal that fine-structure mixing rates increase with deceased energy splitting [39] and is consistent with previous adiabaticity studies [41]. Although [39] does not include high-lying excited alkali state such as Cs 7^2D; it is predicted that Cs 7^2D will exhibit more impulsive collisions with rare gases leading to faster spin-orbit rates. In this work, time resolved laser-induced fluorescence techniques are used to measure fine-structure mixing rates for the Cs $7^2D_{5/2,3/2}$ states with He and Ar rare gas collisions partners.

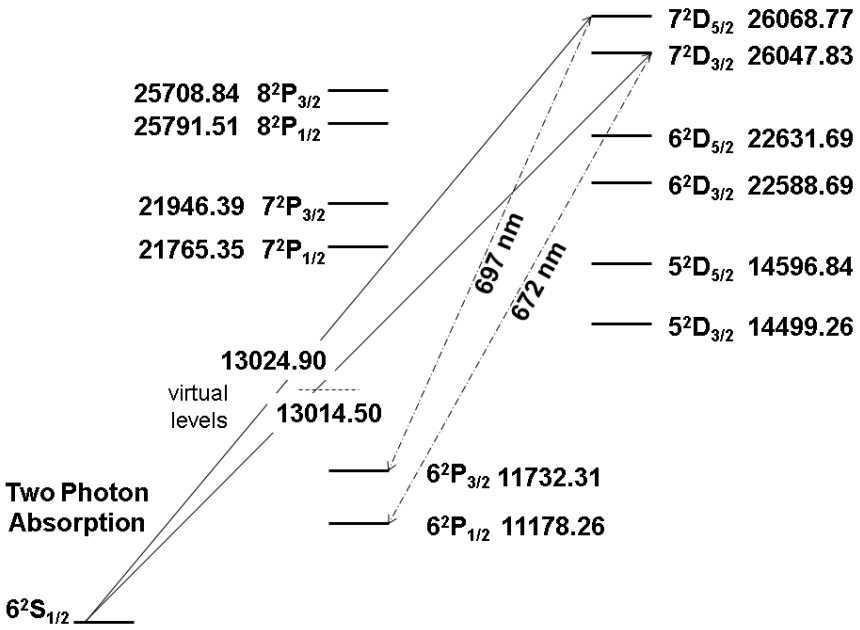

Figure 3.1: Cs energy level diagram.

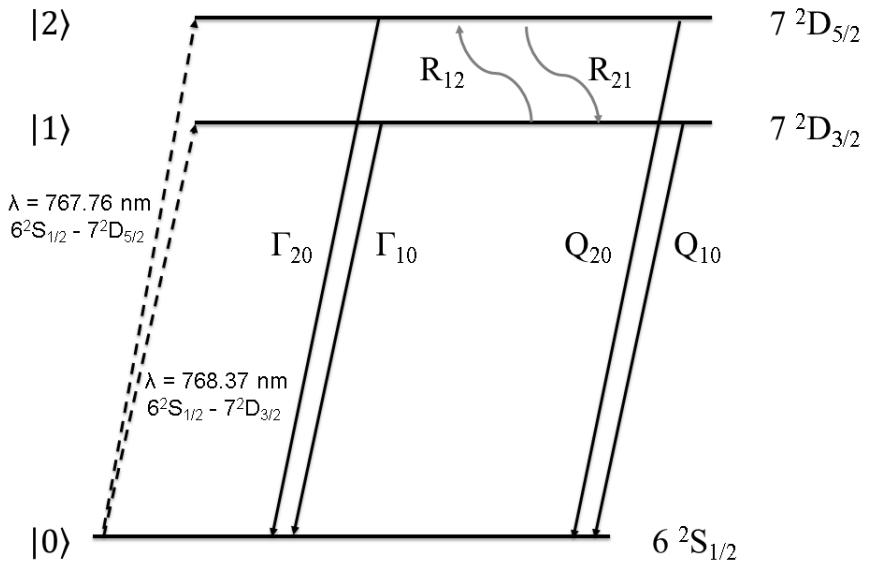

Figure 3.2: Cesium energy levels for the 7^2D fine structure collisional mixing.

3.2 Kinetic Analysis

The transitions considered for exciting the $7^2D_{3/2,5/2}$ levels of the cesium atom by two-photon absorption with a buffer gas are illustrated in Figure 3.2. The radiative decay rates from states $|2\rangle, |1\rangle$ to the ground state $|0\rangle$ is labeled as Γ_{20} and Γ_{10}. The collisional mixing rates from state $|2\rangle \rightarrow |1\rangle$ and $|1\rangle \rightarrow |2\rangle$ are labeled as R_{21} and R_{12}, respectively. The mixing rates R_{12} and R_{21} adhere to the principle of detailed balance

$$\frac{R_{12}}{R_{21}} = \frac{g_2}{g_1} e^{-\Delta E/k_b T} = \rho, \tag{3.1}$$

where $g_2 = 6$ and $g_1 = 4$ represent the degeneracies of the respective $7^2D_{5/2,3/2}$ atomic states, ΔE is the energy difference between these states (21 cm^{-1} for the 7^2D states), k_b is the Boltzmann constant and T is the temperature. For these same states and a temperature of 50°C, $\rho = 1.65$.

The spin-orbit mixing rate is related to the thermally averaged collision cross-section, σ_{21}, via the average relative speed of the collision pair, $\bar{v}$:

$$R_{21} = (n)(\sigma_{21})(\bar{v}) = (n)k_{21}, \tag{3.2}$$

where n is the rare gas density and k_{21} is the spin-orbit mixing rate coefficient. For Cs at 50°C with collision partners He and Ar, the mean relative velocities are 1.3×10^5 cm/sec for [Cs,He] and 4.7×10^4 cm/sec for [Cs,Ar]. Last, the collisional quenching rates associated with the depopulation of states $|2\rangle$ and $|1\rangle$ to the ground state $|0\rangle$ are labeled Q_{20} and Q_{10}.

The time evolution of the population densities in states $|2\rangle$ and $|1\rangle$ after pulsed excitation is described by the first-order system of differential equations:

$$\frac{dn_2(t)}{dt} = -(\Gamma_{20} + R_{21} + Q_{20})n_2(t) + R_{12}n_1(t), \tag{3.3}$$

$$\frac{dn_1(t)}{dt} = -(\Gamma_{10} + R_{12} + Q_{10})n_1(t) + R_{21}n_2(t) \tag{3.4}$$

Defining $\alpha_2 = -(\Gamma_{20} + R_{21} + Q_{20})$ and $\alpha_1 = -(\Gamma_{10} + R_{12} + Q_{10})$, the general solution takes the form of a double exponential

$$n_1(t) = Ae^{\lambda_+ t} + Be^{\lambda_- t}, \tag{3.5}$$

where λ_+, λ_- are given by the eigenvalues [21, 108, 112],

$$\lambda_\pm = \frac{1}{2}\{-(\alpha_1 + \alpha_2) \pm \sqrt{(\alpha_1 - \alpha_2)^2 + 4R_{12}R_{21}}\} \tag{3.6}$$

For initial conditions where the near instantaneous pump populates the $7^2D_{5/2}$ state, $n_1(t = 0) = 0$ and $n_2(t = 0) > 0$, the solution for the parent, n_2, and satellite, n_1 states become:

$$n_1(t) = A\left(e^{\lambda_+ t} - e^{\lambda_- t}\right) \tag{3.7}$$

$$n_2(t) = \frac{A\left((\alpha_1 + \lambda_+)\, e^{\lambda_+ t} - (\alpha_1 + \lambda_-)\, e^{\lambda_- t}\right)}{R_{21}} \tag{3.8}$$

For high rare gas densities where $R_{12} - R_{21} \gg \Gamma_{10} - \Gamma_{20}$ and assuming $Q_{10} = Q_{20} = Q$, Equation (3.6) can be approximated in this limit as [21, 108, 112]

$$\begin{aligned} \lambda_+ &= \frac{\Gamma_{10} + \Gamma_{20}}{2} - \left(\frac{\rho - 1}{\rho + 1}\right)\frac{\Gamma_{10} - \Gamma_{20}}{2} \\ &\quad + \sigma_Q(n)(\overline{v}), \end{aligned} \tag{3.9}$$

$$\begin{aligned} \lambda_- &= \frac{\Gamma_{10} + \Gamma_{20}}{2} + \left(\frac{\rho - 1}{\rho + 1}\right)\frac{\Gamma_{10} - \Gamma_{20}}{2} \\ &\quad + [\sigma_Q + \sigma_{21}(\rho + 1)](n)(\overline{v}), \end{aligned} \tag{3.10}$$

where ρ is given by Equation (3.2), σ_{21} by Equation (3.2), $\sigma_Q = Q/[(n)(\overline{v})]$ and we define $k_Q = \sigma_Q(n)$ as the quenching rate coefficient.

The fine structure transition probability can be defined by the ratio of the experimentally measured cross section, σ_{21} and the quantum defect cross section, σ_{QD},

$$P = \frac{\sigma_{21}}{\sigma_{QD}} \tag{3.11}$$

with

$$\sigma_{QD} = \pi\left(\langle r\rangle + r_{Rg}\right)^2 \tag{3.12}$$

where $\langle r\rangle$ is the expectation value of the Cs atom's electron position and r_{Rg} is the effective radius of the rare gas atom [39]. Since the alkalis are well represented by hydrogenic approximations [124], the expectation value of the electron position is given by

$$\langle r\rangle = a_\mu\,(n^*)^2\left(1 + \frac{1}{2}\left(1 - \frac{l(l+1)}{(n^*)^2}\right)\right) \tag{3.13}$$

where a_μ is the effective Bohr radius of the alkali, l is the angular momentum quantum number and n^* is the effective quantum number given by

$$n^* = \sqrt{\frac{E_{Ryd}}{T - E}} \tag{3.14}$$

In Equation (3.14) E_{Ryd} is the Rydberg energy (109737.32 cm^{-1}), T is the ionization energy and E is the energy level corresponding to the effective quantum number. The effective quantum numbers for $7^2D_{5/2,3/2}$ are 4.53 and 4.52, respectively.

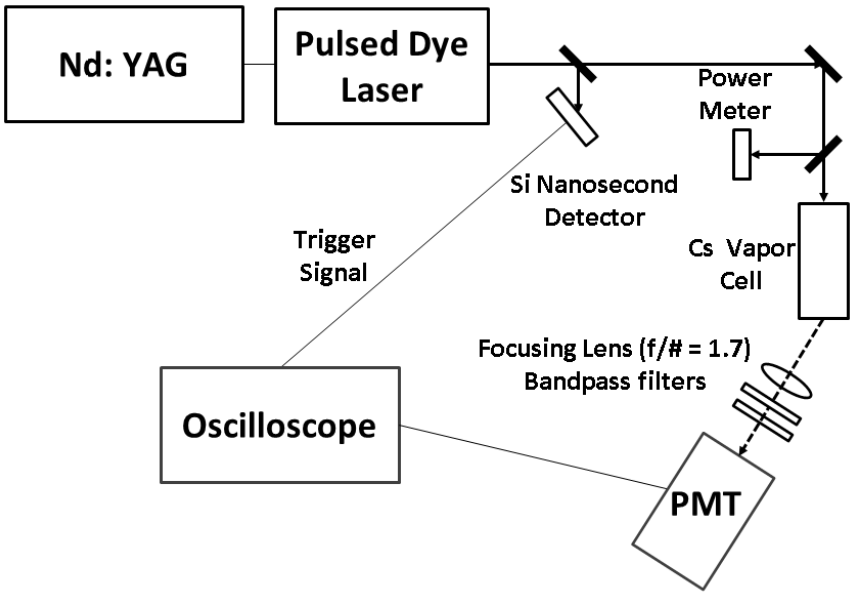

Figure 3.3: Temporally-resolved laser induced fluorescence apparatus.

The extent to which the alkali doublet transfer collision with the rare gas species is sudden or adiabatic depends on the interatomic velocity as well as the spin-orbit splitting [41]. For the alkali-rare gas collision the adiabaticity is defined as [37]

$$\zeta = \frac{\tau_c}{\tau_v} = \frac{\Delta L}{\bar{v}} \tag{3.15}$$

where τ_c is the duration of the collision, τ_v is the period of oscillation, Δ is the spin-orbit splitting, L is the interaction length and $\bar{v}$ is the mean relative speed. We choose to set the interaction length L at 10Å. When the duration of the collision is short, the time dependent perturbation is not averaged out due to oscillations in the state dynamics and a higher probability for energy transfer is achieved.

3.3 Experiment

The apparatus for the two-photon kinetic study for the $7^2D_{5/2,3/2} \rightarrow 6^2P_{3/2,1/2}$ is shown in Figure 3.3. A frequency-doubled Quanta-Ray Pro Series pulsed Nd:YAG laser ($10\ Hz$, $0 - 1\ J/pulse$, $532\ nm$) is used to pump a Sirah model PRSC-D-1800 dye laser with

LDS-765 dye tuned to populate the Cs $7^2D_{3/2}$ or $7^2D_{5/2}$ levels. The dye laser provides $6-10$ ns pulses in a 1 mm radius spot as the energy is tuned from 0 to 30 $mJ/pulse$ by varying the Nd:YAG flash-lamp energy. The Cs DPAL cell path is a 12 cm long and 2.54 cm diameter heatpipe [61]. The rare gas species, He or Ar, was monitored by two MKS Instruments 690A Baratron capacitance manometers with ranges of 1000 $Torr$ and 10 $Torr$. An aluminum heater block encloses the cell with a Watlow temperature controller connected to eight cartridge heaters and a thermocouple on a negative-feedback loop to control the cell temperature. Experiments were conducted at Cs DPAL cell temperatures of 25°C, 35°C, 40°C and 50°C to vary Cs alkali concentration and minimize the effect of radiation trapping on the spin-orbit mixing rate.

The target states, Cs $7^2D_{3/2}$ and Cs $7^2D_{5/2}$, are produced by two-photon absorption of the ground state, Cs $6^2S_{1/2}$, at wavelengths near 767.8 nm and 767.2 nm, respectively. The population of each excited state is measured by detecting the fluorescence measured by the C31034A photomultiplier tube using narrow bandpass filters and a BK 7 bi-convex lens with a diameter of 50.8 mm and focal length of 88.3 mm to observe two different transition states, Cs ($7^2D_{3/2} \rightarrow 6^2P_{1/2}$) at 672.3 nm and Cs ($7^2D_{5/2} \rightarrow 6^2P_{3/2}$) at 697.3 nm. A Thorlabs FES0750 shortpass filter with a cutoff wavelength of 750 nm was used to minimize scattered pump light yet allow over 88% transmission for both 672.3 nm and 697.3 nm fluorescence emissions. For the 672.3 nm emission, a second Andover Corp 670.8 nm filter with center wavelength and 10 nm bandwidth filter was used in conjunction with the shortpass filter. The 670.8 nm filter has a 66% transmission at 672.3 nm. For 697.3 nm, an Andover Corp 697.3 nm center wavelength filter with a 1 nm bandwidth was used with the shortpass filter. The tighter bandwidth requirement for 697.3 nm is needed to reduce fluorescence emissions from the Cs ($7^2D_{3/2} \rightarrow 6^2P_{3/2}$) transition at 698.3 nm. The peak transmission for this filter at 697.3 nm is 47%. For each pressure the scattered pump laser intensity was measured and subtracted from the observed decay profiles by tuning off

resonance, thereby minimizing the scattered light contribution to 7^2D states on-resonance fluorescence signal.

The observed intensities for the 672.3 *nm* and 697.3 *nm* emissions, I_1 and I_2, are proportional to the concentration of the corresponding emitting states

$$I_1 \propto [Cs_{7^2D_{3/2}\rightarrow 6^2P_{1/2}}]d_1 \propto n_1 d_1, \tag{3.16}$$

$$I_2 \propto [Cs_{7^2D_{5/2}\rightarrow 6^2P_{3/2}}]d_2 \propto n_2 d_2, \tag{3.17}$$

where d_1, d_2 depend on detection system efficiencies, transition probabilities and radiometric factors. The fluorescence of the Cs signal consisted of 1000 laser shots summed averaged using a 3 *GHz* LeCroy WavePro 7300 oscilloscope.

3.4 Results

To validate that Cs alkali atoms were pumped by two-photon absorption, excitation spectrum using the time integrated 697 *nm* and 672 *nm* fluorescence intensity as the signal were performed. The spectrum for the cesium cell at 35°C for these two emissions are shown in Figure 3.4. When monitoring the emission from $7^2D_{5/2}$ at 697 *nm* a signal is observed only when directly pumping the same state, confirming that the 1 *nm* bandpass filter is sufficient to isolate emission from $7^2D_{5/2}$. When pumping $7^2D_{3/2}$ a weak signal can be observed from the $7^2D_{5/2}$ state, suggesting minor Cs induced mixing. Very slow scan across a single feature reveals the ground $6^2S_{1/2}$ fine structure splitting with incomplete resolution, consistent with a laser linewidth of about 0.06 cm^{-1}.

All the intensity decay measurements for the He and Ar collision partners were performed at temperatures $\leqslant$ 50°C. As shown in Figure 3.5, temperatures above 75°C result in longer decay rates caused by radiation being absorbed and remitted before escaping the heat-pipe.

The time resolved fluorescence from the collisionally populated $7^2D_{3/2}$ state after two-photon excitation of the $7^2D_{5/2}$ state for various helium pressures is provided in Figure 3.6.

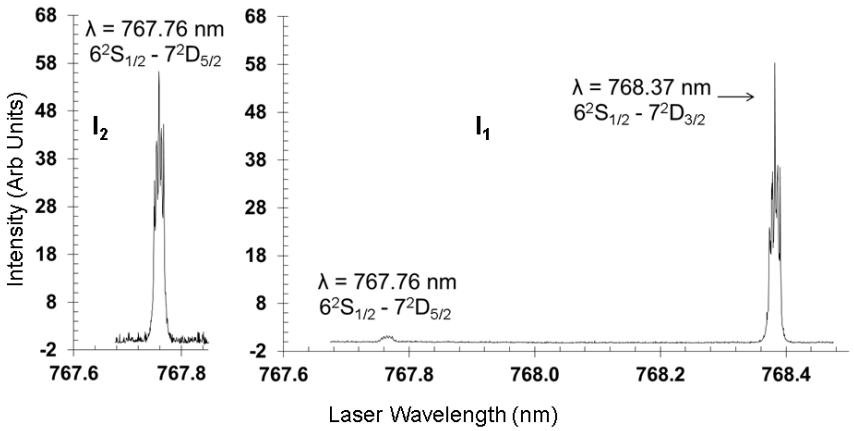

Figure 3.4: Laser excitation spectra using the time integrated fluorescence intensity at 697 and 672 *nm*.

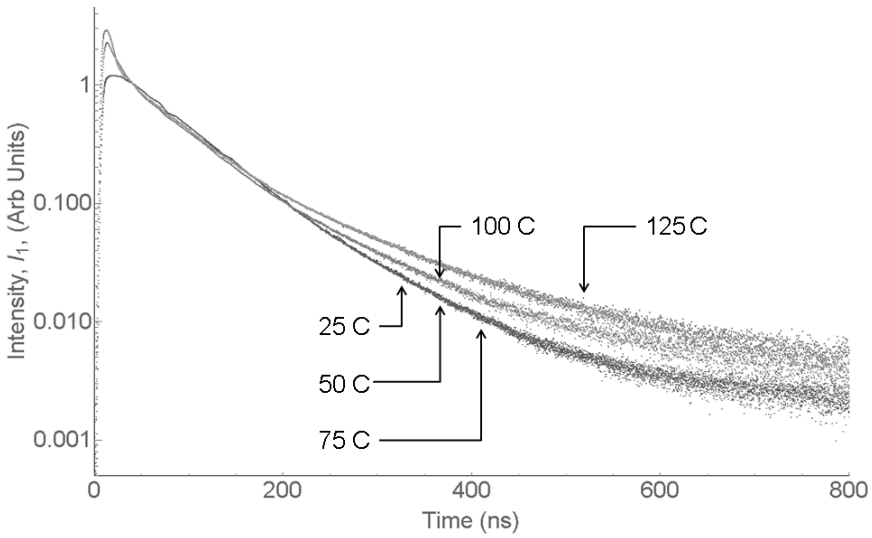

Figure 3.5: Emission intensity, I_1, from $7^2D_{3/2}$ when pumping the same $7^2D_{3/2}$ state at several Cs cell temperatures and no added buffer gas. The intensities grow dramatically with temperature, but have to be normalized to the same value just after the laser pulse to illustrate the radiation trapping at $T > 75°C$.

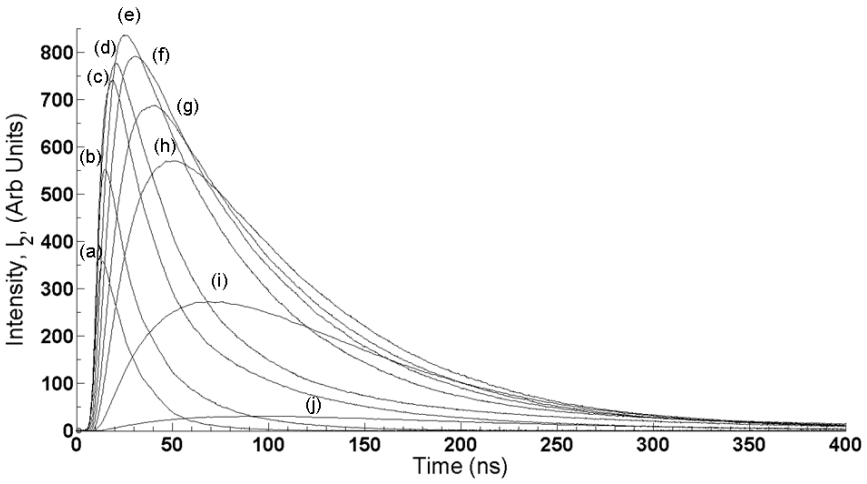

Figure 3.6: Fluorescence decay curves of the Cs $7^2D_{3/2} \rightarrow 6^2P_{1/2}$ emission after excitation of $7^2D_{5/2}$ at 50°C for helium buffer gas pressures in Torr (a) 100, (b) 50, (c) 15, (d) 7, (e) 2, (f) 1, (g) 0.5, (h) 0.25,(i) 0.1, (j) 0.

The rate for fine structure mixing is very rapid. Even at 0.1 $Torr$ of helium, as significant population is observed with a peak occurring 60 ns after excitation. At 7 $Torr$ the rise time is shorter than the pump pulse duration and only the longer quenching decay can be observed. At the higher pressures the peak signal decreases due to quenching during the excitation pulse.

For each pressure, the decay curves, such as those in Figure 3.7, were fit to the double exponential function of Equation (3.7) generating the two eigenvalues. The pressure dependence of the fit eigenvalues are displayed as Stern-Volmer plots for He in Figure 3.8 and similar curves were analyzed for Ar.

For He, the experimentally calculated spin-orbit rate is derived from the slope of eigenvalue λ_+ as shown in Figure 3.8. The slope is $3.1 \pm 0.1 \times 10^{-9}\ cm^3/sec$ yielding a fine structure relaxation rate of $k_{21} = 1.26 \pm 0.05 \times 10^{-9}\ cm^3/sec$. From the slope of λ_- we obtain the quenching rate $k_Q = 6.84 \pm 0.09 \times 10^{-11}\ cm^3/sec$. For an average temperature of 40°C, the respective spin-orbit and quenching cross sections are $\sigma_{21} = 9.6 \pm 0.4 \times 10^{-15}\ cm^2$

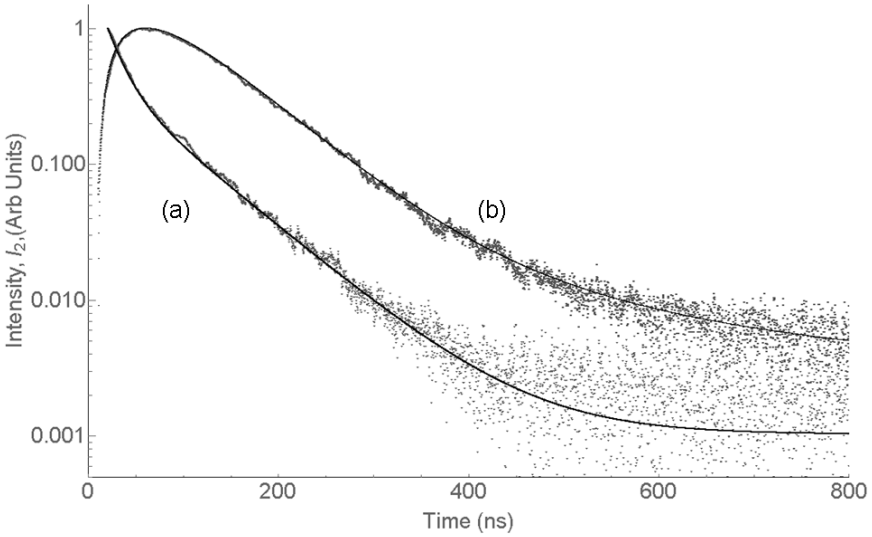

Figure 3.7: Emission on $7^2D_{5/2} \rightarrow 6^2P_{3/2}$ at 697 *nm* after excitation on $7^2D_{3/2}$ for Ar pressures of (a) 50 *Torr* and (b) 0.7 *Torr*. A fit to Equation (3.7) is also provided.

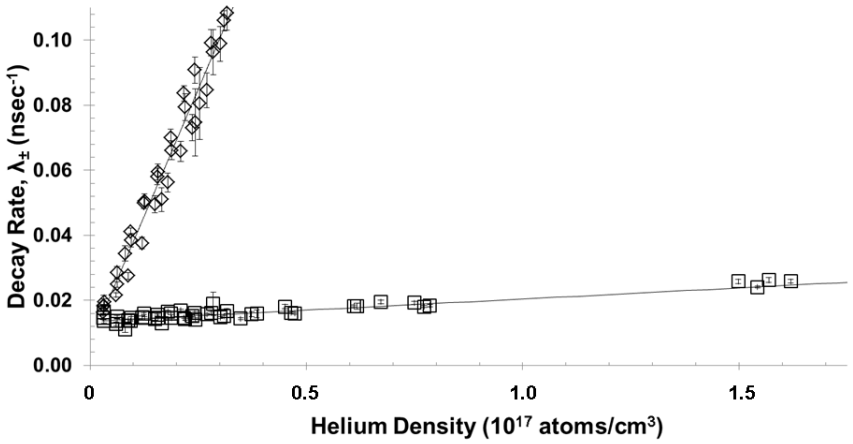

Figure 3.8: Stern-Volmer plot of experimentally derived rates based on Equation (3.7) for Helium at temperatures $\leq$ 50°C. The solid line is a least-squares linear fit to the experimentally derived rates.

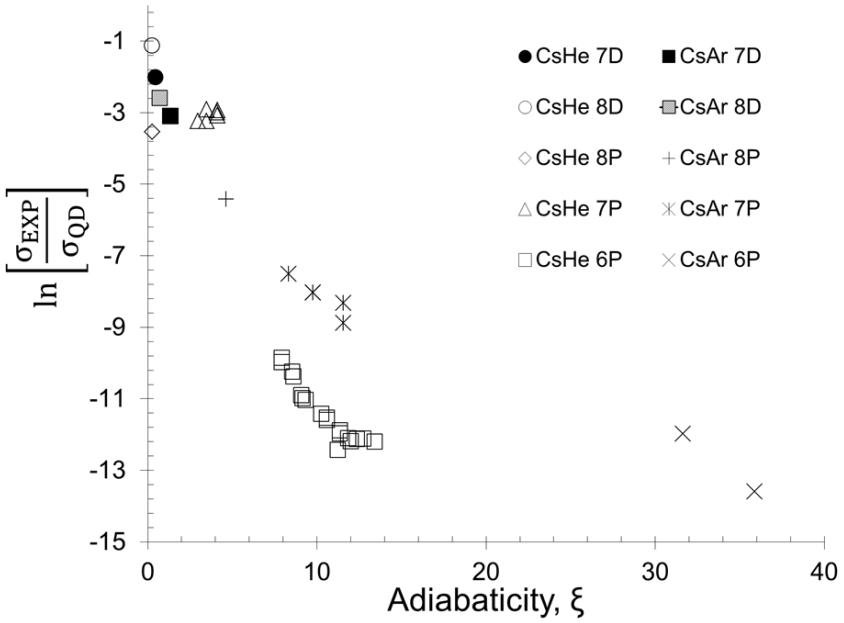

Figure 3.9: The log probabilities are plotted against the calculated adiabaticities where open and closed symbols represent Cs and He, Ar collisions, respectively for different energy states. The open and closed circles represent the experimental 7^2D measurements from this study.

and $\sigma_Q = 5.25 \pm 0.07 \times 10^{-16}\ cm^2$, respectively. The uncertainty in the cross-sections represent the 95% confidence bounds in the unweighted linear fits. Similarly, for Ar, the calculated spin-orbit rate is $k_{21} = 1.52 \pm 0.05 \times 10^{-10}\ cm^3/sec$ and the quenching rate is $k_Q = 2.65 \pm 0.04 \times 10^{-11}\ cm^3/sec$. For an average temperature of 40°C, the respective spin-orbit and quenching cross sections are $\sigma_{21} = 3.3 \pm 0.1 \times 10^{-15}\ cm^2$ and $\sigma_Q = 5.67 \pm 0.09 \times 10^{-16}\ cm^2$, respectively. The intercept for the helium Stern-Volmer plot provides a collisionless lifetime of $148 \pm 42\ ns$, with the lower bound near the radiative lifetime measurement of 98 ns [79].

3.5 Discussion

Figure 3.9 shows experimental Cs and He, Ar cross-sections, converted into probabilities and plotted against their respective adiabaticities. The 7^2D cross-section measurements are combined with the Cs - He, Ar collision database (8^2P, 7^2P and 6^2P) values discdussed in the recent adiabaticity study [39]. The fine structure splitting for Cs 7^2D is 21 cm^{-1} compared to the 83 cm^{-1} for Cs 8^2P, 181 cm^{-1} for Cs 7^2P and 554 cm^{-1} for Cs 6^2P. The current results represent more impulsive, less adiabatic collision conditions, resulting in higher transfer probabilities. For the same adiabaticity, the high polarizability of the rare gas collision partners enhances the transfer probability [39]. The atoms' polarizability increases the interaction length which is directly proportional to adiabaticity. It is unlikely that the added channel of ro-vibrational excitation in a molecular collision partner will significantly increase the transfer rate, as has been characterized for Rb $5P$ [107]. The rare gas collision probability is already very high.

3.6 Conclusions

Collision induced mixing between the $Cs7^2D_{5/2,3/2}$ states is exceptionally fast, driven by the large radius of the valence electron and small energy splitting. The helium rate exceeds that for argon by a factor of 7.4 due to both the higher relative speed and the more impulsive nature of the collision. The quenching rates are moderately fast, but 46 and 16 times slower than the mixing rates for helium and argon, respectively. The rates suggest efficient lasing may be achieved on several competing transitions.

IV. Time Resolved Fine Structure Mixing of Cesium $8\,^2D$ Induced by Helium and Argon

4.1 Introduction

The Diode Pumped Alkali Laser (DPAL) was originally conceived in 2003 as an alternative to existing multi-kilowatt-class laser systems due to its high efficiency and beam-quality [69, 70]. This three-level laser system uses a high pressure (1-10 atmosphere) buffer gas to provide spin-orbit mixing of the first excited ^2P states of the alkali vapor with diode pump-relax-lasing cycle times as short as 74 psec [54]. DPAL performance is optimized when spin-orbit relaxation is faster than the optical excitation rate [46, 48, 71]. Energy pooling can lead to the production of higher lying states and additional pump photons can ionize the gas. The role of ionization in laser performance has been investigated in particular for the Cs DPAL system [7, 62]. Further analysis of the degree of ionization depends on collisional relaxation of these higher lying states. More recently, optically pumped alkali vapor lasers have been demonstrated by excitation of the higher lying states, producing wavelengths extending from the blue to the mid infrared [18, 22, 84, 94, 103, 113]. In particular, we have recently demonstrated a scalable mid infrared Cs laser pumped by two-photon excitation of the $6\,^2S_{1/2} \rightarrow n\,^2D_{5/2,3/2}$ states [94]. Threshold is low enough to allow diode pumping. This system may find applications as a source for infrared counter measures [92, 96]. However, the cascade lasing mechanism depends on rapid fine structure mixing and modest quenching rates. A full assessment of these emerging laser systems requires accurate rate data.

Fine structure mixing in atomic alkali metal vapors upon collisions with rare gases has been studied extensively and several excellent reviews have been published [38, 39, 67, 88, 125]. The rates depend critically on the size of the fine structure energy gap, reduced mass and polarizability of the collision pair, and degree of electronic excitation. The temperature

dependence of the rates has received less attention, with the early work in the lowest P states of Cs and Rb providing the greatest temperature range [41]. In an attempt to correlate the large experimental data base with a few parameters, we have recently developed a scaling law based on adiabaticity using time dependent perturbation theory [38, 39]. Collisions of the higher lying Cs D states with helium are particularly impulsive. The fine structure splitting for the $6\,^2P_{1/2,\,3/2}$ state is 554 cm^{-1} (highly adiabatic), but the higher lying $n\,^2D_{3/2,\,5/2}$ splitting ranges from $97.6 - 7.1$ cm^{-1} for $n = 5 - 9$ (highly impulsive).

The fine structure mixing in cesium has been studied previously for the $n = 6 - 8\,^2P_{3/2,\,1/2}$ and $n = 6, 8 - 14\,^2D_{5/2,\,3/2}$ states [31, 33, 41, 55, 67, 68, 77, 85, 98, 115]. The work prior to 2003 is nicely reviewed in reference [125]. More recently, the mixing rates for the $n = 6$ and $7\,^2D_{5/2,\,3/2}$ states have been measured with cross-sections for helium of 0.54 and $0.96 \times 10^{-14} cm^2$, or $11 - 13\%$ of the quantum defect cross-section values, respectively [31, 35]. Quantum Defect Theory (QDT) [110] provides analytic expressions for expectation value of the valence electron's nuclear distance, accounting for incomplete screening of the inner electrons. We use QDT to provide an upper bound on the mixing rate and convert observed rates to probabilities per collision, as defined in Equation (4.7) below. The prior continuous wave (cw) laser-induced fluorescence (LIF) work by Jackowska [55] and Lukaszewski [77] for the $n = 8$ and $9\,^2D$ states exhibit He cross-sections at 29% and 14% of the quantum defect values, respectively. The decline in probability for the $n > 8$ states is particularly interesting. The rates for quenching, or inter-multiplet mixing (l-mixing), appear to increase relative to fine structure mixing (j-mixing) as the principal quantum number increases, [77] and could pose efficiency limitations for the optically pumped lasers. The influence of polarizibility on the Cs-rare gas mixing rates is of particular importance in selection of laser buffer gas [39, 77]. In the present work we re-examine the $8\,^2D_{3/2,\,5/2}$ mixing rates induced by helium and argon using pulsed lifetime

techniques. The complementary advantages of pulsed and cw energy transfer studies are often useful in rate validation [125].

4.2 Methods

The pulsed laser induced fluorescence apparatus using two-photon excitation to pump the Cs $6\,^2S_{1/2} \rightarrow 8\,^2D_{3/2,5/2}$ is shown in Figure 4.1. A frequency-doubled Quanta-Ray Pro Series pulsed Nd:YAG laser (10 Hz , $0-1$ $J/pulse$, 532 nm) is used to pump a Sirah model PRSC-D-1800 dye laser with LDS-722 dye tuned to populate the Cs $8^2D_{3/2}$ or $8^2D_{5/2}$ levels at 719.1 or 718.8 nm. The dye laser provides $6-10$ ns pulses in a 1 mm radius spot as the energy is tuned from 0 to 30 $mJ/pulse$ by varying the Nd:YAG flash-lamp energy. The pump intensity of 100 MW/cm^2 is more than sufficient to bleach the two-photon absorption. By using excitation through the virtual state rather than the two wavelength sequential excitation through the 6^2P state as used in the prior work [55], the effects of radiation trapping for emission terminating on the 6^2P levels is reduced. The Cs cell is a 12 cm long and 2.54 cm diameter heatpipe [61]. The alkali melt pool is maintained at T = 45°C, yielding a saturated vapor cesium density of 3.09×10^{11} cm^{-3}. Radiation trapping is not apparent in this apparatus until T > 75°C [35]. The rare gas species, He or Ar, were monitored by two MKS Instruments 690A Baratron capacitance manometers with ranges of 1000 $Torr$ and 10 $Torr$. An aluminum heater block encloses the cell with a Watlow temperature controller connected to eight cartridge heaters and a thermocouple on a negative-feedback loop to control the cell temperature.

The fluorescence of the excited $8\,^2D_{3/2}$ state is collected by an $f/1.7$ lens in an end-on configuration and detected by a C31034A photomultiplier tube using a bandpass filter to limit emission to the Cs $8\,^2D_{3/2} \rightarrow 6\,^2P_{1/2}$ transition at 601.1 nm. The 10 nm band pass is sufficient to isolated emission from the $8\,^2D_{3/2}$ state, since the $8\,^2D_{5/2} \rightarrow 6\,^2P_{1/2}$ transition is forbidden and the two transitions from $8\,^2D_{5/2,3/2}$ to $6\,^2P_{3/2}$ occur at 621.76 and 621.31 nm. The filter dramatically improves throughput relative the monochromator used

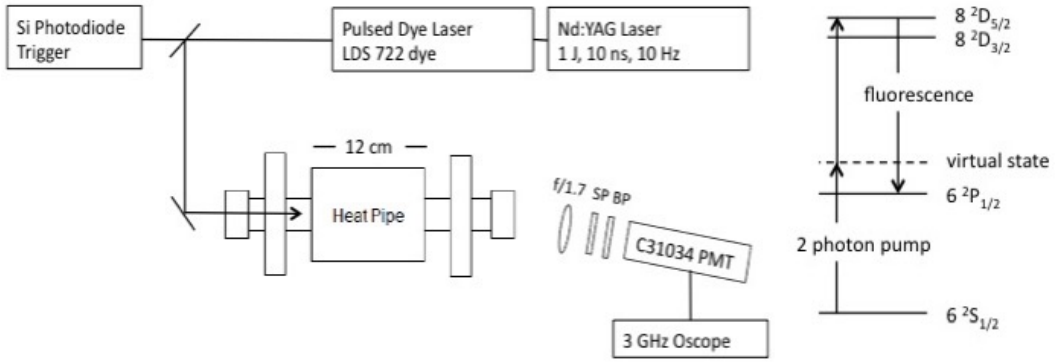

Figure 4.1: Temporally-resolved laser induced fluorescence apparatus and cesium energy levels for the 8 ^2D fine structure collisional mixing.

in the older study [55]. A 700 *nm* shortpass filter was also used to minimize scattered pump light. Scattered pump laser intensity was measured off resonance and subtracted from the observed decay profiles.

4.3 Results

The time resolved fluorescence from the collisionally populated 8 $^2D_{3/2}$ state after two-photon excitation of the 8 $^2D_{5/2}$ state for various helium pressures is provided in Figure 4.2. Emission from this collisionally populated state is minimal for no added helium and depends only on Cs - Cs collisions. The rate for fine structure mixing induced by helium is very rapid. With the addition of just 0.1 $Torr$ of helium, significant population is transfered from the pumped 8 $^2D_{5/2}$ state within 60 ns. At 1 $Torr$ the rise time is shorter than the pump pulse duration and only the longer quenching decay can be observed. At the higher pressures the peak signal decreases due to quenching during the excitation pulse.

The emission signal is quite strong, with a signal-to-noise ratio exceeding 50, as seen in the logarithmic plot of Figure 4.3. The decay is well monitored for time scales exceeding 7 multiples of the slowest eigenvalue. The long-term decay is clearly single exponential at the lower pressure and no indication of radiation trapping is present.

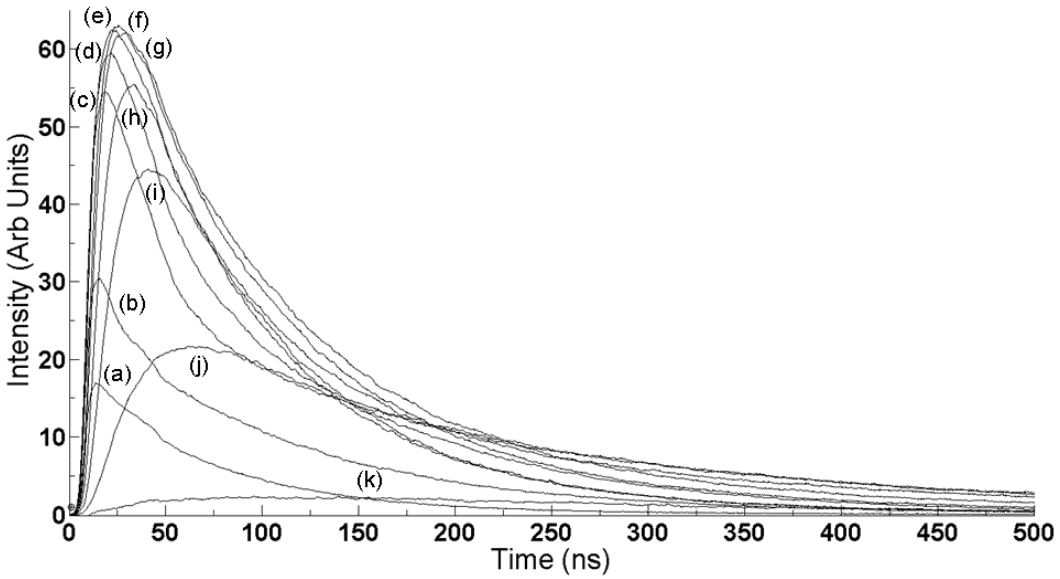

Figure 4.2: Fluorescence decay curves of the Cs $8\,^2D_{3/2} \rightarrow 6\,^2P_{1/2}$ emission after excitation of $8\,^2D_{5/2}$ at 50°C for helium buffer gas pressures in Torr (a) 100, (b) 50, (c) 10, (d) 5, (e) 2.5, (f) 1, (g) 0.8, (h) 0.5, (i) 0.3, (j) 0.1 (k) 0.

To extract mixing and quenching rates from the observed temporal profiles, solutions are sought to the first order, system of linear differential rate equations [35]:

$$\frac{n_2(t)}{dt} = -\left(\Gamma_2 + Q_2 + R_{21}\right) n_2(t) + R_{12} n_1(t) \tag{4.1}$$

$$\frac{n_1(t)}{dt} = -\left(\Gamma_1 + Q_1 + R_{12}\right) n_1(t) + R_{21} n_2(t) \tag{4.2}$$

for the populations $n_2 = [\mathrm{Cs}(8\,^2D_{5/2})]$ and $n_1 = [\mathrm{Cs}(8\,^2D_{3/2})]$. In these equations the total radiative rates from the pumped $8^2D_{5/2}$ and observed $8^2D_{5/2}$ states to all lower levels, are denoted Γ_2 and Γ_1. Similarly, the quenching rates are defined as $Q_2 = k_2 M$ and $Q_1 = k_1 M$ where M = the rare gas concentration. The fine structure mixing rates obey the detailed balance:

$$R_{12} = R_{21}\frac{g_2}{g_1} e^{-\Delta E/k_b T} = R_{21}\rho \tag{4.3}$$

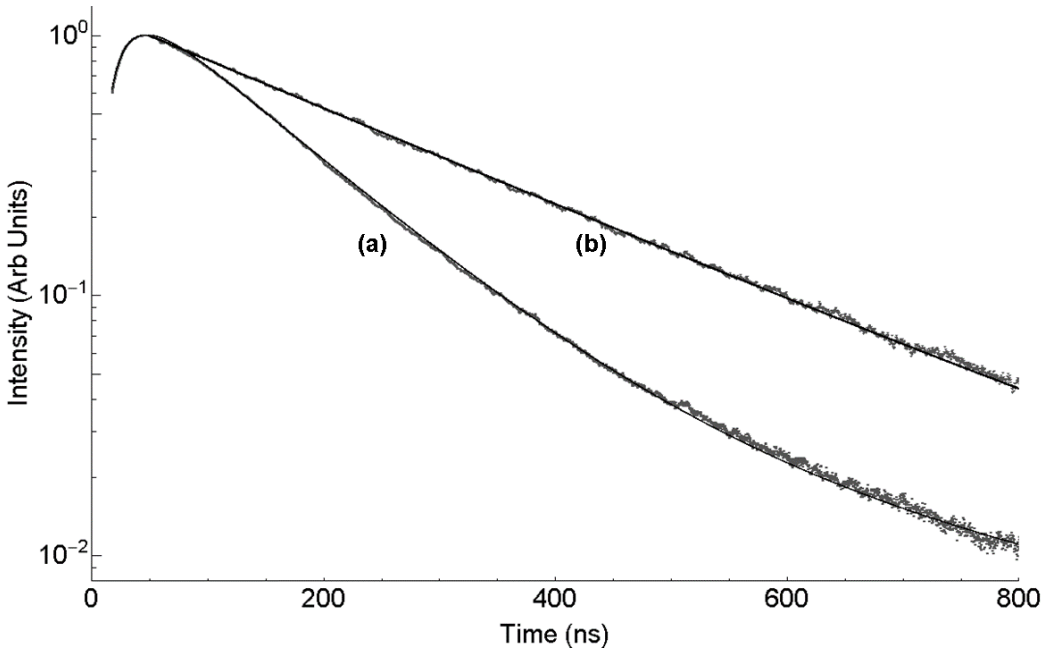

Figure 4.3: Emission on $8\,^2D_{3/2} \rightarrow 6\,^2P_{1/2}$ at 601 *nm* after excitation on $8\,^2D_{5/2}$ for Ar pressures of (a) 200 *Torr* and (b) 0.6 *Torr*. A fit to Equation (4.1) is also provided.

and are proportional to the rare gas density, $R_{21} = k_{21}M$. The eigensolutions after instantaneous, selective laser excitation of $8^2D_{5/2}$ for the satellite population is:

$$n_1(t) = A\left(e^{\lambda_+ t} - e^{\lambda_- t}\right) \tag{4.4}$$

The observed intensities are proportional to the emitter concentration and the amplitude A is not required to define the decay rates. For high rare gas densities where $R_{12} - R_{21} >> \Gamma_1 - \Gamma_2$ and assuming quenching rates independent of J, $k_2 = k_1 = k$, the eigenvalues can be simplified [31, 35, 77, 85] to:

$$\lambda_+ = \frac{\Gamma_1 + \Gamma_2}{2} - \left(\frac{\rho - 1}{\rho + 1}\right)\frac{\Gamma_1 - \Gamma_2}{2} + k \tag{4.5}$$

$$\lambda_- = \frac{\Gamma_1 + \Gamma_2}{2} + \left(\frac{\rho - 1}{\rho + 1}\right)\frac{\Gamma_1 - \Gamma_2}{2} + k + (\rho + 1)\,k_{21} \tag{4.6}$$

The rate coefficients can be converted to collision cross-sections, σ, using the average relative speed of the collision pair, v : $k_{21} = v\sigma_{21}$ and $k = v\sigma_Q$.

For each pressure, the decay curves, such as those in Figure 4.2, were fit to the double exponential function outlined in Equation (4.4). The pressure dependence of the fit eigenvalues are displayed as Stern-Volmer plots for He in Figure 4.4 and Ar in Figure 4.5.

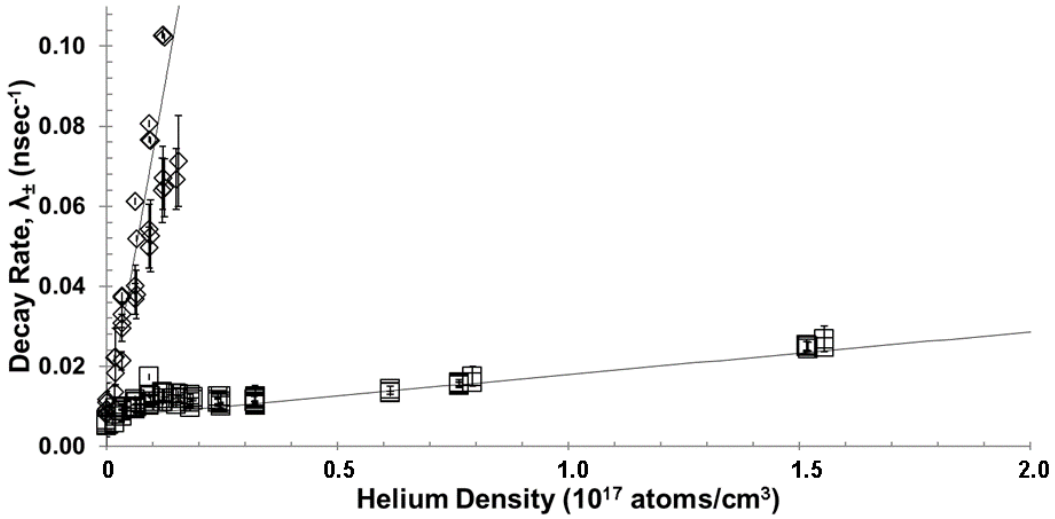

Figure 4.4: Stern-Volmer plot of experimentally derived rates for helium at a temperature of 45°C. The solid lines are a least-squares linear fits yielding the experimentally derived fine structure mixing and quenching rates.

For He, the experimentally calculated spin-orbit rate is derived from the slope of the pressure dependent eigenvalue λ_- as shown in Figure 4.4. The slope is $6.5 \pm 0.5 \times 10^{-9}\ cm^3/sec$ yielding a fine structure relaxation rate of $k_{21} = 2.6 \pm 0.2 \times 10^{-9}\ cm^3/sec$. From the slope of λ_+ we obtain the quenching rate $k_Q = 1.07 \pm 0.04 \times 10^{-10}\ cm^3/sec$. For an average heat pipe temperature of 45°C, the respective spin-orbit and quenching cross sections are $\sigma_{21} = 2.0 \pm 0.2 \times 10^{-14}\ cm^2$ and $\sigma_Q = 8.1 \pm 0.3 \times 10^{-16}\ cm^2$, respectively. The uncertainty in the cross-sections represent the 95% confidence bounds in the unweighted linear fits. The upper limit on eigenvalue determination is imposed by the finite dye laser pulse duration.

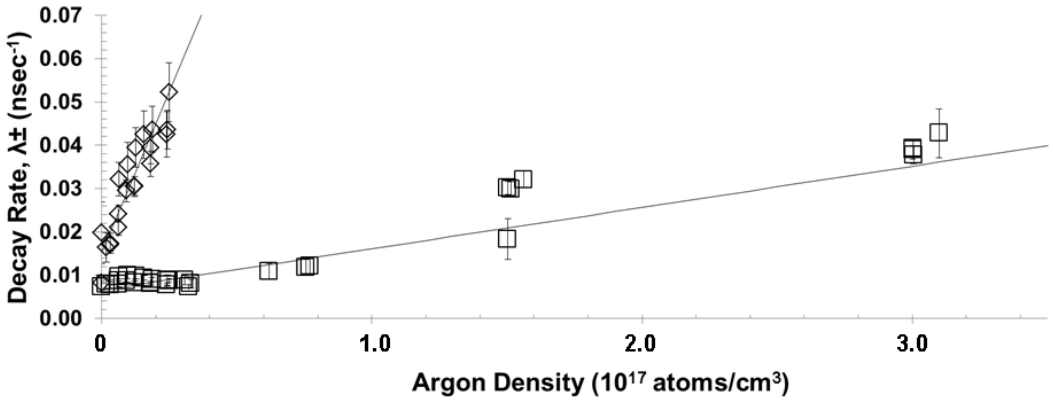

Figure 4.5: Stern-Volmer plot of experimentally derived rates for argon at a temperature of 45°C.

Similarly, for Ar, the calculated spin-orbit rate is $k_{21} = 5.2 \pm 0.4 \times 10^{-10}\ cm^3/sec$ and the quenching rate is $k_Q = 9.5 \pm 0.7 \times 10^{-11}\ cm^3/sec$. For an average temperature of 45°C, the respective spin-orbit and quenching cross sections are $\sigma_{21} = 1.10 \pm 0.09 \times 10^{-14}\ cm^2$ and $\sigma_Q = 2.0 \pm 0.1 \times 10^{-15}\ cm^2$, respectively. The intercept for the helium Stern-Volmer plot provides a collisionless lifetime of $119 \pm 57\ ns$, with the upper bound near the radiative lifetime measurement of $154 \pm 5\ ns$ [80].

4.4 Discussion

The current results for the fine structure mixing cross-sections are compared with prior observations in Table 4.1 [31, 35, 55, 77]. The corresponding quenching rates are summarized in Table 4.2. The only prior reported mixing rates for the 8^2D state agree favorably with the present results for collisions with Ar. The statistical error in the current observations is lower, about 9%. Usually the cw intensity analysis used in the earlier work provides improved signal to noise due to the higher average power from cw sources. However, the prior work used time integrated intensities from pulsed excitation and does not realize this duty cycle advantage. The prior work was performed at higher

temperature, and thus higher Cs density and increased source intensity, but suffered from reduced throughput of the grating spectrometer. The two results agree within the statistical error bounds.

Table 4.1: Fine structure mixing cross-section $\left(10^{-14}\ cm^2\right)$.

	He		Ar		Reference	T(K)
	σ_{21}	$P = \sigma_{21} / \sigma_{QD}$	σ_{21}	$P = \sigma_{21} / \sigma_{QD}$		
$6\,^2D$	0.54 ± 0.15	0.069	0.17 ± 0.05	0.0005	[31]	350 ± 20
$7\,^2D$	0.96 ± 0.04	0.128	0.33 ± 0.01	0.041	[35]	313
$8\,^2D$	2.00 ± 0.20	0.106	1.10 ± 0.09	0.056	this work	318
$8\,^2D$	5.52 ± 0.83	0.292	1.33 ± 0.21	0.068	[55]	360
$9\,^2D$	5.15 ± 0.77	0.141	1.50 ± 0.27	0.040	[55]	360
$10\,^2D$	5.03 ± 1.00	0.078	2.11 ± 0.42	0.032	[77]	353
$11\,^2D$	3.30 ± 0.66	0.031	2.63 ± 0.54	0.025	[77]	353
$12\,^2D$	2.08 ± 0.54	0.013	2.62 ± 0.67	0.016	[77]	353
$13\,^2D$	1.75 ± 0.54	0.007	2.68 ± 0.80	0.011	[77]	353
$14\,^2D$	1.07 ± 0.33	0.003	2.60 ± 0.80	0.007	[77]	353

The case of helium requires more attention. The current cross section measurement is 2.7 times lower than reported in reference [55]. The steady state approach used in the prior work measures the rate relative to the radiative rate and could be influence by systematic errors due to radiation trapping. Indeed, considerably higher Cs densities were employed and the first P state is optically pumped. Trapping should effect both the He and Ar rate determinations, but diffusion is different for the two gases and it is possible the Cs density varies between the two cases. In our case, trapping becomes very evident from multi exponential behavior at long decay times, but is clearly avoided by limiting

Table 4.2: Quenching cross-section $\left(10^{-14}\ cm^2\right)$.

		σ_{12}	$P = \sigma_{12}\ /\ \sigma_{QD}$	σ_Q	Reference	T(K)
Cs-He	$6\,^2D_{5/2} \rightarrow 6\,^2D_{3/2}$	0.54 ± 0.15	0.069	0.026 ± 0.012	[31]	350 ± 20
	$7\,^2D_{5/2} \rightarrow 7\,^2D_{3/2}$	0.96 ± 0.04	0.128	0.0525 ± 0.0007	[35]	313
	$8\,^2D_{5/2} \rightarrow 8\,^2D_{3/2}$	2.00 ± 0.20	0.106	0.0809 ± 0.003	this study	318
Cs-Ar	$6\,^2D_{5/2} \rightarrow 6\,^2D_{3/2}$	0.17 ± 0.05	0.0005	0.0003 ± 0.0001	[31]	350 ± 20
	$7\,^2D_{5/2} \rightarrow 7\,^2D_{3/2}$	0.33 ± 0.01	0.041	0.0567 ± 0.0009	[35]	313
	$8\,^2D_{5/2} \rightarrow 8\,^2D_{3/2}$	1.10 ± 0.09	0.056	0.203 ± 0.001	this study	318
Cs-Xe	$9\,^2D_{3/2} \rightarrow 9\,^2D_{5/2}$	2.13	0.055		[76]	360
	$10\,^2D_{3/2} \rightarrow 10\,^2D_{5/2}$	5.78	0.086		[55]	393
	$11\,^2D_{3/2} \rightarrow 11\,^2D_{5/2}$	13.5	0.124	0.0030 ± 0.0003	[34]	393
	$12\,^2D_{3/2} \rightarrow 12\,^2D_{5/2}$	28.9	0.120	0.0044 ± 0.0004	[34]	393
	$14\,^2D_{3/2} \rightarrow 14\,^2D_{5/2}$	18.8	0.052	0.0150 ± 0.0015	[34]	393
	$15\,^2D_{3/2} \rightarrow 15\,^2D_{5/2}$			0.0190 ± 0.0020	[34]	393
Rb-He	$9\,^2D_{3/2} \rightarrow 9\,^2D_{5/2}$	5.1 ± 1.0	0.08	0.11 ± 0.02	[53]	520
	$10\,^2D_{3/2} \rightarrow 10\,^2D_{5/2}$	4.55 ± 1.50	0.04	0.15 ± 0.02	[53]	520
	$11\,^2D_{3/2} \rightarrow 11\,^2D_{5/2}$	2.2 ± 0.6	0.01	0.29 ± 0.05	[53]	520
	$15\,^2D_{3/2} \rightarrow 15\,^2D_{5/2}$			1.3 ± 0.4	[53]	520

the melt pool temperature. The discrepancy on the helium rates is more likely a result of the rapid rate, whose rate coefficient is five times greater than Ar. Indeed the prior work notes the limited low pressure sampling for their He data. Furthermore, quenching during the unspecified duration of their laser excitation could reduce the integrated intensities and bias the rate measurement. Finally, it is worth noting that the prior study was unable to discern the quenching rates, which depend on the intercepts of their integrated intensity Stern-Volmer plots. We clearly observe rapid quenching from the pressure dependence

of the slower eigenvalue in Figure 4.2. By directly observing the temporal profiles and increasing the signal to noise ratio, we believe the current rates are preferred.

The fine structure transition probabilities are defined in Tables 4.1 and 4.2 by the ratio of the experimentally measured cross section, σ_{21} and the quantum defect cross section, σ_{QD},

$$P = \frac{\sigma_{21}}{\sigma_{QD}} \tag{4.7}$$

with

$$\sigma_{QD} = \pi \left(\langle r \rangle + r_{Rg} \right)^2 \tag{4.8}$$

where $\langle r \rangle$ is the expectation value of the Cs atom's electron position and r_{Rg} is the effective radius of the rare gas atom [39]. Since the alkalis are well represented by hydrogenic approximations [124], the expectation value of the electron position is given by

$$\langle r \rangle = a_\mu \, (n^*)^2 \left(1 + \frac{1}{2} \left(1 - \frac{l(l+1)}{(n^*)^2} \right) \right) \tag{4.9}$$

where a_μ is the effective Bohr radius of the alkali, l is the angular momentum quantum number and n^* is the effective quantum number given by

$$n^* = \sqrt{\frac{E_{Ryd}}{T - E}} \tag{4.10}$$

In Equation (4.10) E_{Ryd} is the Rydberg energy (109737.32 cm^{-1}), T is the ionization energy and E is the energy level corresponding to the effective quantum number. The effective quantum number for $8^2D_{5/2,3/2}$ are 5.53 and 5.52, respectively. The currently measured probabilities for 8^2D fine structure mixing are $p = 0.106$ for helium and less, $p = 0.056$ for Ar. The higher probability for helium reflects are more impulsive collision, as discussed below. The probabilities for quenching are less, but sizeable, $p = 0.04$ for He and $p = 0.02$ for Ar.

The extent to which the alkali doublet transfer collision with the rare gas species is sudden or adiabatic depends on the interatomic velocity as well as the spin-orbit splitting

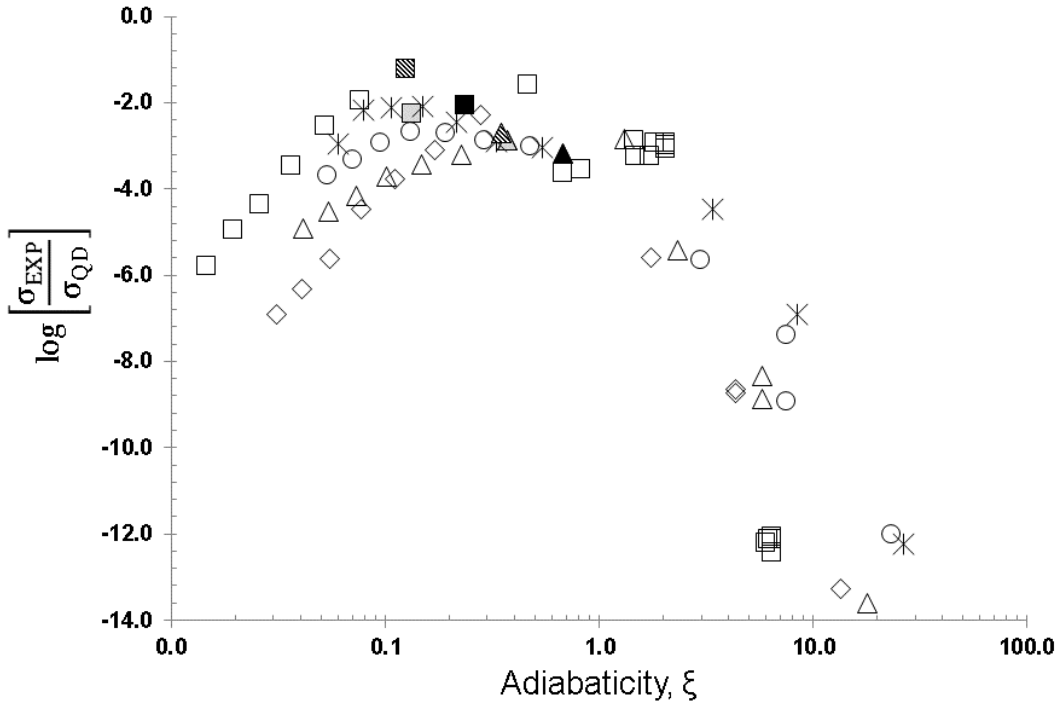

Figure 4.6: The log probabilities are plotted against the calculated adiabaticities where □ - Cs-He, ∗ - Cs-Xe, ○ - Cs-Kr, △ - Cs-Ar, and ◇ - Cs-Ne collisions. The black filled square and triangle represent experimental 7^2D measurements from [35], The hatched filled square and triangle represent experimental 8^2D measurements from [55] and the gray shaded square and triangle represent 8^2D measurements from this study.

[41]. For the alkali-rare gas collision the adiabaticity is defined as [37]

$$\xi = \frac{\tau_c}{\tau_v} = \frac{\Delta L}{\bar{v}} \tag{4.11}$$

where τ_c is the duration of the collision, τ_v is the period of oscillation, Δ is the spin-orbit splitting, L is the interaction length and $\bar{v}$ is the mean relative speed. Using the results of [39], we set the interaction length, L, to 5Å despite not knowing how the potential energy surfaces trend.

Figure 4.6 shows experimental Cs and various buffer gas cross-sections, converted into probabilities and plotted against their respective adiabaticities. The current 8^2D cross-

section measurements are incorporated with an extensive Cs - buffer gas collision database (8^2P, 7^2P, 6^2P and $8^2 - 15^2D$) discussed in the recent adiabaticity study [39] and extended to include Cs 7^2D thru 14^2D using measured data from [35, 55, 77]. The fine structure splitting for Cs 8^2D is 11 cm^{-1} compared to the 554 cm^{-1} for Cs 6^2P at the lower bound and 1.3 cm^{-1} for Cs 14^2D at the upper bound. The current results represent more impulsive, less adiabatic collision conditions, resulting in higher transfer probabilities up to Cs 8^2D. For Cs-He and Cs-Ar collisions, the transfer probabilities decrease starting at Cs 8^2D and a similar trend is noticed for the other Cs collision partners as shown in Figure 4.6. This trend does not represent a collapse of the adiabatic argument for the collision, rather it shows a failure of the system to account for all the energy levels that will contribute to the probability. The higher lying states tend to have many nearby states, shown in Figure 4.7. They are no longer electronically isolated and we would expect the total energy transfer cross-section to be fully governed by the adiabatic argument whereas a single cross-section would not. This total cross-section can be represented by the sum of the spin-orbit mixing cross-section and the quenching cross-section of the state of interest. Unfortunately, all of the previous work except for [34] did not publish the quenching cross-sections. The few published quenching cross-sections do show the expected trend of increasing with increasing excitation. Measured quenching cross-sections [34, 53], σ_Q, detailed in Table 4.2 show increasing quenching cross-sections as the ratio of the measured spin-orbit cross-sections to quantum defect cross-sections decreases for Rb-He and Cs-Xe for increasing n^2D states.

Another trend that is seen in Figure 4.6 is the behavior of the probability with various collision partners. The trend predicted by [39] and observed by [41, 66] is that the probability should be highest for the Cs-He collision, decrease for Cs-Ne and then increase slowly from Ar to Xe. This is precisely the behavior that is observed in the energy transfer probabilities for the Cs-rare gas D-states and arises from the interplay of the relative

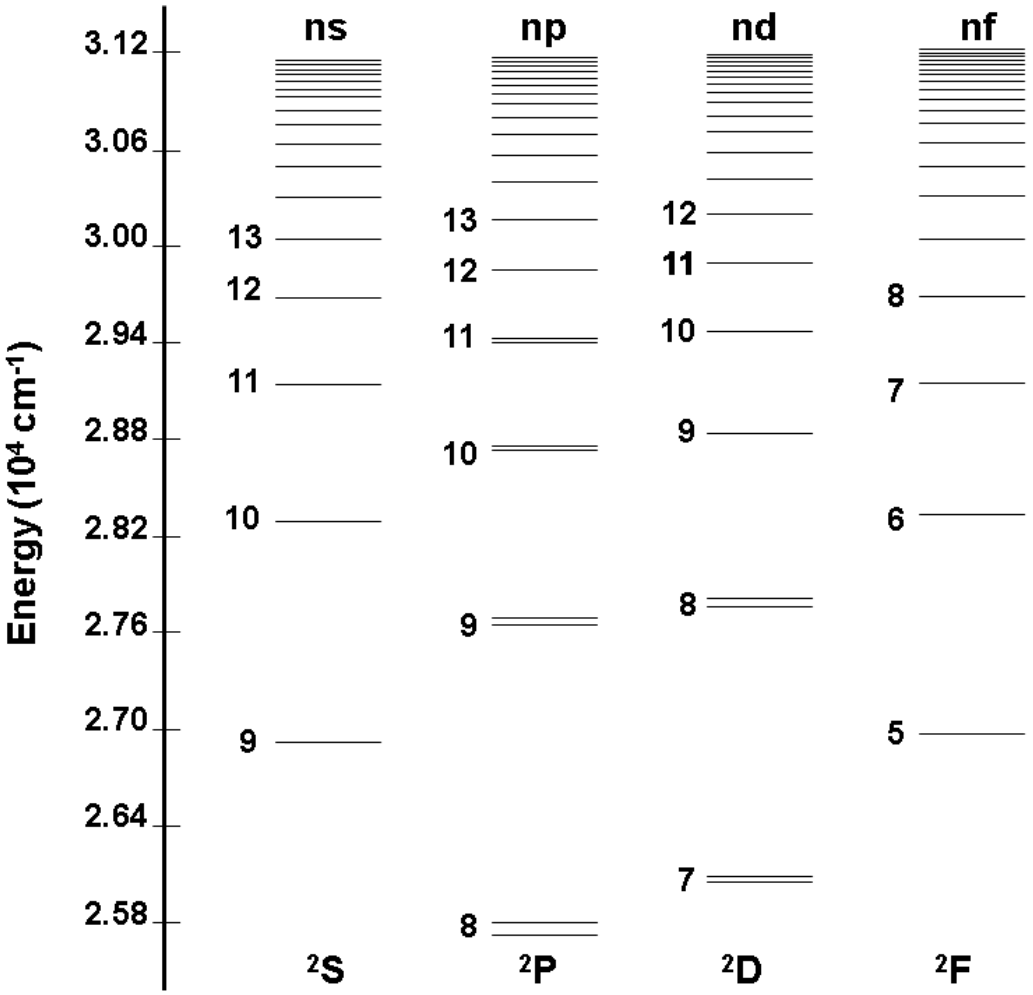

Figure 4.7: Grotrian diagram of electronic states of cesium.

velocity and polarizability of the collision partner. The total cross-sections would also be expected to share this trend.

Predictions of the temperature dependence for the Cs 8^2D fine structure mixing rates are compared with the observations in Figure 4.8. An analytic expression for the probability of energy transfer in alkali-metal-rare gas collisions was recently derived using time-dependent perturbation theory [38]. The rate depends principally on the adiabaticity, ξ, defined in Equation (4.11). When the interaction potential changes rapidly during the collision (suddenly), the probability for energy transfer is enhanced. The temperature

dependence of the mixing rate coefficient is [38]:

$$k_{21}(T) = \frac{V_o^2 L^4}{2\pi\hbar^2 \bar{v}} \xi^{-2} \left(A^2 + B^2\right) \tag{4.12}$$

where

$$A^2 + B^2 = 2e^{-4\pi^2\left(\frac{w}{L}\right)^2 \xi^2} \pi^3 \left(\frac{w}{L}\right)^2 \xi^2 + \left[1 - 2\sqrt{2}\pi\left(\frac{w}{L}\right)\xi \mathcal{F}\left(\sqrt{2}\pi\left(\frac{w}{L}\right)\xi\right)\right]^2$$

$$\mathcal{F}(x) = \frac{1}{2} e^{-x^2} Erf(x)$$

V_o = magnitude of the interaction potential

L = interaction length

$\bar{v} = \sqrt{8k_b T/\pi\mu} \equiv$ average relative speed

w = length scale for the rapidly changing region of the interaction potential

The temperature dependence arises from the velocity dependence of the adiabaticity, $\xi = L/\bar{v}$.

The prediction from Equation (4.12) using $L = 5$Å, $w = 3$Å, $V_o = 0.1119$ Hartree for He and 0.1221 H for Ar and temperatures of $T = 100 - 1200$ K is provided in Figure 4.8. The current and prior Ar mixing rates were determined at somewhat different temperatures, and the trend is strikingly similar to the prediction from the perturbation theory. For helium, the collision is very sudden, and the rate coefficient approaches the gas kinetic, or probability $p = 1$, limit. The difference in interaction magnitude, V_o, for helium and argon is small and was obtained from the lowest $6P$ state [38]. Again, the prior reported rate for He appears inconsistent with the theoretical prediction.

4.5 Conclusions

Collision induced mixing between the $8^2D_{5/2,3/2}$ states is exceptionally fast, driven by the large radius of the valence electron and small energy splitting. The helium rate exceeds that for argon by a factor of 5 due to both the higher relative speed and the more impulsive nature of the collision. The quenching rates are moderately fast, but 24 and 5 times slower

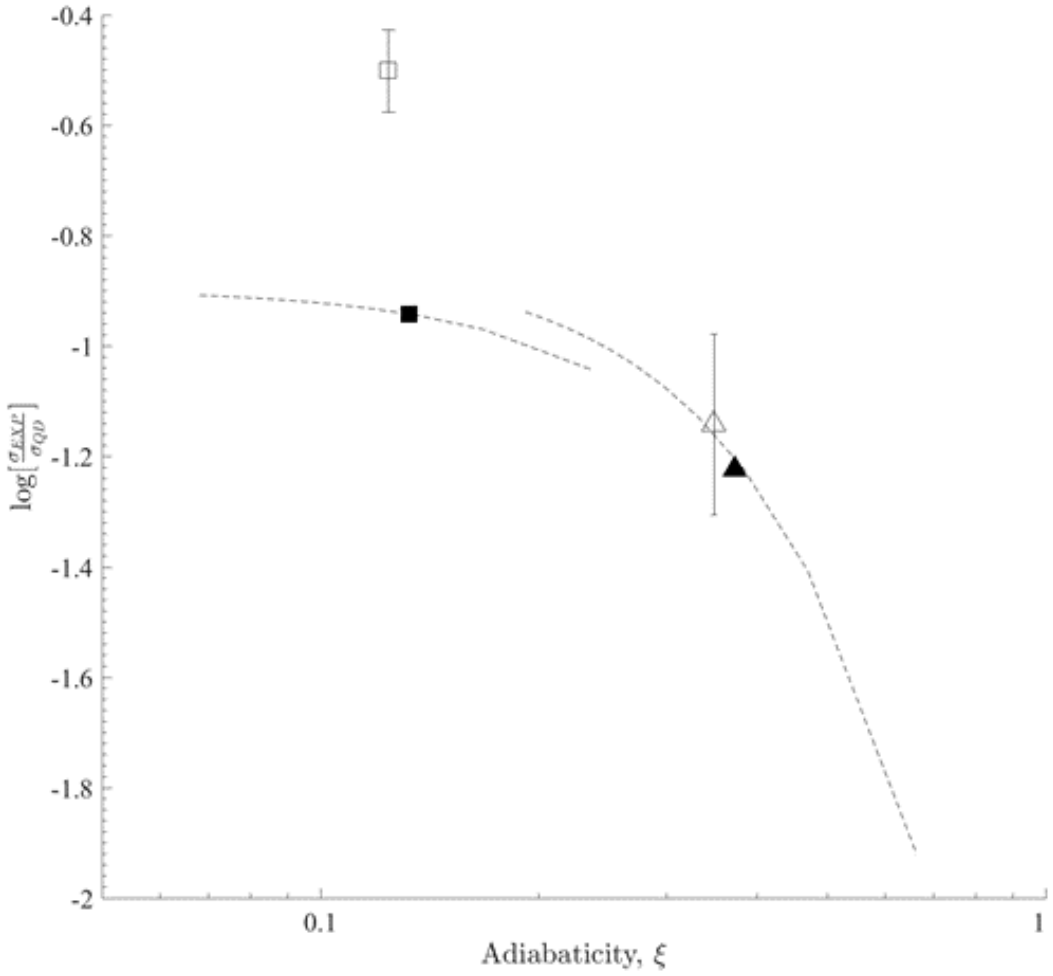

Figure 4.8: Temperature scaling for Cs 8^2D fine structure mixing rates for: (■,□) He and (▲,△) Ar from: (□,△) Reference [55] and (■,▲) present work. (− − −) Prediction from perturbation theory of Equation (4.12) using L = 5Å, w = 3Å, V_o = 0.1119 Hartree for He and 0.1221 H for Ar and temperatures T = 100 − 1200 K.

than the mixing rates for helium and argon, respectively. The rates suggest efficient lasing may be achieved on several competing transitions.

These rates are put in context of the previously measured spin-orbit cross-sections for Cs-rare gas pairs and are shown to agree well. The probability for energy transfer is shown to decrease with reduced adiabaticity which is in contrast to previous developments [37, 39]

and is driven by the non-isolated nature of the highly excited D-states. The total cross-section is still observed to follow adiabatic arguments for the probability of energy transfer. The probabilities are also seen to share the previously observed trend in the probability with collision partner.

V. Ultraviolet and Blue Stimulated Emission from Cs Alkali Vapor Pumped using Two-Photon Absorption

5.1 Introduction

The Diode Pumped Alkali Laser, a three-level laser system, is pumped by diode bars or stacks through the alkali's D_2 transition to its $^2P_{3/2}$ state, then collisionally relaxed to the $^2P_{1/2}$ state where it lases in the near-infrared (NIR) along the D_1 transition. DPAL performance is optimized when spin-orbit relaxation, with a buffer gas (usually a rare gas or small hydrocarbon), is much faster than the optical excitation rate [46, 48, 71]. A cesium (Cs) cw laser demonstrated near 1 kW output at 894.6 nm [15] and 1.5 kW for a potassium (K) DPAL at 770.1 nm [102], steps towards proving DPAL's capability as a high energy class laser; however, the alkali gain medium's ability to produce various beams at a variety of wavelengths from ultraviolet through long-wave infrared is a versatility that requires further study and measurements [40, 100, 113, 119]. Several comprehensive DPAL reviews [42, 71, 139] outline the benefits of this laser's high quantum efficiency, gaseous gain medium, reduced thermal issues, diode pumping and scalability to high output powers.

Several optically-pumped alkali lasers operating at alternative wavelengths have also been demonstrated and require excitation above the first alkali $^2P_{3/2}$ excited state [5, 19, 21, 22, 28, 52, 93, 103, 113, 119]. Ultraviolet and blue emission lasing, have been reported for K, rubidium (Rb) and Cs. For K, a blue spot at 404 nm was observed when pumping the K $4^2S_{1/2} \rightarrow 6^2S_{1/2}$ transition [103]. For a K vapor cell at 553K with 5.4 torr of helium (He) buffer gas, it was reported that the threshold was approximately 1 mJ/pulse and the slope efficiency for the blue beam increased by a factor of 4 as the number density increased by a factor of 2.5 [103]. It was theorized that both cascade lasing and 4-wave mixing may both be occurring and may also be in competition with one another for producing the blue beam [103].

For Rb, 100 mW of ultraviolet light at 398 nm was measured as a harmonic to 1 W of 794.8 nm beam output in an experiment for a Rb cell temperature of $T = 140°C$ [97]. As a harmonic of 794.8 nm, the 398 nm output emission can not be explained by either 4-wave mixing or cascade lasing. Additionally, 9.1 mW of Rb blue emission 420 nm $\left(6^2P_{3/2} \rightarrow 5^2S_{1/2}\right)$ for a Rb cell temperature of $T = 135°C$ (Rb vapor density, $n = 5 \times 10^{13}$ cm^{-3}) was measured using two pump lasers at 780 nm ($5^2S_{1/2} \rightarrow 5^26_{3/2}$) and 776 nm ($5^2P_{3/2} \rightarrow 5^2D_{5/2}$) and explained as a 4-wave mixing process [111]. A two-photon pump excitation, ($5^2S_{1/2} \rightarrow 5^2D_{5/2}$) was used to explore the Rb blue transitions $6^2P_{3/2,1/2} \rightarrow 5^2S_{1/2}$ for temperatures $T = 175°C$, $T = 200°C$ and $T = 250°C$ [119]. Maximum output power was 3.2 μJ for a pump power of 3.3 mJ and slope efficiencies increased from 0.03% to 0.5% for Rb as cell temperatures increased from $T = 175°C$ through 250°C.

Cs blue emission studies performed in [119] showed efficiencies on the order of $0.02 - 0.06\%$ for $T = 175 - 200°C$ for pump transition $6^2S_{1/2} \rightarrow 7^2D_{3/2}$ and blue emissions for the Cs $7^2P_{3/2,1/2} \rightarrow 6^2S_{1/2}$ transition. For a scaled Cs system, 10 μJ per pulse was achieved for 100 mW, 4 ns pump pulse at 10 Hz [119]. Recent measurements in [40] reported Cs ultraviolet $\left(8^2P_{3/2} \rightarrow 6^2S_{1/2}\right)$ and blue $\left(7^2P_{3/2} \rightarrow 6^2S_{1/2}\right)$ emissions after pumping the $6^2S_{1/2} \rightarrow 7^2D_{5/2}$ transition. Maximum powers achieved in this experiment were 700 nJ and 150 nJ for the ultraviolet and blue emissions, respectively for pump pulse power of 0.8 mJ [40]. Additional modulation studies conducted in [40] led to 4-wave mixing as the method for producing these ultraviolet and blue emissions.

Optically pumped alkali lasers at far-,mid-infrared, near-infrared, visible and ultraviolet wavelengths may be useful as beacons or illuminators for laser weapons, or for countermeasures [92]. Like the traditional DPAL, these higher energy states require knowing the transition rates, optical cross sections, collisional quenching and spin-orbit rates to understand the competing and cascading laser transitions and whether or not 4-wave mix-

ing is occurring concurrently. One such excitation scheme, depicted in Figure 5.1, uses

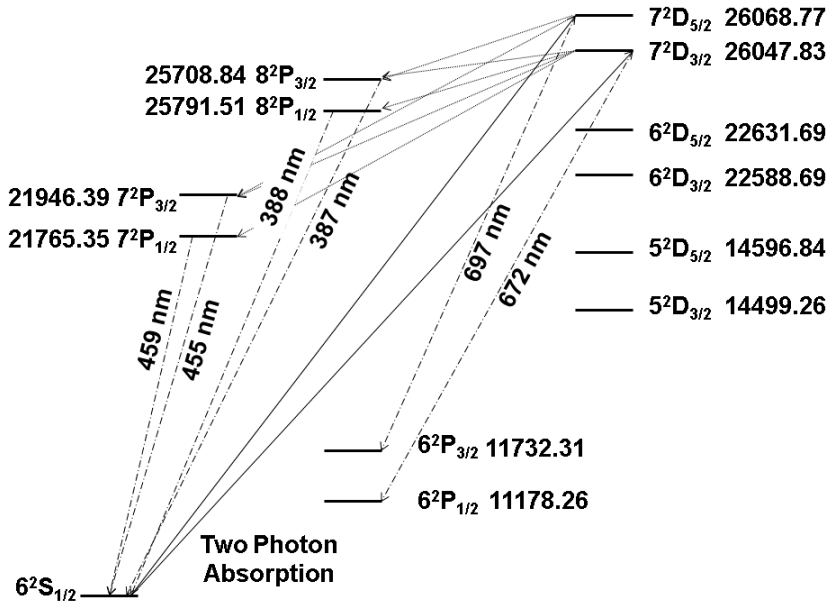

Figure 5.1: Cs energy level diagram.

two-photon direct excitation of the Cs ground state to Cs $7^2D_{5/2,\ 3/2}$ followed by primary infrared and visible transitions to the Cs 8^2P, 7^2P and 6^2P and secondary ultraviolet, blue and NIR transitions to the Cs $6^2S_{1/2}$ ground state.

This work extends the optically-pumped Cs vapor cell transition $6^2S_{1/2} \rightarrow 7^2D_{5/2}$ ultraviolet and blue emissions characterization study outlined in [40] by extending these same emissions for the Cs vapor cell pump transition $6^2S_{1/2} \rightarrow 7^2D_{3/2}$. A functional form equation detailed in [84] to quantitatively evaluate Rb near IR laser energy at 2.73 μm and 2.79 μm for Rb vapor cell transitions $6^2P_{3/2,1/2} \rightarrow 6^2S_{1/2}$, respectively, was applied in this study to assess the Cs ultraviolet and blue emissions. This equation, while not a theoretical solution to the Cs vapor cell emission performance, is sufficient to represent the pump threshold, bleached limit, slope efficiency dependence on pump energy providing further validation for the functional fit. Last, this study extends the Cs vapor cell blue

emission dependence on Cs vapor density outlined in [119] by including visible emissions at 150°C and validating that pump pulse versus blue beam energy dependence detailed in [119] include ultraviolet $8^2P_{3/2,1/2} \rightarrow 6^2S_{1/2}$ as well as blue $7^2P_{3/2,1/2} \rightarrow 6^2S_{1/2}$ emissions.

5.2 Experiment

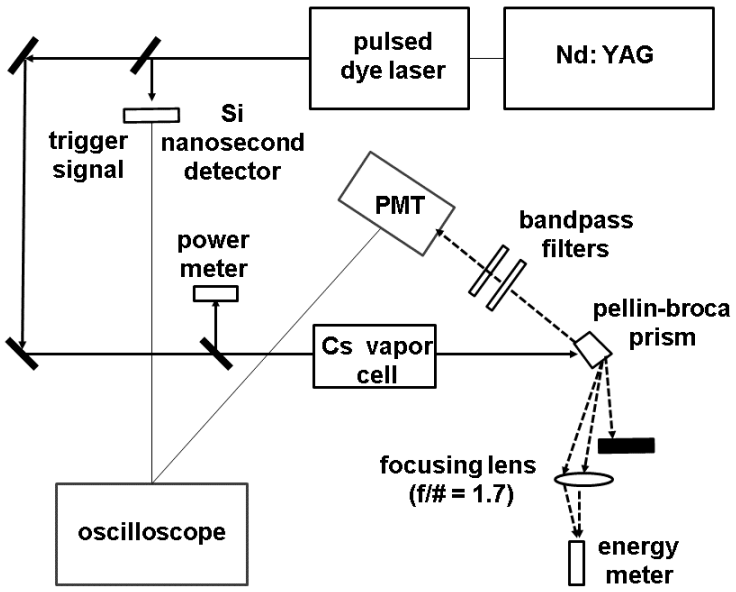

Figure 5.2: Cs vapor Amplified Spontaneous Emission (ASE) laser apparatus.

The apparatus for the two-photon ultraviolet and blue emissions study for pump transitions $6^2S_{1/2} \rightarrow 7^2D_{5/2,\,3/2}$ is shown in Figure 5.2. A frequency-doubled Quanta-Ray Pro Series pulsed Nd:YAG laser (10 Hz , $0-1$ $J/pulse$, 532 nm) is used to pump a Sirah model PRSC-D-1800 dye laser with LDS-765 dye tuned to populate the Cs $7^2D_{3/2}$ or $7^2D_{5/2}$ levels. The dye laser provides $6-10$ ns pulses in a 1 mm radius spot as the energy is tuned from 0 to 30 $mJ/pulse$ by varying the Nd:YAG flash-lamp energy. A 2.5 cm diameter by 6.5 cm long Triad technologies cesium vapor cell with Pyrex windows

was heated to 150 - 200°C. This is a low pressure cell with no buffer gases containing only cesium at the natural isotopic abundance.

The target states, Cs $7^2D_{3/2}$ and Cs $7^2D_{5/2}$, are produced by two-photon absorption of the ground state, Cs $6^2S_{1/2}$, at wavelengths near 767.8 *nm* and 767.2 *nm*, respectively. The transmitted pump and resulting stimulated beams were dispersed through a pellin-broca prism, reflected off a smooth aluminum block and measured by the C31034A photomultiplier tube using narrow bandpass filters to isolate the ultraviolet (UV), blue and red beams. A combination of 25 mm diameter narrow bandpass filters were used for 387 nm, 388 nm, 455 nm and 459 nm emissions measurements. These filters included a thorlab 700 nm short pass filter with a $10 - 15\%$ transition for UV/blue, edmund optics 452 nm /45 nm bandwidth, a thorlab 390 nm /10 nm bandwidth, and specially made bandpass filters from andover corporation (388.8 nm/1 nm bandwidth, 387.8 nm/1 nm bandwidth, 455.5 nm/3 nm bandwidth and 459.3 nm/3 nm bandwidth). Average power was measured using an RjP-735 pyroelectric energy meter with a spectral response of $0.18 - 20\ \mu$m and a minimum detectable energy of 100 nJ.

Blue and UV beams were observed as the pump laser was tuned through the two-photon absorption wavelengths. Visible images of the blue and UV beams and the transmitted far red pump laser spots recorded after the pellin-broca prism for the Cs cell are shown in Figure 5.3 and Figure 5.4 at distances of 0.5 m and 1.5 m, respectively. Images of the blue and UV beams were taken by a Canon Digital Rebel XT DSLR Camera with EF-S 18-55mm f3.5-5.6 zoom lens and 8.0-megapixel CMOS sensor and video was recorded on a Kodak EasyShare C180 10.2-megapixel digital camera for UV, blue and red beam emission analysis. The pump beam saturates the camera and the UV beams were captured via florescence from a thin white paper background.

To validate that Cs alkali atoms emits various laser emissions at different wavelengths when pumped on the two-photon Cs $6^2S_{1/2} \rightarrow 7^2D_{5/2,\ 3/2}$ transitions, a Cs heatpipe cell

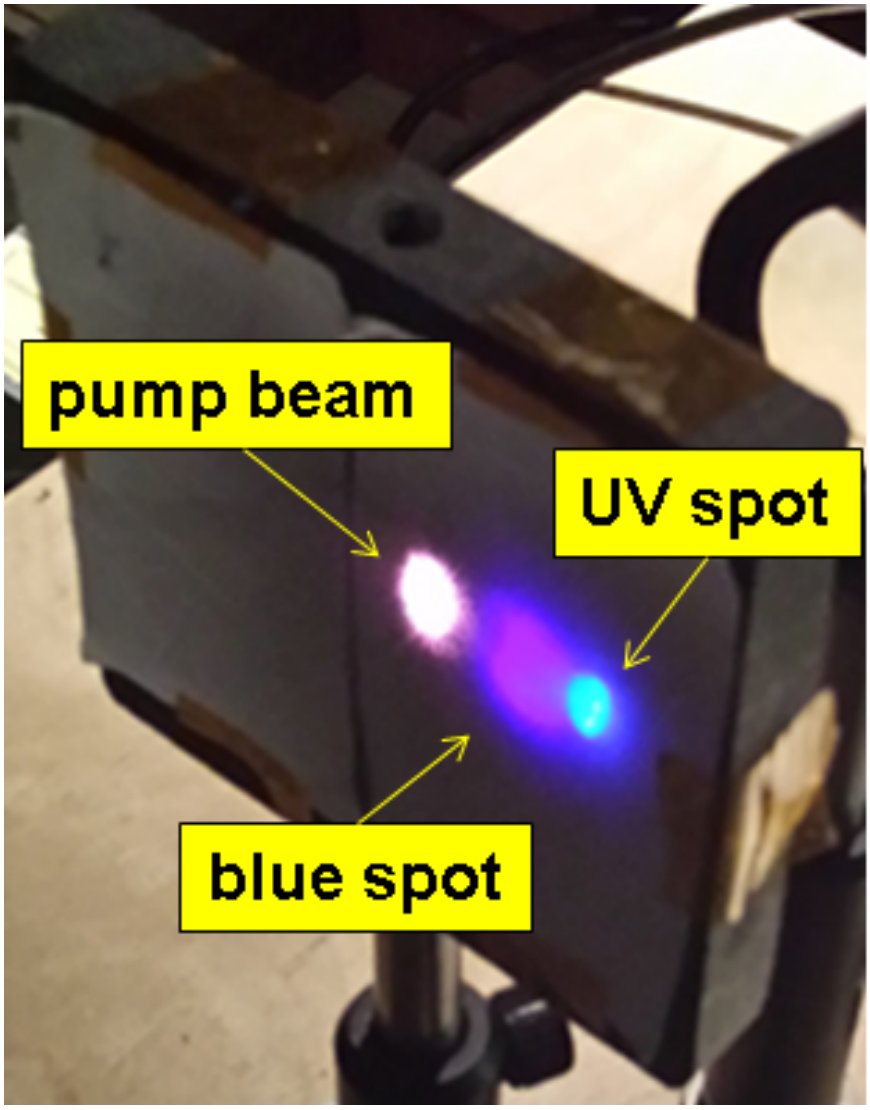

Figure 5.3: Beam emissions for the Cs cell in the forward direction at 0.5 m.

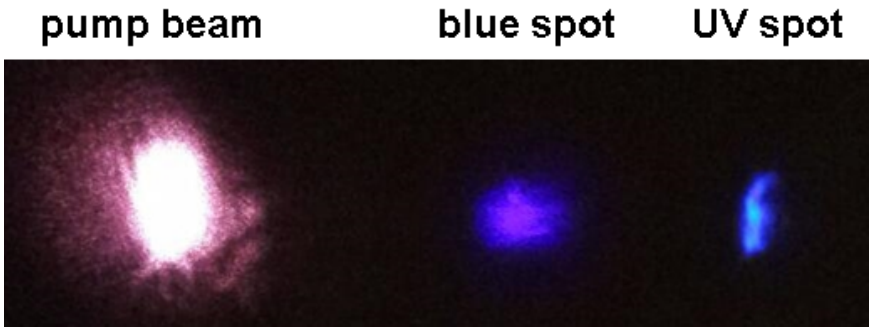

Figure 5.4: Beam emissions for the Cs cell in the forward direction at 1.5 m.

is heated to 200°C, corresponding to a Cs vapor density of $n = 1.82 \times 10^{15}$ cm^{-3}, to produce the excitation spectrum show in Figure 5.5. The Cs DPAL cell path is a 12 cm long and 2.54 cm diameter heatpipe pumped by the dye laser using LDS-765 dye at 10 mJ per pulse. The heatpipe, described in detail in reference [61], was monitored by a MKS Instruments 690A Baratron capacitance manometer to ensure emission measurements were conducted while the heatpipe contained no or minimal non-Cs vapor gases. The Cs heatpipe cell emissions were collected by SpectraPro-275 and McPherson-218 monochromators to capture emissions from UV (> 386 nm) through NIR (< 1500) nm with resolutions less than 0.1 nm, sufficient to differentiate between closely space Cs vapor emissions such as 387.6 nm and 388.9 nm $\left(8^2P_{3/2,\,1/2} \rightarrow 6^2S_{1/2}\right)$ and 697.3 nm and 698.3 nm $\left(7^2D_{5/2,\,3/2} \rightarrow 6^2P_{3/2}\right)$.

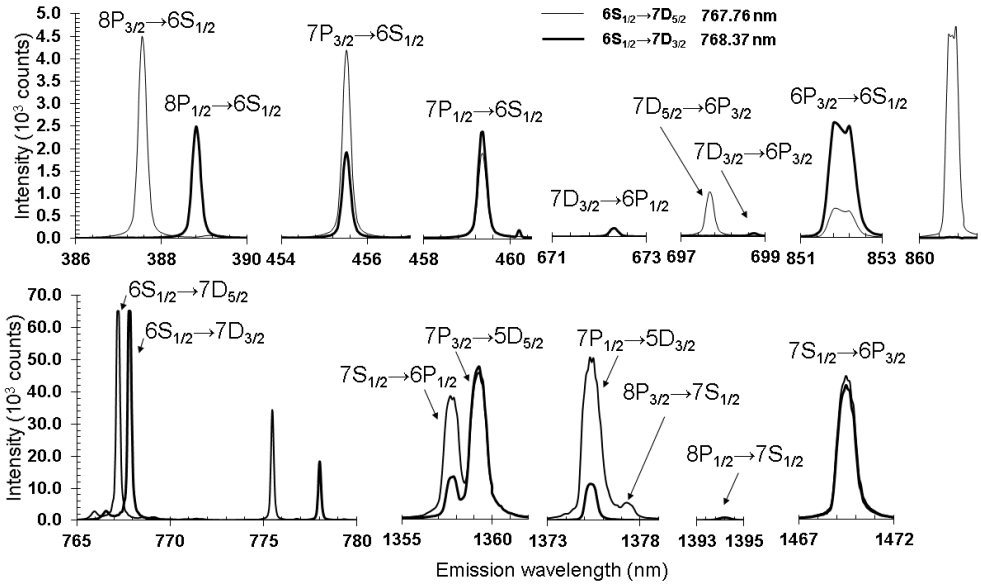

Figure 5.5: Cesium emission spectrum for $\lambda = 386$ nm to $\lambda = 1472$ nm for pulsed excitation on the two-photon Cs $6^2S_{1/2} \rightarrow 7^2D_{5/2,\,3/2}$ transitions at heatpipe cell temperature $T = 200$°C.

5.3 Results

These UV and blue Cs vapor laser emissions depicted in Figure 5.5 are consistent with previous observations for ultraviolet 387.7 nm $\left(8^2P_{3/2} \rightarrow 6^2S_{1/2}\right)$ [40], blue 455.5 nm $\left(7^2P_{3/2} \rightarrow 6^2S_{1/2}\right)$ [40, 113, 119] and blue 459.3 nm $\left(7^2P_{1/2} \rightarrow 6^2S_{1/2}\right)$ [113, 119]. The short-wave infrared emissions depicted in Figure 5.5, wavelengths between 1300 nm through 1500 nm, are consistent with measurements in reference [113]. No measurable Cs vapor laser emissions in Figure 5.5 were observed between 870 nm through 1357 nm.

Figure 5.6 shows the evolution from fluorescence emission (heatpipe temperature $<$ 75°C) for laser beam output (heatpipe temperature $>$ 100°C) for Cs emission 672.3 nm $\left(7^2D_{3/2} \rightarrow 6^2P_{1/2}\right)$. The experiment was originally performed using the equipment setup detailed in [35] which used the Cs heatpipe for determining 7^2D spin-orbit rate measurements. A frequency-doubled Quanta-Ray Pro Series pulsed Nd:YAG laser (10 Hz , 0 – 1 $J/pulse$, 532 nm) is used to pump a Sirah model PRSC-D-1800 dye laser with LDS-765 dye tuned to populate the Cs $7^2D_{3/2}$ level. The Cs DPAL cell path is a 12 cm long and 2.54 cm diameter heatpipe [61] and no buffer gas was used in this study. The target state, Cs $7^2D_{3/2}$, is produced by two-photon absorption of the ground state, Cs $6^2S_{1/2}$, at wavelength 767.8 nm. The population of the excited state is measured using the C31034A photomultiplier tube to detect the side fluorescence for temperatures at and below 75°C and lasing emissions for Cs heatpipe temperatures at or above 100°C. The exact onset of 672.3 nm lasing was not determined; however, Figure 5.6 indicates 672.3 nm lasing onset occurred between cell temperatures of T = 75°C and T = 100°C corresponding to Cs vapor densities of $n = 3.08\times10^{12}$ cm^{-3} and $n = 1.57\times10^{13}$ cm^{-3}, respectively. The rapid decrease in intensity at T = 100°C after reaching its peak compared to longer measured decay rates at T = 75°C and below, consistent with previous florescence decay profiles [35, 36], is indicative of pulsed lasing activity. The time scale of these emissions for cell temperatures $\geq T$ = 100°C approaches pulses on the order of 20 ns to 30 ns, roughly two to three times

the 10 ns pump pulse duration. Figure 5.6 also confirms previous observations made during the $7D$ spin-orbit study [35] that for heatpipe temperatures above 75°C results in longer decay rates caused by radiation being absorbed and remitted before escaping the heat-pipe. The laser dye pump pulse at the entrance window of the heatpipe was approximately 16 mJ per pulse.

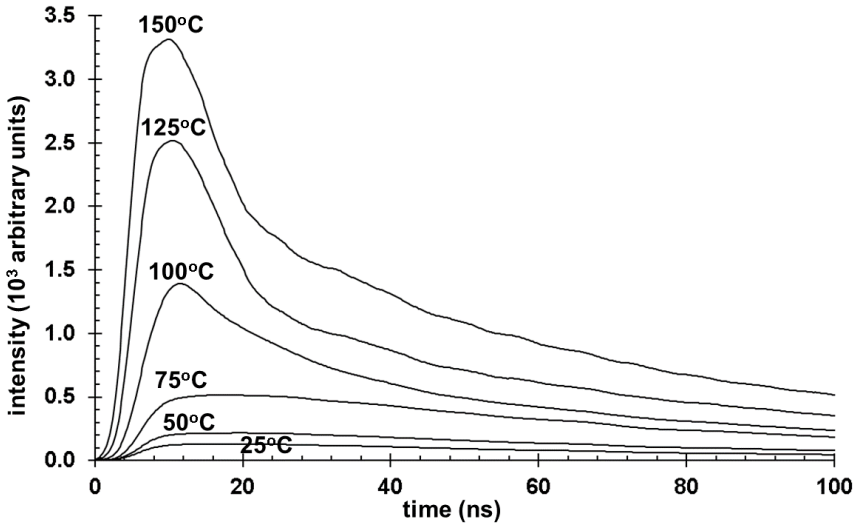

Figure 5.6: Cs 672.3 nm $\left(7^2D_{3/2} \rightarrow 6^2P_{1/2}\right)$ laser development from florescence Cs vapor at T = 25°C through laser emissions at T = 100°C through T = 150°C.

Figure 5.7 shows 672.3 nm lasing output for Cs vapor cell temperature of 150°C for pump beam energies less than 8 mJ using the equipment setup shown Figure 5.2. The target state, Cs $7^2D_{3/2}$, was produced by two-photon absorption of the ground state, Cs $6^2S_{1/2}$ at a wavelength near 767.8 nm. The lasing was detected by a C31034A photomultiplier tube using narrow bandpass filters. A Thorlabs FES0750 shortpass filter with a cutoff wavelength of 750 nm was used to minimize scattered pump light yet allow over 88% transmission for 672.3 nm emissions. A second Andover Corp 670.8 nm filter with center wavelength and 10 nm bandwidth filter was used in conjunction with the shortpass filter. The 670.8 nm filter has a 66% transmission at 672.3 nm. The scattered pump laser intensity

was measured and subtracted from the observed emission profiles by tuning off resonance, thereby minimizing the scattered light contribution to the $7^2D_{3/2} \rightarrow 6^2P_{1/2}$ transition emission. Energy measurements could not be performed for 672.3 *nm* output beams due to the minimal separation between red ASE and pump beam and associated damage risk presented to the RjP-735 pyroelectric energy meter detector. Pump energies were kept below 8 mJ per pulse due to saturation effects on the C31034A photomultiplier for pump pulse energies above this energy per pulse level. 672.3 *nm* ASE was also observed for vapor cell temperatures at 175°C and 200°C and initial indications suggest for a given pump intensity, 672.3 *nm* ASE intensity increases for higher Cs alkali density. Clearly 672.3 *nm* lasing occurs at 150°C and beam output increases with increasing pump energies. A more detailed analysis is required to determine how the Cs red beam output scales with alkali density and pump intensity and what Cs vapor density is required for the onset of red lasing.

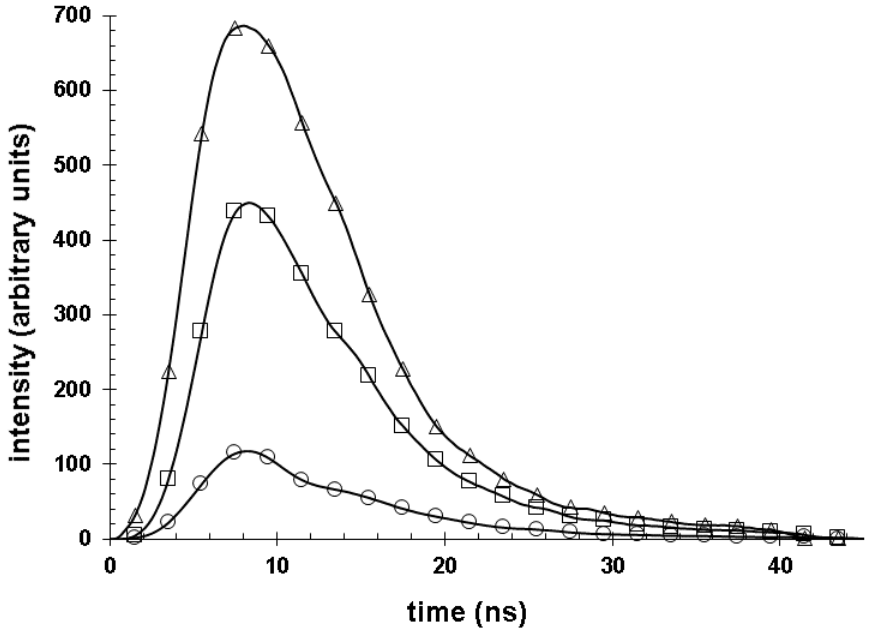

Figure 5.7: Cs 672.3 nm $\left(7^2D_{3/2} \rightarrow 6^2P_{1/2}\right)$ laser output for cell temperature T = 150°C and pump energies of ○ - 5.8 mJ, □ - 6.9 mJ, and △ - 7.6 mJ.

The dependence of the ultraviolet and blue output energies on pump energy at three temperatures for the pump transitions $6^2S_{1/2} \rightarrow 7^2D_{5/2}$ and $6^2S_{1/2} \rightarrow 7^2D_{3/2}$ are shown in Figure 5.8 and Figure 5.9, respectively. Output energies grow linearly until pump pulse energies of $6 - 8$ mJ and gradually level off through the highest pump energy used at 31 mJ. For all emission wavelengths, the energies increase with cesium vapor density. The uncertainty in the output energies represent the 95% confidence bounds for the associated lasing intensities measured by the C31034A photomultiplier tube. A functional form, first used and described in [84], was used to fit these results:

$$E = E_m \left(1 - e^{-\eta((E_p - E_{th})/E_m)}\right), \tag{5.1}$$

where

E = laser output energy per pulse.

E_p = pump dye laser energy per pulse.

E_m = bleached limit for maximum output energy.

E_{th} = threshold pump energy.

η = initial slope efficiency.

Threshold conditions were achieved for both pump transitions for pump energies of $0.5 - 3.5$ mJ as shown in Figure 5.10. Error bounds in Figure 5.10 are reported for the 95% confidence intervals for the E_{th} fit parameter.

Consistent with results reported in [84], for higher pump intensities, there are not sufficient cesium atoms in the pumped volume to process all of the incident pump photons. The population in the ground state is depleted and the pump transition becomes transparent. As the alkali density increases the maximum output energy increases linearly, as additional pump photons can be processed. The linear fits in Figure 5.11 indicates a small positive intercept, which could be interpreted as a threshold requirement or may indicate minor curvature at higher alkali densities. For both pump transitions, the trend is for the ultraviolet emissions $(387, 388)$ nm to reach higher bleached limits than the blue $(455, 459)$ nm

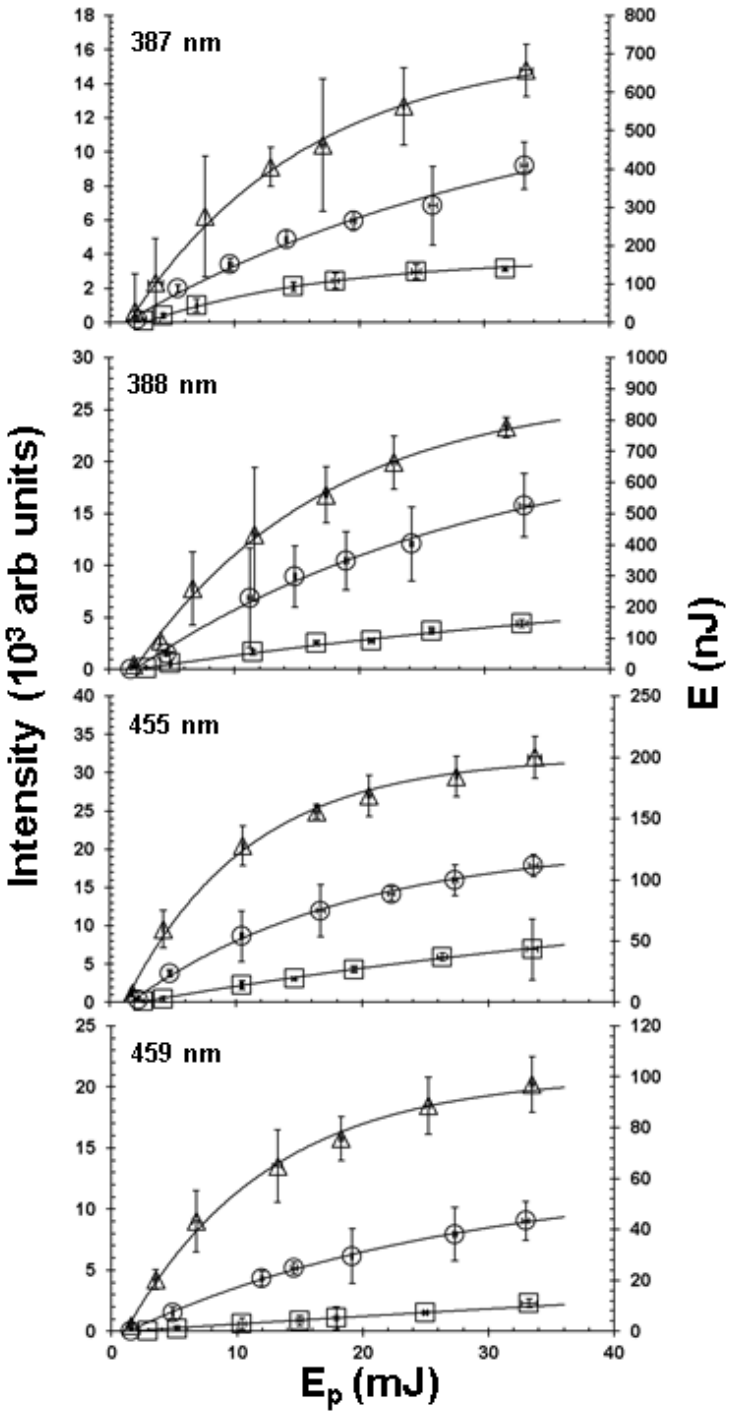

Figure 5.8: Ultraviolet (387 nm, 388 nm) and visible (455 nm, 459 nm) for pump transition $6^2S_{1/2} \rightarrow 7^2D_{5/2}$ for three temperatures and corresponding Cs vapor densities: (□) $T = 150°C$, $n = 2.26 \times 10^{14}$ cm^{-3},(○) $T = 175°C$, $n = 6.81 \times 10^{14}$ cm^{-3} and (△) $T = 200°C$, $n = 1.82 \times 10^{15}$ cm^{-3}.

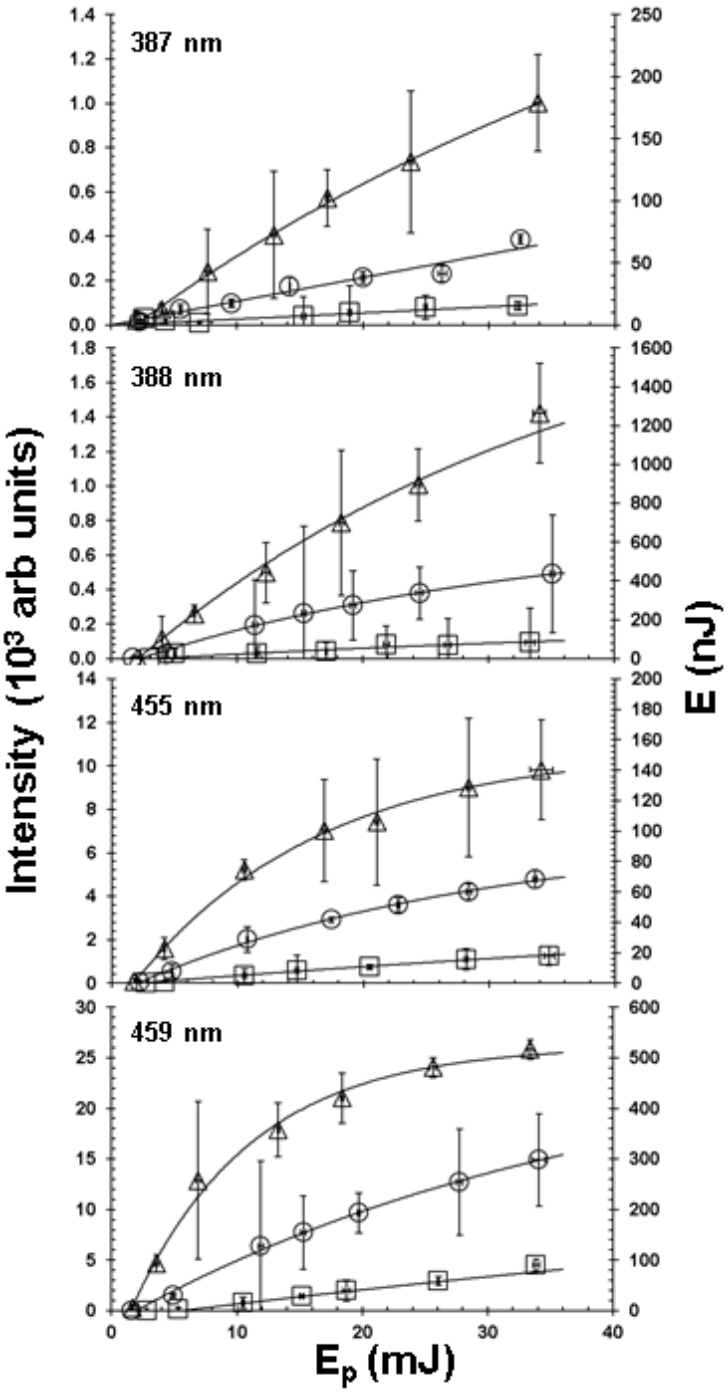

Figure 5.9: Ultraviolet (387 nm, 388 nm) and visible (455 nm, 459 nm) for pump transition $6^2S_{1/2} \rightarrow 7^2D_{3/2}$ for three temperatures and corresponding Cs vapor densities: (□) $T = 150$°C, $n = 2.26 \times 10^{14}$ cm^{-3},(○) $T = 175$°C, $n = 6.81 \times 10^{14}$ cm^{-3} and (△) $T = 200$°C, $n = 1.82 \times 10^{15}$ cm^{-3}.

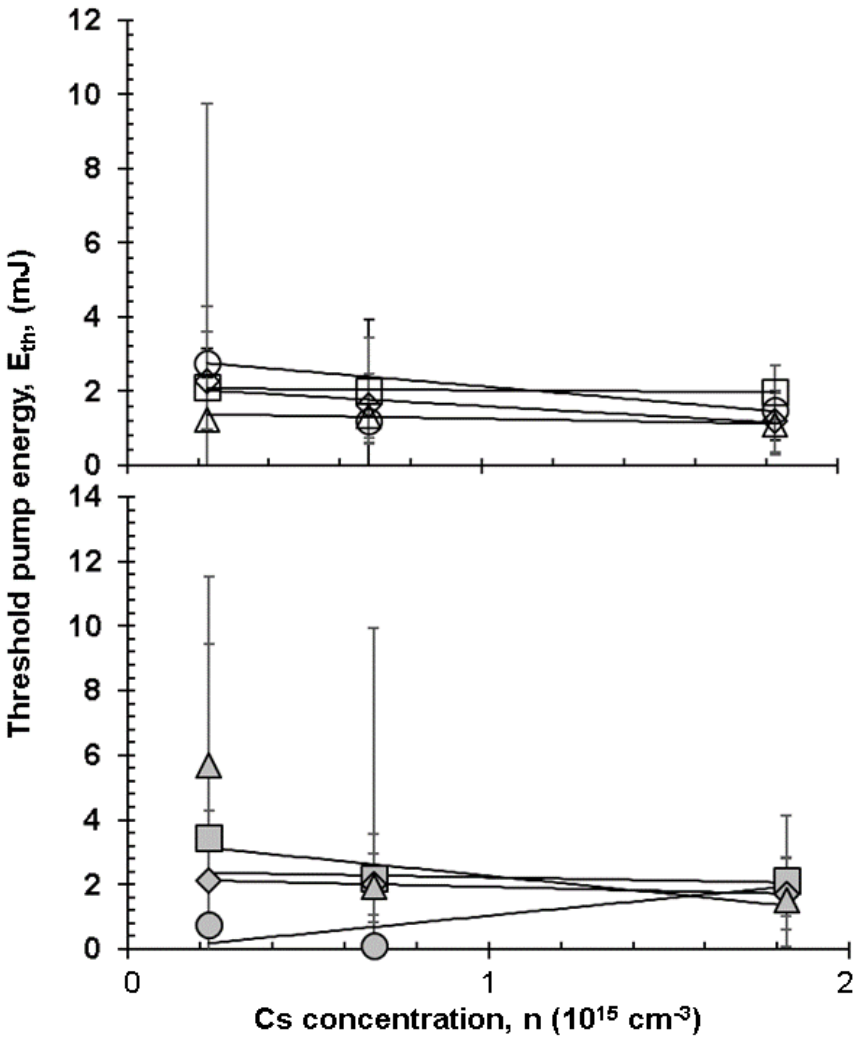

Figure 5.10: Dependence of the initial threshold energy, E_{th}, on cesium density when pumping $6^2S_{1/2} \rightarrow 7^2D_{5/2}$ (open symbols) and $6^2S_{1/2} \rightarrow 7^2D_{3/2}$ (filled symbols) for 387 nm (○, ●), 388 nm (□, ■), 455 nm (◇, ◆) and 459 nm (△, ▲) emissions.

transitions; however, results from Equation (5.1) were insufficient to adequately capture the E_m for 387 nm emission for pump transition $6^2S_{1/2} \rightarrow 7^2D_{3/2}$. Error bounds in Figure 5.11 are reported for the 95% confidence intervals for the E_m fit parameter.

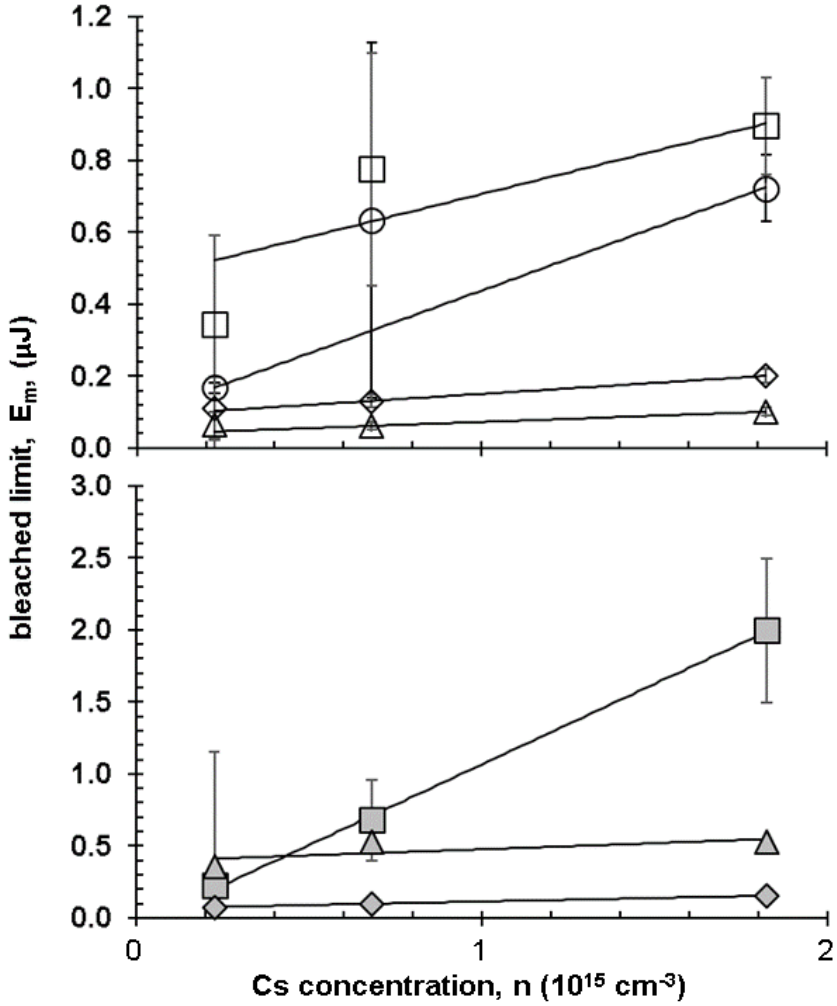

Figure 5.11: Dependence of the maximum achieved output energy, E_m, on cesium density when pumping $6^2S_{1/2} \rightarrow 7^2D_{5/2}$ (open symbols) and $6^2S_{1/2} \rightarrow 7^2D_{3/2}$ (filled symbols) for 387 nm (○, ●), 388 nm (□, ■), 455 nm (◇, ◆) and 459 nm (△, ▲) emissions.

The slope efficiencies Figure 5.12 also improve as the Cs density increases. Threshold for the ASE beams for both ultraviolet and blue occur for Cs densities at $T = 120°C$ (Cs density of $n = 4.94 \times 10^{13}$).

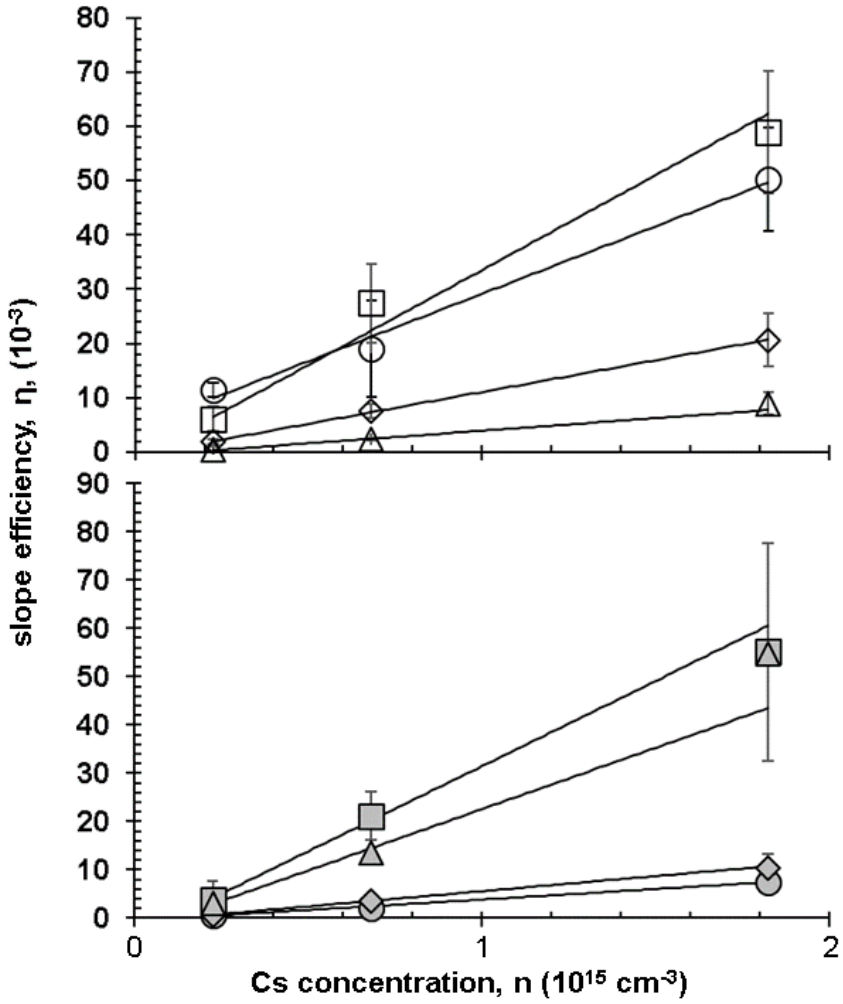

Figure 5.12: Dependence of initial slope efficiency, η, on cesium density when pumping $6^2S_{1/2} \rightarrow 7^2D_{5/2}$ (open symbols) and $6^2S_{1/2} \rightarrow 7^2D_{3/2}$ (filled symbols) for 387 nm (○, ●), 388 nm (□, ■), 455 nm (◇, ◆) and 459 nm (△, ▲) emissions.

5.4 Discussion

Both threshold and pump efficiency should depend on the absorption cross-section and two-photon absorption cross-sections are quite low. While Cs two-photon cross-sections have not been reported in the literature, calculations using a methodology outlined in [16] predict two-photon cross sections for pump transitions $6^2S_{1/2} \rightarrow 7^2D_{5/2,\,3/2}$ to be 5.96×10^{-21} cm^4/W and 2.49×10^{-21} cm^4/W, respectively. At the threshold pump energy of 3 mJ (the low end of our pump energies), the corresponding pump intensity, I, is 2×10^6 W/cm^2. To derive the two-photon saturation intensity, consider the time dependence of the excited state number density [13]:

$$\frac{dn_e}{dt} = \frac{\sigma_{eg} I_l^2}{h\nu_l} n_g - \Gamma n_e, \tag{5.2}$$

where n_e is the number density of the excited state, σ_{eg} is the two-photon cross section for the ground state, g, to the excited state, e, in cm^4/W, I_l is the laser intensity, h is planck's constant, ν_l is the laser frequency, n_g number density of the ground state and Γ is the total decay rate from the upper level in sec^{-1}. For the steady state condition, $dn_e/dt = 0$ and Equation (5.2) becomes:

$$\frac{\sigma_{eg} I_l^2}{h\nu_l} n_g - \Gamma n_e = 0, \tag{5.3}$$

which leads to

$$\frac{\sigma_{eg} I_l^2}{\Gamma h\nu_l} = \frac{n_e}{n_g}, \tag{5.4}$$

and from Equation (5.4) we define the two-photon saturation intensity as

$$I_{sat}^2 = \frac{\Gamma h\nu_l}{\sigma_{eg}}. \tag{5.5}$$

The saturation intensities, I_{sat} for pump transitions $6^2S_{1/2} \rightarrow 7^2D_{5/2,\,3/2}$ are 3.13×10^4 W/cm^2 and 4.83×10^4 W/cm^2, respectively. With saturation parameters of $S = I/I_{sat}$ of 64 and 41, the sample is strongly bleached for both pump transitions.

Figure 5.5 shows the partial Cs emission spectrum from ultraviolet ($>$ 386 nm) through NIR ($<$ 1500) nm for pump transitions $6^2S_{1/2} \rightarrow 7^2D_{5/2,\,3/2}$. This figure shows

the emission wavelength diversity at a temperature and associated Cs vapor density of 200°C and $n = 1.82 \times 10^{15}$ cm^{-3}, respectively. Our emission results, in several cases, are amplified extensions of the full Cs fluorescence from (> 360 nm) through NIR (< 1600) nm reported in [52] with the exception of our recorded emission wavelengths 775.5 nm, 778.0 nm and 861.7 nm, which have no corresponding fluorescence signatures in [52]. The full spectrum Cs vapor measurements in [52] were taken at a cell temperature of 247°C (Cs vapor density of $n = 8.94 \times 10^{15}$ cm^{-3}) after pump excitation of 455.7 nm $\left(6^2S_{1/2} \rightarrow 7^2P_{3/2}\right)$. The spectrum in [52] shows atomic transitions up to the ionization limit. The different pumping schemes and Cs cell temperatures between our measurements and the fluorescence spectrum in [52] may account for those emissions in our results not seen in [52].

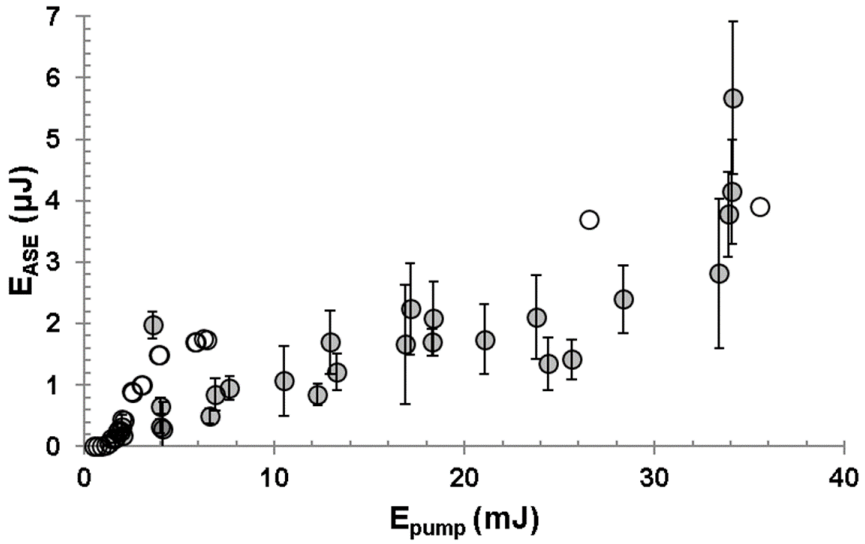

Figure 5.13: Combined ultraviolet $8^2P_{3/2,\,1/2} \rightarrow 6^2S_{1/2}$ and blue $7^2P_{3/2,\,1/2} \rightarrow 6^2S_{1/2}$ emissions (●) and blue emissions (○) from [119] after pulsed laser pumping of $6^2S_{1/2} \rightarrow 7^2D_{3/2}$ at cell temperature of 200°C (Cs vapor density, $n = 1.82 \times 10^{15}$ cm^{-3}).

Figure 5.13 shows pump power versus output emissions between our results and those measured in [119]. The error bars in Figure 5.13 depict 1-sigma deviation from

the respective mean values. Emission power measurements in [119] were taken using a Coherent LM-3 HTD power meter with power range of 10 mW to 3 W and our measurements were taken with a RjP-735 cavity pyroelectric energy probe with a minimal detectable energy of 100 nJ and a maximum energy density of 1.0 J/cm^2. Our results are comparable to those collected in [119]. Considering only the blue emissions, 455 nm and 459 nm, for 200°C in Figure 5.9, these emissions alone can not account for the power measurements in [119]. From our results, we noted that the ultraviolet and blue beam emissions for pump transitions $6^2S_{1/2} \rightarrow 7^2D_{5/2,\,3/2}$ do not significantly diverge from each other until 1 m after leaving the Triad cesium vapor cell. The spectral content of the blue beam in [119] was examined using a 0.5 m Triax monochromator but was not used to verify the ultraviolet transitions $8^2P_{3/2,\,1/2} \rightarrow 6^2S_{1/2}$ shown in this study and in [40] for similar pump pulse transitions.

Reference [40] used a GCR200, Spectra Physics, Nd:YAG laser to pump an ND6000, Continuum, dye laser to produce simultaneous ultraviolet and blue emission beams. The pump transition used was $6^2S_{1/2} \rightarrow 7^2D_{5/2}$ to produce 387.7 nm $\left(8^2P_{3/2} \rightarrow 6^2S_{1/2}\right)$ and 455.6 nm $\left(7^2P_{3/2} \rightarrow 6^2S_{1/2}\right)$ emissions [40] as seen in this study. The cell used in [40] was a quartz filled with metal Cs vapor under vacuum with a diameter of 2.5 cm and a length of 10 cm and kept at a temperature of 200°C (Cs vapor density, $n = 1.82 \times 10^{15}$ cm^{-3}). The emission beams were measured with an QE12SP-S-MT-D0, Gentec-EO energy detector and the emission spectra were recorded using a SynerJY iHR320, HORIBA spectrometer [40]. While the output pulse energy in [40] followed the same trend as this study, the pumping pulse energy (mJ) threshold and trend in [40] was two orders of magnitude smaller than reported in this study and in [119]. While we can not account for this pump pulse energy discrepancy between our results and [40], our results follow a pump pulse versus output pulse energy trend reported in [119]. Ultraviolet and blue emissions were not recorded in [40] for pump transition $6^2S_{1/2} \rightarrow 7^2D_{3/2}$ and, although, this pump transition

was used in [119], the ultraviolet emissions were not measured. This study reports the first simultaneous observations for pump transition $6^2S_{1/2} \rightarrow 7^2D_{3/2}$.

Figures 5.8 and 5.9 show UV and blue beam output emissions scale linearly with pump pulse energies below $6 - 8$ mJ and gradually level off through higher pump pulse energies. At the higher pump pulse energies, there are not sufficient Cs atoms in the pumped volume to process all the incident pump photons. The Sirah model PRSC-D-1800 dye laser's linewidth is 0.1 cm^{-1} ($\nu_{linewidth} = 3$ GHz) at 768 nm and the laser pump Doppler broadening is given by

$$\Delta\nu_D = 2\nu_{pump}\sqrt{\frac{2k_bTln(2)}{M_{Cs}c^2}} \tag{5.6}$$

where k_b is the Boltzmann constant, T is the cell temperature, M_{Cs} is the mass of the neutral cesium atom and c is the speed of light. The Cs doppler broadening frequency for cell temperatures of 150°C and 200°C are 0.99 GHz and 1.06 GHz, respectively. The pump frequency, ν_{pump}, is given by $\nu_{pump} = 2\nu_L = 3.911 \times 10^{14}$ Hz (767 nm) or 3.906×10^{14} Hz (768 nm) depending on pump transition $6^2S_{1/2} \rightarrow 7^2D_{5/2}$ or $6^2S_{1/2} \rightarrow 7^2D_{3/2}$, respectively.

The pump beam radius of 0.5 cm is consistent with previously measured in [119] using the same laser apparatus and laser dye setup for previous Cs blue beam emission characterization. The length of the Triad technologies cesium vapor cell is 6.5 cm with Pyrex windows and the cross sectional area of the pump beam is 0.78 cm^2 which gives a pump volume of 5.11 cm^3. To determine the pump energy level where the UV and blue beam output emissions no longer scale linearly, we use the following relationship where the ratio of the number of Cs atoms in the cell, for the given temperature, to the number of pump photons for a given pump intensity approaches the ratio of the Cs doppler broadening to pump laser linewidth

$$\frac{\#\text{ Cs atoms}}{\#\text{ pump photons}} \equiv \frac{\Delta\nu_D}{\nu_{linewidth}} \approx 1/3. \tag{5.7}$$

For a pump volume of 5.11 cm^3 and pump wavelength of 767 nm (3.91×10^{14} Hz), Table 5.1 contains calculated ratios for Equation (5.7). For Cs vapor cell temperature of

200°C, Table 5.1 indicates that between pulsed pump pulses of 7 – 8 mJ the UV and blue beam output emissions begin to deviate from the linear scale and begin gradually leveling off through higher pump pulse energies. For 175°C, the transition occurs for pump pulses between 2 – 3 mJ and less than 1 mJ at 150°C. This is consistent from the power scaling shown in Figures 5.8 and 5.9.

Table 5.1: Calculated ratio of number of Cs atoms to number of pulsed pump photons in 6.5 cm Pyrex Cs vapor cell.

Temperature (°C)	Cs density (cm^{-3})	# Cs atoms	Pump energy (mJ)	# Pump photons	# Cs atoms/# Pump photons
150°C	2.255×10^{14}	1.151×10^{15}	0.5	1.93×10^{15}	0.596
150°C	2.255×10^{14}	1.151×10^{15}	0.75	2.90×10^{15}	0.398
150°C	2.255×10^{14}	1.151×10^{15}	1	3.86×10^{15}	0.298
150°C	2.255×10^{14}	1.151×10^{15}	2	7.72×10^{15}	0.149
175°C	6.810×10^{14}	3.477×10^{15}	2	7.72×10^{15}	0.450
175°C	6.810×10^{14}	3.477×10^{15}	3	1.16×10^{16}	0.300
175°C	6.810×10^{14}	3.477×10^{15}	4	1.54×10^{16}	0.225
175°C	6.810×10^{14}	3.477×10^{15}	5	1.93×10^{16}	0.180
200°C	1.824×10^{15}	9.314×10^{15}	5	1.93×10^{16}	0.482
200°C	1.824×10^{15}	9.314×10^{15}	6	2.32×10^{16}	0.402
200°C	1.824×10^{15}	9.314×10^{15}	7	2.70×10^{16}	0.345
200°C	1.824×10^{15}	9.314×10^{15}	8	3.09×10^{16}	0.302

Figure 5.14 depicts the two cases for Cs UV laser emissions, $8^2P_{3/2,\,1/2} \rightarrow 6^2S_{1/2}$, after pulsed laser pumping of the $6^2S_{1/2} \rightarrow 7^2D_{3/2}$ transition, respectively. A fully-coupled mathematically model to capture the dynamics of the Cs DPAL requires measured transition probabilities between various possible cascade transition paths has yet to be

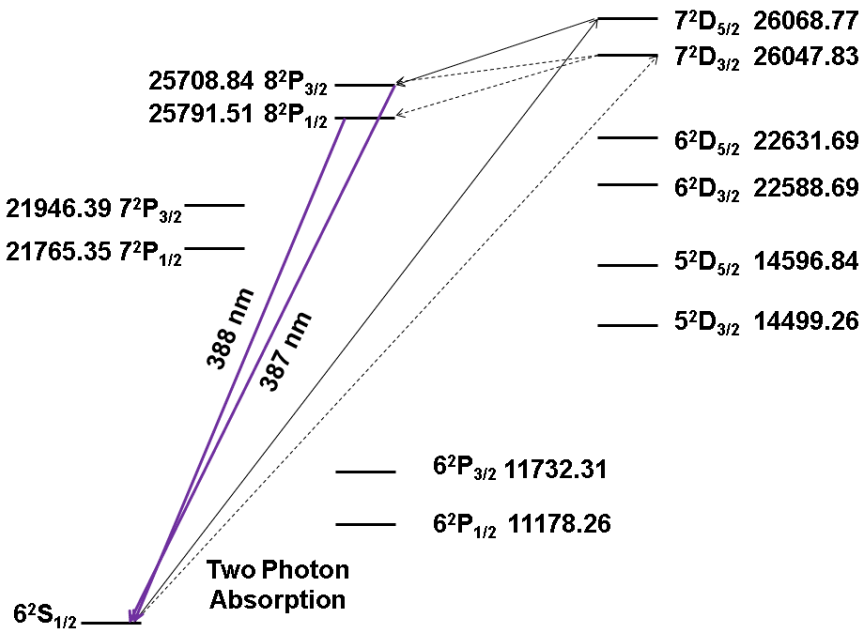

Figure 5.14: Cs ultraviolet $8^2P_{3/2,\,1/2} \rightarrow 6^2S_{1/2}$ emissions after pulsed laser pumping of $6^2S_{1/2} \rightarrow 7^2D_{3/2}$.

developed. A simplified model to investigate possible cascade lasing between the 7D, 8P and ground state, 6S, are captured in the equations below.

For the case for pulse laser pumping of $6^2S_{1/2} \rightarrow 7^2D_{5/2}$ and assuming infinite Cs-Cs mixing rate transitions for 7D and 8P fine structure states and infinite stimulated cross sections for infrared and UV transitions, the equations to simultaneously solve are:

$$\left(\frac{6}{2}\right) n_{6^2S_{1/2}} - n_{7^2D_{5/2}} = 0 \tag{5.8}$$

$$n_{7^2D_{3/2}} - \left(\frac{6}{4}\right) e^{(\theta_1)} n_{7^2D_{5/2}} = 0 \tag{5.9}$$

$$n_{7^2D_{5/2}} - \left(\frac{6}{4}\right) n_{8^2P_{3/2}} = 0 \tag{5.10}$$

$$n_{8^2P_{1/2}} - \left(\frac{4}{2}\right) e^{(\theta_2)} n_{8^2P_{3/2}} = 0 \tag{5.11}$$

$$n_{6^2S_{1/2}} + n_{7^2D_{5/2}} + n_{7^2D_{3/2}} + n_{8^2P_{3/2}} + n_{8^2P_{1/2}} = n_{Total} \tag{5.12}$$

where n is the number density for the specified energy level, $\theta_1 = \Delta_{7D}/(k_bT)$, and $\theta_2 = \Delta_{8P}/(k_bT)$. For these conditions $\Delta_{7D} = 21$ cm^{-1}, energy splitting of the $7D$ fine structure, $\Delta_{8P} = 83$ cm^{-1}, energy splitting of the $8P$ fine structure, $k_b = 0.695$ cm^{-1}/K and T are temperatures 150°C (423.15 K), 175°C (448.15 K) and 200°C (473.15 K).

Similarly for the case for pulse laser pumping of $6^2S_{1/2} \rightarrow 7^2D_{3/2}$ and assuming infinite Cs-Cs transition for 7D and 8P fine structure states, the equations to simultaneously solve are:

$$\left(\frac{4}{2}\right)n_{6^2S_{1/2}} - n_{7^2D_{3/2}} = 0 \tag{5.13}$$

$$n_{7^2D_{3/2}} - \left(\frac{6}{4}\right)e^{(\theta_1)}n_{7^2D_{5/2}} = 0 \tag{5.14}$$

$$2n_{7^2D_{3/2}} - n_{8^2P_{3/2}} - \left(\frac{4}{2}\right)n_{8^2P_{1/2}} = 0 \tag{5.15}$$

$$n_{8^2P_{1/2}} - \left(\frac{4}{2}\right)e^{(\theta_2)}n_{8^2P_{3/2}} = 0 \tag{5.16}$$

$$n_{6^2S_{1/2}} + n_{7^2D_{5/2}} + n_{7^2D_{3/2}} + n_{8^2P_{3/2}} + n_{8^2P_{1/2}} = n_{Total} \tag{5.17}$$

For cell temperatures of 150°C, 175°C and 200°C, the density of Cs atoms are 2.26×10^{14}cm^{-3}, 6.81×10^{14}cm^{-3} and 1.82×10^{15}cm^{-3}, respectively. Table 5.2 shows the resulting calculations of number density for temperatures 150°C, 175°C and 200°C for pump transitions $6^2S_{1/2} \rightarrow 7^2D_{5/2,3/2}$.

The population inversions, Δ, for the ultraviolet transitions $8^2P_{3/2} \rightarrow 6^2S_{1/2}$ and $8^2P_{1/2} \rightarrow 6^2S_{1/2}$ are given by the following equations:

$$\Delta_{8^2P_{3/2} \rightarrow 6^2S_{1/2}} = n_{8^2P_{3/2}} - \left(\frac{4}{2}\right)n_{6^2S_{1/2}} \tag{5.18}$$

$$\Delta_{8^2P_{1/2} \rightarrow 6^2S_{1/2}} = n_{8^2P_{1/2}} - \left(\frac{2}{2}\right)n_{6^2S_{1/2}} \tag{5.19}$$

Using the appropriate calculated number densities in Table 5.2 and Equations (5.18) and (5.19), Table 5.3 shows the resulting calculations for Cs UV $8^2P_{3/2,1/2} \rightarrow 6^2S_{1/2}$ population inversions for temperatures 150°C, 175°C and 200°C for pump transitions $6^2S_{1/2} \rightarrow 7^2D_{5/2,3/2}$.

Table 5.2: Calculated number density resulting from simultaneously solving Equations (5.8) - (5.12) for pump transition $6^2S_{1/2} \rightarrow 7^2D_{5/2}$ and Equations (5.13) - (5.17) for pump transition $6^2S_{1/2} \rightarrow 7^2D_{3/2}$.

		Number density (cm^{-3})		
		Alkali cell temperature		
Pump transition	Energy level	150°C	175°C	200°C
$6^2s_{1/2} \rightarrow 7^2D_{5/2}$	$6^2S_{1/2}$	1.707×10^{13}	5.130×10^{13}	1.368×10^{14}
	$7^2D_{5/2}$	5.121×10^{13}	1.539×10^{14}	4.105×10^{14}
	$7^2D_{3/2}$	7.154×10^{13}	2.158×10^{14}	5.778×10^{14}
	$8^2P_{3/2}$	3.414×10^{13}	1.026×10^{14}	2.737×10^{14}
	$8^2P_{1/2}$	5.155×10^{13}	1.574×10^{14}	4.257×10^{14}
$6^2s_{1/2} \rightarrow 7^2D_{3/2}$	$6^2S_{1/2}$	3.254×10^{13}	9.844×10^{13}	2.641×10^{14}
	$7^2D_{5/2}$	4.660×10^{13}	1.404×10^{14}	3.753×10^{14}
	$7^2D_{3/2}$	6.509×10^{13}	1.967×10^{14}	5.283×10^{14}
	$8^2P_{3/2}$	3.238×10^{13}	9.681×10^{13}	2.570×10^{14}
	$8^2P_{1/2}$	4.890×10^{13}	1.485×10^{14}	3.998×10^{14}

Table 5.3: Calculated Cs UV population inversion for pump transitions $6^2S_{1/2} \rightarrow 7^2D_{5/2,3/2}$.

		Population inversion (cm^{-3})		
		Alkali cell temperature		
Pump transition	Emission	150°C	175°C	200°C
$6^2S_{1/2} \rightarrow 7^2D_{5/2}$	$8^2P_{3/2} \rightarrow 6^2S_{1/2}$	-0.004	0	0
	$8^2P_{1/2} \rightarrow 6^2S_{1/2}$	3.448×10^{13}	1.061×10^{14}	2.889×10^{14}
$6^2S_{1/2} \rightarrow 7^2D_{3/2}$	$8^2P_{3/2} \rightarrow 6^2S_{1/2}$	-3.270×10^{13}	-1.001×10^{14}	-2.713×10^{14}
	$8^2P_{1/2} \rightarrow 6^2S_{1/2}$	1.635×10^{13}	5.004×10^{13}	1.356×10^{14}

For a two-level system, the laser intensity propagation along the laser cavity is given by [92]

$$\frac{dI}{dz} = \left[A_{21}\frac{\lambda^2}{8\pi n^2}g(v)\right]\left[N_2 - \frac{g_2}{g_1}N_1\right]I + \xi\,(chv)\,A_{21}N_2, \tag{5.20}$$

where I is the intensity in the laser beam, A_{21} is the transition probability between energy levels 2 and 1, λ is the laser wavelength, n is the index of refraction, $g(v)$ is the lineshape function, $N_{2(1)}$ is the number density for respective energy level, $g_{2(1)}$ is the degeneracy number and ξ is the fraction of spontaneous photons emitted in the direction of beam propagation in the laser cavity.

The stimulated emission cross section, $\sigma_{SE}(v)$, and population inversion, Δ, are defined as follows

$$\sigma_{SE} = A_{21}\frac{\lambda^2}{8\pi n^2}g(v) \tag{5.21}$$

$$\Delta = N_2 - \frac{g_2}{g_1}N_1 \tag{5.22}$$

and substitution into Equation (5.20) leads to

$$\frac{dI}{dz} = \sigma_{SE}(v)\Delta + \xi\,(chv)\,A_{21}N_2. \tag{5.23}$$

Initially the only source of photons is the spontaneous term $\xi A_{21}N_2$ in Equation (5.23). As the lasing process continues the intensity from stimulated emission surpasses the spontaneous term. If the spontaneous term is neglected and we assume a few seed photons of intensity, I(z=0), then Equation (5.23) can be integrated directly. The solution indicates that the laser beam intensity grows exponentially with propagation distance through the cavity as shown below

$$I(z) = I(0)e^{\sigma_{SE}(v)\Delta z}. \tag{5.24}$$

Since the laser beam power is the intensity divided by the beams cross sectional area and the calculated stimulated cross section areas for the Cs UV transitions are within 6% difference over the temperature range for this study, the ratio of intensities should scale similarly

with similar ratios for the population inversions. For $8^2P_{1/2} \rightarrow 6^2S_{1/2}$ the calculated cross sections are 5.15×10^{-15} cm^2 for 150°C and 4.88×10^{-15} cm^2 for 200°C and for $8^2P_{3/2} \rightarrow 6^2S_{1/2}$, the cross sections are 2.20×10^{-14} cm^2 for 150°C and 2.08×10^{-14} cm^2 for 200°C. Given the small percent difference in the stimulated cross section calculations from 150°C to 200°C, the measured power should scale in proportion to the population inversions depicted in Table 5.3 for cascade lasing.

For both pump transitions $6^2S_{1/2} \rightarrow 7^2D_{3/2,5/2}$, Table 5.3 shows 388 nm $\left(8^2P_{1/2} \rightarrow 6^2S_{1/2}\right)$ population inversion (PI) scales as 1.0, 3.0 and 8.3 for ratios $(150°C/150°C)_{PI}$, $(175°C/150°C)_{PI}$, and $(200°C/150°C)_{PI}$, respectively. Table 5.2 contains the ratios of 388 nm power outputs using the form fit Equation (5.1) shown in Figures 5.8 and 5.9 at the 7 mJ pulsed pump energy.

Table 5.4: Cs UV (388 nm) emission energies and ratios for 150°C, 175°C and 200°C.

	388 nm pulse energy (nJ)					
	Alkali cell temperature			Ratio		
Pump transition	150°C	175°C	200°C	$(150°C/150°C)_E$	$(175°C/150°C)_E$	$(200°C/150°C)_E$
$6^2S_{1/2} \rightarrow 7^2D_{5/2}$	28	125	252	1	4	9
$6^2S_{1/2} \rightarrow 7^2D_{3/2}$	13	94	252	1	7	20

The ratios show in Table 5.4 are consistent for pump pulse energies from 6 mJ through 8 mJ. The ratios (1, 4 and 9) for pump pulse transition $6^2S_{1/2} \rightarrow 7^2D_{5/2}$ are consistent with the calculated ratios (1, 3 and 8) for the population inversions for the same pump pulse transition in Table 5.3. This comparison is an indication that cascade lasing may play a major role in the Cs UV lasing process. For $6^2S_{1/2} \rightarrow 7^2D_{5/2}$, the energy ratios are doubled those population inversion ratios using the values recorded in Table 5.3 for $(175°C/150°C)_{PI}$ and $(200°C/150°C)_{PI}$.

While the analysis that led up to the population inversions listed in Table 5.3 supports cascade lasing for the 388 nm emission for pump transition $6^2S_{1/2} \rightarrow 7^2D_{5/2}$, the analysis does not adequately support cascade lasing for 388 nm emission for pump pulse $6^2S_{1/2} \rightarrow 7^2D_{3/2}$ nor does the analysis' results support the observed 387 nm $\left(8^2P_{3/2} \rightarrow 6^2S_{1/2}\right)$ emissions for both pump transitions $6^2S_{1/2} \rightarrow 7^2D_{5/2,3/2}$.

The first possible explanation to account for the differences between the results of the UV population inversion analysis and observed UV output emissions is the various transitions that occur from the $7D$ states back to the Cs ground state $6S$. Tables 5.5 and 5.6 show the cascading transitions for pump pulse transitions $6^2S_{1/2} \rightarrow 7^2D_{5/2,\ 3/2}$, respectively.

The transitions are consistent with the Cs emission spectrum in Figure 5.5, either observed transitions or cascading transitions leading up to these emissions. These transitions are arranged in descending order of the measured or calculated transition probabilities. Derived transition probabilities used the Weakest Bound Electron Potential Model (WBEPM) theory outlined in [25, 26, 143] and using the radial dipole integral for hydrogenic atoms described in [32]. The WPEPM transition probability equations derivation and subsequent cross section calculations are outlined in Appendix A.

Tables 5.5 and 5.6 reflect over 18+ transitions that may lase and bottleneck and possibly re-lase before undergoing the UV output emissions. A fully-coupled kinetics model needs to be developed to capture all these transitions and would be more complicated that the analysis used to calculate the population inversions in Table 5.3 for cascade lasing. A high-level Cs kinetics model is described in section 6.3.2 and may capture the cascading events given correct spin-orbit cross sections in the P and D states and measured and calculated transition probabilities for the various inter-multiplet transitions outlined in Tables 5.5 and 5.6 and other transitions not captured in these tables.

The second possible explanation to account for the differences between the results of the UV population inversion analysis and observed UV output emissions is Equations 5.8

Table 5.5: Transition wavelengths, probabilities and cross sections for several dipole allowed transitions of cesium at 200°C for pump transition $6^2S_{1/2} \rightarrow 7^2D_{5/2}$.

Transition	Wavelength λ (nm)	Transition prob. A (10^6 s^{-1})	Cross section σ (cm^2)	Transition prob. reference
$7^2D_{5/2} \rightarrow 8^2P_{3/2}$	36066.6	0.052	2.25×10^{-9}	*
$8^2P_{3/2} \rightarrow 8^2S_{1/2}$	6782.6	0.956	2.75×10^{-10}	*
$8^2S_{1/2} \rightarrow 7^2P_{3/2}$	4218.1	2.620	1.81×10^{-10}	*
$6^2D_{5/2} \rightarrow 7^2P_{3/2}$	14592.4	0.063	1.81×10^{-10}	*
$7^2P_{1/2} \rightarrow 7^2S_{1/2}$	3096.1	3.520	9.64×10^{-11}	*
$7^2P_{3/2} \rightarrow 7^2S_{1/2}$	2931.8	4.050	9.42×10^{-11}	*
$8^2S_{1/2} \rightarrow 7^2P_{1/2}$	3918.8	1.380	7.66×10^{-11}	*
$7^2D_{5/2} \rightarrow 7^2P_{3/2}$	2425.8	2.768	3.65×10^{-11}	*
$7^2S_{1/2} \rightarrow 6^2P_{3/2}$	1469.9	11.400	3.34×10^{-11}	*
$8^2P_{3/2} \rightarrow 6^2D_{5/2}$	3164.7	0.746	2.18×10^{-11}	*
$6^2P_{3/2} \rightarrow 6^2S_{1/2}$	852.3	32.790	1.87×10^{-11}	[105]
$7^2S_{1/2} \rightarrow 6^2P_{1/2}$	1359.2	6.230	1.44×10^{-11}	*
$7^2P_{1/2} \rightarrow 5^2D_{3/2}$	1376.3	1.590	3.82×10^{-12}	*
$7^2D_{5/2} \rightarrow 6^2P_{3/2}$	697.5	8.543	2.67×10^{-12}	*
$7^2P_{3/2} \rightarrow 5^2D_{5/2}$	1360.6	1.100	2.56×10^{-12}	*
$8^2P_{3/2} \rightarrow 7^2S_{1/2}$	1378.2	0.565	1.36×10^{-12}	*
$7^2P_{3/2} \rightarrow 6^2S_{1/2}$	455.7	1.840	1.61×10^{-13}	[126]
$7^2P_{1/2} \rightarrow 6^2S_{1/2}$	459.4	0.793	7.10×10^{-14}	[126]
$8^2P_{3/2} \rightarrow 6^2S_{1/2}$	387.7	0.386	2.08×10^{-14}	[75]
$8^2P_{1/2} \rightarrow 6^2S_{1/2}$	389.0	0.090	4.88×10^{-15}	[75]

Table 5.6: Transition wavelengths, probabilities and cross sections for several dipole allowed transitions of cesium at 200°C for pump transition $6^2S_{1/2} \rightarrow 7^2D_{3/2}$.

Transition	Wavelength λ (nm)	Transition prob. A (10^6 s^{-1})	Cross section σ (cm^2)	Transition prob. reference
$7^2D_{3/2} \rightarrow 8^2P_{1/2}$	29498.6	0.058	1.38×10^{-9}	*
$7^2D_{3/2} \rightarrow 8^2P_{3/2}$	39012.8	0.010	5.44×10^{-10}	*
$8^2P_{1/2} \rightarrow 8^2S_{1/2}$	7185.5	0.835	2.86×10^{-10}	*
$8^2P_{3/2} \rightarrow 8^2S_{1/2}$	6782.6	0.956	2.75×10^{-10}	*
$8^2S_{1/2} \rightarrow 7^2P_{3/2}$	4218.1	2.620	1.81×10^{-10}	*
$7^2P_{1/2} \rightarrow 7^2S_{1/2}$	3096.1	3.520	9.64×10^{-11}	*
$7^2P_{3/2} \rightarrow 7^2S_{1/2}$	2931.8	4.050	9.42×10^{-11}	*
$8^2S_{1/2} \rightarrow 7^2P_{1/2}$	3918.8	1.380	7.66×10^{-11}	*
$7^2S_{1/2} \rightarrow 6^2P_{3/2}$	1469.9	11.400	3.34×10^{-11}	*
$6^2D_{3/2} \rightarrow 7^2P_{3/2}$	15566.0	0.009	2.99×10^{-11}	*
$8^2P_{1/2} \rightarrow 6^2D_{3/2}$	3205.1	0.733	2.23×10^{-11}	*
$8^2P_{3/2} \rightarrow 6^2D_{5/2}$	3164.7	0.746	2.18×10^{-11}	*
$6^2P_{3/2} \rightarrow 6^2S_{1/2}$	852.3	32.790	1.87×10^{-11}	[105]
$7^2D_{3/2} \rightarrow 7^2P_{1/2}$	2335.1	1.594	1.87×10^{-11}	*
$7^2S_{1/2} \rightarrow 6^2P_{1/2}$	1359.2	6.230	1.44×10^{-11}	*
$7^2P_{1/2} \rightarrow 5^2D_{3/2}$	1376.3	1.590	3.82×10^{-12}	*
$7^2P_{3/2} \rightarrow 5^2D_{5/2}$	1360.6	1.100	2.56×10^{-12}	*
$8^2P_{3/2} \rightarrow 6^2D_{3/2}$	3122.4	0.086	2.42×10^{-12}	*
$7^2D_{3/2} \rightarrow 6^2P_{1/2}$	672.5	5.840	1.64×10^{-12}	*
$8^2P_{1/2} \rightarrow 7^2S_{1/2}$	1394.1	0.364	9.10×10^{-13}	*
$7^2D_{3/2} \rightarrow 6^2P_{3/2}$	698.5	2.008	6.31×10^{-13}	*
$7^2P_{3/2} \rightarrow 6^2S_{1/2}$	455.7	1.840	1.61×10^{-13}	[126]
$7^2P_{1/2} \rightarrow 6^2S_{1/2}$	459.4	0.793	7.10×10^{-14}	[126]
$8^2P_{1/2} \rightarrow 6^2S_{1/2}$	389.0	0.090	4.88×10^{-15}	[75]

through 5.12 and Equations 5.13 through 5.17 do not include non-linear effects. Previous studies have offered four wave mixing, a third order non-linear event, as the mechanism responsible for the blue light generation in Cs blue emissions [119], Cs blue and UV emissions [40] and Rb blue emission [3]. Recently, [1] offered population inversion and four wave mixing as possible mechanisms for generating Rb blue emissions. The kinetics model mentioned previously would be key to explore differences in the modeled Cs blue and UV emissions and observations by considering cascade lasing only. Only after these differences are analyzed, incorporating four wave maxing to model any differences will help understand whether or not these effects are cascade population inversion alone, four wave mixing alone or a combination of these two processes.

A third possible explanation to account for the differences is investigating the role of photo-ionization in a Cs DPAL laser as described in previous studies [62, 86]. At 200°C, the Cs density is 1.82×10^{15} cm^{-3}. For the Pyrex cell used in this experiment, the length of the cylinder is $L_{cell} = 6.5$ cm with a pump beam cross sectional area of $A_{pump} = 0.79$ cm^2. The number of Cs atoms contained in the pump beam column is

$$\begin{aligned} \#\text{Cs atoms} &= n_0 L_{cell} A_{pump} \\ &= 1.82 \times 10^{15}\ \text{cm}^{-3} \times 6.5\ \text{cm} \times 0.79\text{cm}^2 \\ &= 9.31 \times 10^{15}\ \text{Cs atoms} \end{aligned} \tag{5.25}$$

It takes three photons at $\nu_{pump} = 3.91 \times 10^{14}$ Hz to ionize a single Cs atom. The total energy required to ionize the column is

$$3h\nu_{pump} \times 9.31 \times 10^{15}\ \text{Cs atoms} = 7.24\ \text{mJ} \tag{5.26}$$

The 7.24 mJ is on order of the pump energy used to excite the Cs atoms in this experiment. If any of the Cs atoms are excited above the Cs ionization limit, Cs ions and electrons recombine to populate Rydberg levels above the Cs $7D$ state. Energy levels at or below $7D$ are re-populated by radiative relaxation from the Rydberg states. This is a possible

explanation for the observed UV emissions at 387 nm but not predicted by the population inversion analysis in Table 5.3. Last, it is possible that all three of these processes, cascade lasing, four wave mixing and photo-ionization are occurring simultaneously in the UV and blue emissions.

5.5 Conclusions

Stimulated emission on the ultraviolet and blue transitions in Cs has been achieved by pumping via two-photon absorption from the ground state to the 7^2D states. The performance of the optically-pumped cesium vapor laser operating in ultraviolet and blue has been extended to 650 nJ/pulse for 387 nm, 1.3 μJ/pulse for 388 nm, 200 nJ/pulse for 455 nm and 500 nJ/pulse for 459 nm. Emission performance improves dramatically as the cesium vapor density is increased. No scaling limitations associated with energy pooling or ionization kinetics have been observed. Potential applications for this new laser system include underwater communications and infrared countermeasures such as blinding heat seeking missiles.

VI. Conclusions

6.1 Work Summary

This work measured, for the first time, the spin-orbit (SO) cross section for the Cs 7^2D states using buffer gases He and Ar. This study also confirmed previous SO mixing rates and cross sections for Cs 8^2D states and put both 7^2D and 8^2D SO measurements in terms of adiabaticity theory. The final portion of this work was to characterize the Cs UV and visible emissions resulting from the pump transitions $6^2S_{1/2} \rightarrow 7^2D5/2, 3/2$. Specific results from these three studies are listed below.

First, pulsed excitation on the two-photon Cs $6^2S_{1/2} \rightarrow 7^2D_{3/2,5/2}$ transition results in time-resolved fluorescence at 697 *nm* and 672 *nm*. The rates for fine structure mixing between the $7^2D_{3/2,5/2}$ states have been measured for helium and argon rare gas collision partners. The mixing rates are very fast, $1.26 \pm 0.05 \times 10^{-9}$ $cm^3/(atom\ sec)$ for He and $1.52 \pm 0.05 \times 10^{-10}$ $cm^3/(atom\ sec)$ for Ar, driven by the small energy splitting and large radial distribution for the valence electron. The quenching rates are considerably slower, $6.84 \pm 0.09 \times 10^{-11}$ $cm^3/(atom\ sec)$ and $2.65 \pm 0.04 \times 10^{-11}$ $cm^3/(atom\ sec)$ for He and Ar, respectively. The current results are placed in context with similar rates for other alkali-rare gas collision pairs using adiabaticity arguments.

Second, pulsed excitation on the two-photon Cs $6\,^2S_{1/2} \rightarrow 8\,^2D_{3/2,5/2}$ transition results in time-resolved fluorescence at 601 *nm*. The rates for fine structure mixing between the $8\,^2D_{3/2,5/2}$ states have been measured for helium and argon rare gas collision partners. The mixing rates are very fast, $2.6 \pm 0.2 \times 10^{-9}$ $cm^3/(atom\ s)$ for He and $5.2 \pm 0.4 \times 10^{-10}$ $cm^3/(atom\ s)$ for Ar, about 2-3 times faster than for the Cs $7\,^2D_{5/2} \rightleftharpoons 7\,^2D_{3/2}$ relaxation. The quenching rates are also rapid, $1.07 \pm 0.04 \times 10^{-10}$ $cm^3/(atom\ s)$ and $9.5 \pm 0.7 \times 10^{-11}$ $cm^3/(atom\ s)$ for He and Ar, respectively. The rapid fine structure rates are explained by the highly impulsive nature of the collisions and the large average distance of

the valence electron from the nucleus. Quenching rates (intra-multiplet transfer) are likely enhanced by the closely spaced, $9\,^2P$ levels.

Third, stimulated emission on the ultraviolet and blue transitions in Cs has been achieved by pumping via two-photon absorption for the pump transition $6^2S_{1/2} \rightarrow 7^2D_{5/2,3/2}$. The emission performance of the optically pumped cesium vapor laser operating in ultraviolet and blue has been extended to 650 nJ/pulse for 387 nm, 1.3 μJ/pulse for 388 nm, 200 nJ/pulse for 455 nm and 500 nJ/pulse for 459 nm. Emission performance improves dramatically as the cesium vapor density is increased and no scaling limitations associated with energy pooling or ionization kinetics have been observed.

6.2 DPAL Impact

Major advancement for kilowatt-class lasers have been achieved since Krupke proposed diode-pumped alkali lasers as a potential kilo-watt class laser candidate [70]. While major advancements have been made in developing kilo-watt class lasers for a variety of defense platforms [58], decreasing the size, weight and power requirements for kilo-watt class lasers continues to be a challenge for future 6th generation fighter aircraft. High laser power and wavelength diversity described in [23, 56, 129] are key for developing laser based countermeasures for defeating future surface-to-air and air-to-air missiles.

While this study demonstrated laser output in the ultraviolet and visible spectrums, work remains in characterizing the wavelength diversity in the short-, mid- and long-wave alkali emission wavelengths. While the HEL community continues to diode-pumped alkali lasers from the 10s to 100s kilo-watt range, DPALs just might become a strong candidate to match or surpass previous high energy lasers such as the the chemical oxygen iodine laser (COIL) used in the Airborne Laser program. The possibility for a DPAL to emit laser output from the ultraviolet to long-wave with a possibility to reach average powers of 10s of watts at these diverse wavelengths make it a suitable laser candidate to address future threats [23, 129].

6.3 Recommendation for future work

6.3.1 Deleterious Processes in the Cesium DPAL Cell.

Deleterious processes, due to complex interactions in a DPAL gain cell, have been simulated using an advanced computational fluid dynamics model and, as an example, observed in the lab by Oliker et al. [89] and Zhdanov et al. [142], respectively. Initial motivation for investigating these processes started with recent ionization studies such as those performed by Knize et al.[62] and Ge et al. [43]. Because alkali metals have the lowest ionization energy than any other element groups on the periodic table, these studies investigated the impact of photoionization on Rb and Cs alkali laser performance. Further study is required to determine the extent of ionization as a loss mechanism to DPALs neutral alkali atoms in the gain cell.

Oliker et al. [89] lists several key deleterious processes that may impact DPAL kinetics. These processes include: dissociative recombination, multi-photon ionization, alkali-hydrocarbon reaction and electron impact ionization, alkali number density decrease in high temperature regions, convective flow, pressure broadening and shifting of the absorption lineshape including hyperfine structure, radiative decay, quenching, energy pooling, off-resonant absorption, Penning ionization, photoionization, radiative recombination, three-body recombination due to free electron and buffer gas collisions, ambipolar diffusion, and thermal aberration. Its possible that one or several of these deleterious processes may be impacting our experiments.

Further data collections and analysis of data already collected will be necessary to explore any potential deleterious effects mentioned above that may be impacting our results. A first principle model containing the rate equations and ionization rates should also be included in this analysis to explore the underlying kinetics of similar measurements. A thorough review of the journal literature reveals no study such as the one proposed here has been performed.

6.3.2 *Full kinetic theory model to explain UV and blue laser emissions.*

Despite the success of observing and characterizing blue and UV beams for Cs transitions $6^2S_{1/2} \rightarrow 7^2D_{5/2,3/2}$ and $6^2S_{1/2} \rightarrow 8^2D_{5/2,3/2}$, there remains significant work on understanding the full kinetics involved on the two-photon absorption blue and UV beams. Models to understand portions of the kinetics involved in the blue and UV beam have been developed and used to explain specific transition events for blue and UV fluorescence and beams [20, 22, 28, 31, 35, 40, 52, 119]; however, a full scale analytical model of the kinetic two-photon absorption and subsequent blue and UV beam mechanisms are required to evaluate the scaling and the efficiency of this system. Additionally the Cs two-photon absorption cross sections for $6^2S_{1/2} \rightarrow 7^2D_{5/2,3/2}$ and $6^2S_{1/2} \rightarrow 8^2D_{5/2,3/2}$ must be measured and model development of production mechanism dependence when a pressure broadening gas is added to this particular DPAL class system. Following the kinetic study, an attempt should be made to produce a true laser in both the blue and UV simultaneously for both pulsed and cw systems. Once a kinetic study and model is created for replicating the blue and UV beams, an extensive study should begin on understanding the role that cascade lasing and whether or not 4-wave mixing plays occurs simultaneously in generating blue and UV ASE [2, 3, 40, 49, 87, 117].

One such modeling scheme, depicted in Figure 6.1, is a seven-level model that includes photo-ionization, recombination, and cascade stimulated emission from either Cs $7^2D_{5/2,3/2}$ energy level back to the ground level $6^2S_{1/2}$. The first four levels (blue lines) depict the two-photon pumping from $6^2S_{1/2} \rightarrow 7^2D_{5/2,3/2}$ and cascade lasing from level 4 eventually back to the ground state $6^2S_{1/2}$ at level 1. The black lines are the decay rates between the respective levels and the purple double arrow line between levels 3 and 4 is the is the spin-orbit rate. In Figure 6.1, the spin-orbit rate is shown for $7^2D_{3/2} \rightleftharpoons 7^2D_{5/2}$.

This model incorporates photo-ionization from the $7^2D_{5/2,3/2}$ levels. It takes three photons at 3.91×10^{14} Hz to ionize a single Cs atom. This frequency is equivalent to

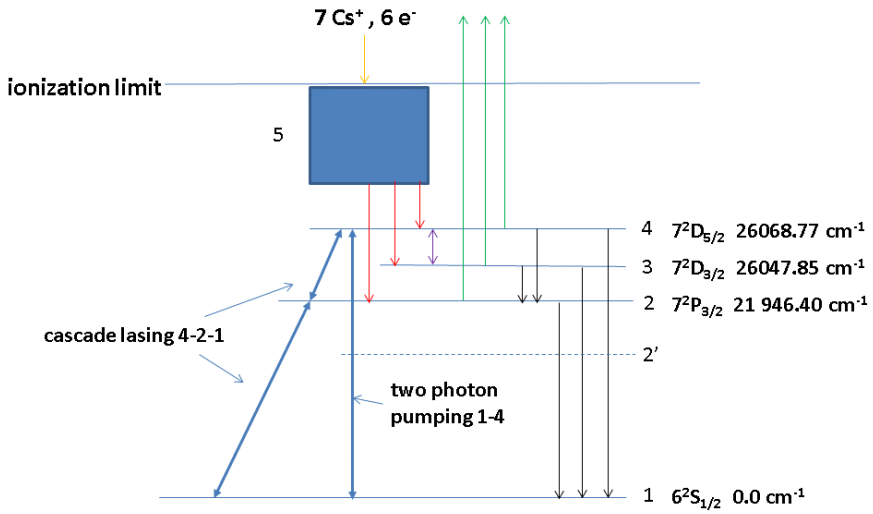

Figure 6.1: Schematic seven level energy diagram with two-photon pumping and cascade lasing.

the pump wavelength, 767.263 nm, required to pump Cs atoms via two-photons from the ground state to $7^2D_{5/2,3/2}$. The ionization limit for Cs atoms is 31423.9 cm^{-1} and the three photon energy is 39126.2 cm^{-1}. Levels 7 and 6 (green lines) contain the Cs^+ and e^- formed by photo-ionization respectively from levels 3 and 4. Cs^+ and e^- loss is by three body recombination that produces population in level 5 (orange line). Level 5 Contains all Rydberg levels above the two-photon pumped 7^2D levels up to the ionization limit. Levels 3 and 4 are re-populated by radiative relaxation from level 5 (red lines).

Figure 6.1 is a high-level depiction of a fully coupled model that includes photo-ionization, recombination, and cascade stimulated emission; however, what is not captured are the spin-orbit rates between the $8 - 6^2P_{3/2,1/2}$ and $6 - 5^2D_{5/2,3/2}$ states and the many allowed transitions between the various D, P and S states back to the ground state. Many of these possible transitions to include measured and calculated transition probabilities and cross section were shown in tables 5.5 and 5.6.

Appendix: Electric Dipole Line Strength Calculation

The electric dipole line strength for transitions between two excited levels is given by

$$\begin{aligned}\sqrt{DLS} &= (-1)^{2l+j'+3/2}\sqrt{(2j+1)(2j'+1)(2l+1)(2l'+1)} \\ &\times \begin{pmatrix} l & s & j \\ j' & 1 & l' \end{pmatrix}\begin{pmatrix} l & 1 & l' \\ 0 & 0 & 0 \end{pmatrix} \\ &\times \int_0^\infty r^3 R_{n_i l_i}(r) R_{n_f l_f}(r)\, dr\end{aligned} \tag{A.1}$$

where

s = spin quantum number

l, l' = orbital angular momentum quantum number for intial, final states

j, j' = total angular momentum quantum number for intial, final states

$\begin{pmatrix} l & s & j \\ j' & 1 & l' \end{pmatrix}$ = Racah coefficient or Wigners 6-j symbol

$\begin{pmatrix} l & 1 & l' \\ 0 & 0 & 0 \end{pmatrix}$ = Wigner 3-j symbol

$\int_0^\infty r^3 R_{n_i l_i}(r) R_{n_f l_f}(r)\, dr$ = radial transition integral

According to the WBEPM theory, electronic radial wave functions, $R_{n_i l_i}(r)$ and $R_{n_f l_f}(r)$, are presented as a function of Laguerre polynomial. These functions are represented as

$$\begin{aligned}R_{nl}(r) &= \left(\frac{2Z^*}{n^*}\right)^{l^*+3/2}\left[\frac{2n^*}{(n-l-1)!}\Gamma(n^*+l^*+1)\right]^{-1/2} \\ &\times \exp\left(-\frac{Z^* r}{n^*}\right) r^{l^*} L_{n-l-1}^{2l^*+1}\left(\frac{2Z^* r}{n^*}\right)\end{aligned} \tag{A.2}$$

where

n = principal quantum number

l = orbital angular momentum quantum number

Z^* = effective nuclear charge

$n^* = n + d \equiv$ effective principal quantum number

$l^* = l + d \equiv$ effective orbital angular momentum quantum number

d = modifies the integer quantum numbers n and l

$L_{n-l-1}^{2l^*+1}\left(\frac{2Z^*r}{n^*}\right)$ = generalized Laguerre polynomial

In order to solve this radial wave function $R_{nl}(r)$, Z^*,n^* and l^* parameters must be known. These parameters are obtained by solving the following equations:

$$I = \frac{Z^{*2}}{2n^{*2}} \tag{A.3}$$

$$\langle r \rangle = \frac{3n^{*2} - l^*(l^*+1)}{2Z^*} \tag{A.4}$$

where

I = Ionization energy

$\langle r \rangle$ = expectation value for radius of weakeast bound electron

The transition probability is given by

$$A_{ij} = 2.0261 \times 10^{-6} \frac{\left(E_j - E_i\right)^3}{(2j'+1)} \times DLS \tag{A.5}$$

where

E_i, E_j = Energy levels of the initial and final states $\left(\text{cm}^{-1}\right)$

j' = total angular momentum quantum number for final state

DLS = electric dipole line strength

The stimulated emission cross sections in Tables 5.5 and 5.6 are derived from

$$\sigma_{SE}(v) = A_{ij}\frac{\lambda^2}{8\pi n^2}g(v) \tag{A.6}$$

where

A_{ij} = Transition probability $\left(s^{-1}\right)$ from Equation A.5

λ = center emission wavelength

n = index of refraction

$g(v)$ = line-shape function (s)

The line-shape function, $g(v)$, is given by

$$g(v) = \left(\frac{4ln(2)}{\pi}\right)^2 \frac{1}{\Delta v_D} \tag{A.7}$$

where

$$\Delta v_D = \left(\frac{8k_bTln(2)}{M_{Cs}c^2}\right)v_0$$

k_b = Boltzmann constant

T = Temperature of the vapor cell

M_{Cs} = Mass of Cs atom

c = speed of light

v_0 = center frequency of the transition

Bibliography

[1] Akulshin, Alexander, Dmitry Budker, and Russell McLean. "Directional infrared emission resulting from cascade population inversion and four-wave mixing in Rb vapor." *Optics letters*, 39(4):845–8, 2014. ISSN 1539-4794. URL http://www.ncbi.nlm.nih.gov/pubmed/24562222.

[2] Akulshin, Alexander, Christopher Perrella, Gar-Wing Truong, Russell McLean, and Andre Luiten. "Frequency evaluation of collimated blue light generated by wave mixing in Rb vapour". *Journal of Physics B: Atomic, Molecular and Optical Physics*, 45(24):245503, 2012. ISSN 0953-4075. URL http://stacks.iop.org/0953-4075/45/i=24/a=245503?key=crossref.7955357b03c598de6165aeb7627c129d.

[3] Akulshin, Alexander M., Russell J. McLean, Andrei I. Sidorov, and Peter Hannaford. "Coherent and collimated blue light generated by four-wave mixing in Rb vapour". *Optics Express*, 17(25):22861, 2009. ISSN 1094-4087.

[4] Alcock, C. B., V. P. Itkin, and M. K. Horrigan. "Vapour Pressure Equations for the Metallic Elements: 2982500K". *Canadian Metallurgical Quarterly*, 23(3):309–313, 1984. ISSN 0008-4433. URL http://www.tandfonline.com/doi/full/10.1179/cmq.1984.23.3.309.

[5] Auzinsh, M., R. Ferber, F. Gahbauer, A. Jarmola, L. Kalvans, and A. Atvars. "Cascade coherence transfer and magneto-optical resonances at 455 nm excitation of cesium". *Optics Communications*, 284(12):2863–2871, 2011. ISSN 00304018.

[6] Banerjee, A, D Das, and V Natarajan. "Absolute frequency measurements of the D1 lines in 39K, 85Rb, and 87Rb with ≈ 0.1 ppb uncertainty". *Europhysics Letters*, 65(2):172, 2004.

[7] Barmashenko, B D, S Rosenwaks, and M C Heaven. "Static diode pumped alkali lasers: Model calculations of the effects of heating, ionization, high electronic excitation and chemical reactions". *Optics Communications*, 292(0):123–125, jan 2013. ISSN 0030-4018. URL http://www.sciencedirect.com.wrs.idm.oclc.org/science/article/pii/S0030401812013612.

[8] Barwood, GP, P Gill, and WRC Rowley. "Frequency measurements on optically narrowed Rb-stabilised laser diodes at 780 nm and 795 nm". *Applied Physics B*, 53(3):142–147, 1991.

[9] Beach, Raymond J., William F. Krupke, V. Keith Kanz, Stephen A. Payne, Mark A. Dubinskii, and Larry D. Merkle. "End-pumped continuous-wave alkali vapor lasers: experiment, model, and power scaling". *Journal of the Optical Society of America B*, 21(12):2151, 2004. ISSN 0740-3224. URL https://www.osapublishing.org/abstract.cfm?URI=josab-21-12-2151.

[10] Beahn, TJ, WJ Condell, and HI Mandelberg. "Excitation-Transfer Collisions between Rubidium and Helium Atoms". *Physical Review*, 141(1):83, 1966.

[11] Berends, R. W., W. Kedzierski, and L. Krause. "52P1 2-52P3 2 fine-structure mixing in potassium atoms induced by collisions with noble gases". *Journal of Quantitative Spectroscopy and Radiative Transfer*, 37(2):157–164, 1987. ISSN 00224073.

[12] Bieniak, B., K. Fronc, S. Gateva-Kostova, M. Głódź, V. Grushevsky, J. Klavins, K. Kowalski, A. Rucińska, and J. Szonert. "Excitation transfer between the rubidium 52D fine-structure levels in collisions with ground-state rubidium atoms: Experiment and theory". *Physical Review A*, 62(2):022720, 2000. ISSN 1050-2947. URL https://link.aps.org/doi/10.1103/PhysRevA.62.022720.

[13] Bischel, W K, B E Perry, and D R Crosley. "Detection of fluorescence from O and N atoms induced by two-photon absorption." *Applied optics*, 21(8):1419–1429, 1982. ISSN 0003-6935.

[14] Boesten, HMJM, CC Tsai, JR Gardner, DJ Heinzen, and BJ Verhaar. "Observation of a shape resonance in the collision of two cold Rb 87 atoms". *Physical Review A*, 55(1):636, 1997.

[15] Bogachev, A V, Sergey G Garanin, A M Dudov, V A Eroshenko, S M Kulikov, G T Mikaelian, V A Panarin, V O Pautov, A V Rus, and Stanislav A Sukharev. "Diode-pumped caesium vapour laser with closed-cycle laser-active medium circulation". *Quantum Electronics*, 42(2):95, 2012.

[16] Boyd, Robert W. *Nonlinear Optics, 3rd Edition*. Academic Press, 3rd edition, 2008. ISBN 9780123694706.

[17] Bradley, Michael P, James V Porto, Simon Rainville, James K Thompson, and David E Pritchard. "Penning Trap Measurements of the Masses of C 133 s, R 8 7, 8 5 b, and N 23 a with Uncertainties 0.2 ppb". *Physical Review Letters*, 83(22):4510, 1999.

[18] Brown, Kirk C., Edward J. Hurd, Jeremy C. Holtgrave, and Glen P. Perram. "Stimulated electronic Raman and hyper-Raman scattering in potassium vapor". *Optics Communications*, 309:21–25, 2013. ISSN 00304018.

[19] Brown, Kirk C and Glen P Perram. "Cesium laser operating in the blue by direct optical excitation of the 7(2)P(3/2) state". *Proceedings of SPIE*, 7915:791507, 2011. ISSN 0277-786X; 978-0-81948-452-9.

[20] Brown, Kirk C. and Glen P. Perram. "Spin-orbit relaxation and quenching of cesium 7 ^2P in mixtures of helium, methane, and ethane". *Physical Review A*, 85:022713, Feb 2012.

[21] Brown, Kirk C. and Glen P. Perram. "Spin-orbit relaxation and quenching of cesium 72P in mixtures of helium, methane, and ethane". *Physical Review A - Atomic, Molecular, and Optical Physics*, 85(2):022713, 2012. ISSN 10502947. URL http://link.aps.org/doi/10.1103/PhysRevA.85.022713.

[22] Brown, Kirk C. and Glen P. Perram. "Demonstration of a 459-nm pulsed, optically pumped cesium vapor laser". *Optics Communications*, 300:51–57, 2013. ISSN 00304018.

[23] Caplan, William D. "Requirements for laser countermeasures against imaging seekers", 2014. URL http://proceedings.spiedigitallibrary.org/proceeding.aspx?doi=10.1117/12.2067264.

[24] Cataliotti, F S, C Fort, F S Pavone, and M Inguscio. "Doppler-free excitation of the weak 6S1/2-8P1/2 cesium transition at 389 nm". *Zeitschrift für Physik D Atoms, Molecules and Clusters*, 38(1):31–33, 1996. ISSN 0178-7683. URL http://dx.doi.org/10.1007/s004600050059.

[25] Çelik, G. and Å AteÅ. "Calculations of transition probabilities for some excited levels of Na I". *Acta Physica Polonica A*, 113(6):1619–1627, 2008. ISSN 05874246. URL http://przyrbwn.icm.edu.pl/APP/PDF/113/a113z606.pdf.

[26] Çelik, Gültekin and Åule AteÅ. "Investigation of the effects of expectation values for radii on the determination of transition probabilities using WBEPM theory". *Journal of Astrophysics and Astronomy*, 29(3-4):367–378, 2008. ISSN 0250-6335. URL http://link.springer.com/10.1007/s12036-008-0049-3.

[27] Chapman, G. D. and L. Krause. "Sensitized Fluorescence in Vapors of Alkali Metals Viii. Energy Transfer Between the 4 2P Levels in Potassium Induced By Inelastic Collisions". *Can. J. Phys.*, 44(4):753–768, 1966.

[28] Chaves De Souza Segundo, P., I. Hamdi, M. Fichet, D. Bloch, and M. Ducloy. "Selective reflection spectroscopy on the UV third-resonance line of Cs: Simultaneous probing of a van der Waals atom-surface interaction sensitive to far IR couplings and interatomic collisions". *Laser physics*, 17(7):983–992, 2007. ISSN 1054-660X. URL http://www.springerlink.com/index/10.1134/S1054660X07070134{%}5Cnhttp://www.springerlink.com/index/a73t5n27200166v4.pdf.

[29] Chen, F E I C, D X U Ongdong, Q Ikun P An, Y H E Ang, and D Y U Eyang. "Theoretical study on the characteristics of intracavity frequency doubling of a diode-pumped cesium vapor laser". 33(12):2445–2449, 2016.

[30] Chen, Fei, Qikun Pan, Fei Gao, Dongdong Xu, Yang He, Deyang Yu, and Kuo Zhang. "Repetition Operation of a 447.3 nm BlueViolet Laser by Intracavity Frequency Doubling of an LD-Pumped Cesium Vapor Laser". *Journal of Russian Laser Research*, 38(6):564–568, 2017. ISSN 15738760.

[31] Correll, Tiffany L., Vlasta Horvatic, Nicoló Omenetto, James D. Winefordner, and Cedomil Vadla. "Experimental evaluation of the cross-sections for the Cs(6D) Cs(7PJ) and Cs(6D5 / 2) Cs(6D3 / 2) collisional transfer processes induced by He and Ar". *Spectrochimica Acta - Part B Atomic Spectroscopy*, 61(6):623–633, 2006. ISSN 05848547.

[32] Cowan, R. D. *The theory of atomic structure and spectra*. Los Alamos Series in Basic and Applied Sciences. University of California Press, 1981. ISBN 0-520-03821 -5. URL http://books.google.ru/books?id=tHOXLrXkJRgC.

[33] Cuvellier, J., P. R. Fournier, F. Gounand, J. Pascale, and J. Berlande. "Inelastic collisions involving excited cesium atoms at thermal energies". *Physical Review A*, 11(3):846–856, 1975. ISSN 10502947.

[34] Czajkowski, M., E. Lisicki, and N. Hedgecock. "Total out-of-doublet quenching cross-sections for Cs-atoms in n2S12, n2DJ and n2FJ states in collision with Xe atoms". *Journal of Quantitative Spectroscopy and Radiative Transfer*, 41(2):85–91, feb 1989. ISSN 00224073. URL http://www.sciencedirect.com/science/article/pii/0022407389901295.

[35] Davila, Ricardo C. and Glen P. Perram. "Spin-orbit relaxation of cesium 7 2D in mixtures of helium and argon". *Physical Review A - Atomic, Molecular, and Optical Physics*, 93(3):033418, 2016. ISSN 10941622. URL http://link.aps.org/doi/10.1103/PhysRevA.93.033418.

[36] Davila, Ricardo C., Glen P. Perram, and Ben Eshel. "Time-resolved fine structure mixing of cesium 82D induced by helium and argon". *Journal of Physics B: Atomic, Molecular and Optical Physics*, 50(22):225204, 2017. ISSN 13616455. URL http://stacks.iop.org/0953-4075/50/i=22/a=225204.

[37] Elward-Berry, Julianne and Michael J. Berry. "Lithium [Li(22P1/2,3/2)] fine structure transitions induced by collisions with noble gas atoms". *The Journal of Chemical Physics*, 72(8):4500, 1980. ISSN 00219606. URL http://link.aip.org/link/JCPSA6/v72/i8/p4500/s1{&}Agg=doi.

[38] Eshel, Ben, Joseph A. Cardoza, David E. Weeks, and Glen P. Perram. "Role of adiabaticity in controlling alkali-metal fine-structure mixing induced by rare gases". *Physical Review A*, 95(4):042708, apr 2017. ISSN 24699934.

[39] Eshel, Ben, David E. Weeks, and Glen P. Perram. "The role of adiabaticity in alkali atom-fine structure mixing". *SPIE Photonics West 2014-LASE: Lasers and Sources*, 8962:896207, 2014. ISSN 0277-786X. URL http://proceedings.spiedigitallibrary.org/proceeding.aspx?doi=10.1117/12.2045115.

[40] Gai, Baodong, Rui Cao, Xusheng Xia, Shu Hu, Jinbo Liu, Jingwei Guo, Yannan Tan, Wanfa Liu, Yuqi Jin, and Fengting Sang. "Modulation of a double-line

frequency up-conversion process in cesium vapor". *Applied Physics B: Lasers and Optics*, 122(6):165, 2016. ISSN 09462171. URL http://link.springer.com/10.1007/s00340-016-6438-4.

[41] Gallagher, Alan. "Rubidium and cesium excitation transfer in nearly adiabatic collisions with inert gases". *Physical Review*, (v):88, 1968. URL http://journals.aps.org/pr/abstract/10.1103/PhysRev.172.88.

[42] Gao, F., F. Chen, J. J. Xie, D. J. Li, L. M. Zhang, G. L. Yang, J. Guo, and L. H. Guo. "Review on diode-pumped alkali vapor laser". *Optik*, 124(20):4353–4358, 2013. ISSN 00304026. URL http://www.sciencedirect.com/science/article/pii/S0030402613002234.

[43] Ge, Lun, Weihong Hua, Hongyan Wang, Zining Yang, and Xiaojun Xu. "Study on photoionization in a rubidium diode-pumped alkali laser gain medium with the optogalvanic method". *Optics letters*, 38(2):199–201, 2013. ISSN 1539-4794.

[44] Gearba, M A, J F Sell, B M Patterson, R Lloyd, J Plyler, and R J Knize. "Temperature dependence of Rb 5P fine-structure transfer induced by He-4 collisions". *Optics Letters*, 37(10):1637–1639, 2012. ISSN 0146-9592.

[45] Gutterres, RF, C Amiot, A Fioretti, C Gabbanini, M Mazzoni, and O Dulieu. "Determination of the ^{87}Rb 5p state dipole matrix element and radiative lifetime from the photoassociation spectroscopy of the Rb_2 $0_g^-(P_{3/2})$ long-range state". *Physical Review A*, 66(2):024502, 2002.

[46] Hager, G. D. and G. P. Perram. "A three-level analytic model for alkali metal vapor lasers: Part I. Narrowband optical pumping". *Applied Physics B: Lasers and Optics*, 101(1-2):45–56, 2010. ISSN 09462171.

[47] Hager, Gordon D. and Glen P. Perram. "A three level analytic model for alkali vapor lasers". *AIP Conference Proceedings*, 1278:472–481, 2010. ISSN 0094243X.

[48] Hager, Gordon D. and Glen P. Perram. "A three-level model for alkali metal vapor lasers. Part II: Broadband optical pumping". *Applied Physics B: Lasers and Optics*, 112(4):507–520, 2013. ISSN 09462171. URL http://dx.doi.org/10.1007/s00340-013-5371-z.

[49] Hamadani, S. M., J. A D Stockdale, R. N. Compton, and M. S. Pindzola. "Two-photon resonant four-wave mixing and multiphoton ionization of cesium in a heat-pipe oven". *Physical Review A*, 34(3):1938–1943, sep 1986. ISSN 10502947. URL https://link.aps.org/doi/10.1103/PhysRevA.34.1938.

[50] Hecht, J. *The Laser Guidebook, 1992*. McGraw-Hill Education, 1992.

[51] Hecht, Jeff. *Understanding lasers: an entry-level guide*, volume 21. John Wiley & Sons, 2011.

[52] Huennekens, J., Z. Wu, and T. G. Walker. "Ionization, excitation of high-lying atomic states, and molecular fluorescence in Cs vapor excited at =455.7 and 459.4 nm". *Physical Review A*, 31(1):196–209, jan 1985. ISSN 10502947. URL http://pra.aps.org/abstract/PRA/v31/i1/p196{_}1http://link.aps.org/doi/10.1103/PhysRevA.31.196.

[53] Hugon, M, F Gounand, P R Fournier, and J Berlande. "Collisional processes of rubidium in the S and D Rydberg states with helium". *Journal of Physics B: Atomic and Molecular Physics*, 13(8):1585–1599, apr 1980. ISSN 0022-3700. URL http://stacks.iop.org/0022-3700/13/i=8/a=013?key=crossref.fb1e2a19d5bb761a6108b4a79563a7e4.

[54] Hurd, Edward J., Jeremy C. Holtgrave, and Glen P. Perram. "Intensity scaling of an optically pumped potassium laser". *Optics Communications*, 357:63–66, 2015. ISSN 00304018.

[55] Jackowska, I. and M. Lukaszewski. "Cross sections for J mixing in 8D and 9D states of caesium in collisions with noble-gas atoms", 1990. URL http://stacks.iop.org/0953-4075/23/i=12/a=018.

[56] James, D.L. and M.A. Welsh. "State of the Air Force press briefing by Secretary James and General Welsh in the Pentagon Briefing Room [Interview]", 2015.

[57] Jordan, J. A. and P. A. Franken. "Collision-induced mixing in the first excited states of sodium and potassium". *Physical Review*, 142(1):20–25, feb 1966. ISSN 0031899X. URL https://link.aps.org/doi/10.1103/PhysRev.142.20.

[58] Jung, M., T. Riesbeck, J. Schmitz, T. Baumgärtel, K. Ludewigt, and A. Graf. "High energy laser demonstrators for defense applications". 10254:1025416, 2017. ISSN 1996756X. URL http://proceedings.spiedigitallibrary.org/proceeding.aspx?doi=10.1117/12.2254021.

[59] Kiran Kumar, P. V., M. Sankari, and M. V. Suryanarayana. "Hyperfine structure of the 7d 2D3/2 level in cesium measured by Doppler-free two-photon spectroscopy". *Physical Review A - Atomic, Molecular, and Optical Physics*, 87(1):012503, 2013. ISSN 10502947. URL http://link.aps.org/doi/10.1103/PhysRevA.87.012503.

[60] Kissel, Heiko, Bernd Köhler, and Jens Biesenbach. "High-power diode laser pumps for alkali lasers (DPALs)". *Proceedings of SPIE*, 8241:82410Q, 2012. ISSN 0277786X. URL http://link.aip.org/link/PSISDG/v8241/i1/p82410Q/s1{&}Agg=doi.

[61] Klennert, W. and Sandoval, A.J. and Hostutler, D.A. "Development of a compact heat pipe oven for optically pumped alkali laser research". *Energy*, 4:245–252, feb 2012. ISSN 1751-8113. URL http://arxiv.org/abs/1011.1669http://dx.doi.org/10.1088/1751-8113/44/8/085201http://stacks.iop.org/1751-8121/44/i=8/a=085201?key=crossref.abc74c979a75846b3de48a5587bf708f.

[62] Knize, R.J., B.V. Zhdanov, and M.K. Shaffer. "Photoionization in alkali lasers", 2011. URL https://www.osapublishing.org/oe/abstract.cfm?uri=oe-19-8-7894.

[63] Koenning, Tobias, Dan Mccormick, David Irwin, Dean Stapleton, Tina Guiney, and Steve Patterson. "DPAL pump system exceeding 3kW at 766nm and 30 GHz bandwidth". 1(520):1–7, 2016. ISSN 1996756X.

[64] Köhler, Bernd, Andreas Unger, Tobias Kindervater, Simon Drovs, Paul Wolf, Ralf Hubrich, Anna Beczkowiak, Stefan Auch, Holger Müntz, and Jens Biesenbach. "Wavelength stabilized multi-kW diode laser systems". *Spie Lase*, 9348(0):93480Q–93480Q, 2015. ISSN 1996756X. URL http://dx.doi.org/10.1117/12.2079428.

[65] Konefał, Z. "Observation of collision induced processes in rubidium-ethane vapour". *Optics Communications*, 164(1):95–105, 1999. ISSN 00304018.

[66] Krause, L. "Collisional Excitation Transfer Between the $^2P_{1/2}$ and $^2P_{3/2}$ Levels in Alkali Atoms". *Applied Optics*, 5(9):1375–1382, 1966.

[67] Krause, L. "Sensitized Fluorescence and Quenching". *The Excited State in Chemical Physics*, volume 28, 267–316. John Wiley & Sons, Inc., 2006. ISBN 9780470143803. URL http://dx.doi.org/10.1002/9780470143803.ch4.

[68] Krause, L., M. Czajkowski, D. A. Mcgillis, and L. Krause. "Sensitized Fluorescence in Vapors of Alkali Metals". *Canadian Journal of Physics*, 44(361):91–103, jan 1966. ISSN 0008-4204. URL http://www.nrcresearchpress.com/doi/abs/10.1139/p66-007.

[69] Krupke, W F, R J Beach, V K Kanz, S A Payne, and J T Early. "New class of cw high-power diode-pumped alkali lasers (DPALs)". *Proceedings of SPIE*, 5448:7–17, 2004. ISSN 0277-786X; 0-8194-5371-4.

[70] Krupke, William F. "Diode Pumped Alkali Laser, US Patent No. 6,643,311 B2", 2003.

[71] Krupke, William F. "Diode pumped alkali lasers (DPALs) - A review (rev1)". *Progress in Quantum Electronics*, 36(1):4–28, 2012.

[72] Krupke, William F., Raymond J. Beach, V. Keith Kanz, and Stephen A. Payne. "Resonance transition 795-nm rubidium laser". *Optics Letters*, 28(23):2336, dec 2003. ISSN 0146-9592. URL https://www.osapublishing.org/abstract.cfm?URI=ol-28-23-2336.

[73] Lee, Y C, Y H Chang, Y Y Chang, Y Y Chen, C C Tsai, and H C Chui. "Hyperfine coupling constants of cesium 7D states using two-photon spectroscopy". *Applied Physics B-Lasers and Optics*, 105(2):391–397, 2011. ISSN 0946-2171.

[74] Lide, David R. "CRC handbook of physics and chemistry", 2001.

[75] Liu, Y and P E G Baird. "Measurement of the caesium 6S 1/2 8P 1/2 transition frequency". *Applied Physics B (Lasers and Optics), Springer Verlag*, 572(Issue 4):567–572, 2000. URL http://nthur.lib.nthu.edu.tw/dspace/handle/987654321/55853.

[76] Lukaszewski, M and I Jackowska. "Fine-Structure Mixing in the 9d State of Cesium Induced in Collisions with Noble-Gas Atoms". *Journal of Physics B-Atomic Molecular and Optical Physics*, 21(21):L659–L664, 1988. ISSN 0953-4075.

[77] Lukaszewski, M and I Jackowska. "J mixing in nD (n = 10-14) states of caesium induced in collisions with noble-gas atoms". *J. Phys. B: At. Mol. Opt. Phys.*, 24(8):2047–2057, 1991. ISSN 0953-4075.

[78] Mallory, T. R., W. Kedzierski, J. B. Atkinson, and L. Krause. "92D fine-structure mixing in rubidium by collisions with ground-state Rb and noble-gas atoms". *Physical Review A*, 38(11):5917–5920, 1988. ISSN 10502947.

[79] Marek, J. "Radiative lifetime of the 8S, 9S and 7D levels of CsI". *Physics Letters A*, 60(3):190–192, 1977. ISSN 0375-9601.

[80] Marek, J. and M. Ryschka. "Lifetime measurements of F-levels of Cs using partially superradiant population". *Physics Letters A*, 74(1-2):51–54, oct 1979. ISSN 03759601. URL http://linkinghub.elsevier.com/retrieve/pii/0375960179905802.

[81] Mccormick, Dan, David Irwin, Dean Stapleton, Joe Braker, Tobias Koenning, Steve Patterson, and A Power. "Ultra-narrow spectral linewidth diode lasers for the pumping of alkalis". *2015 IEEE High Power Diode Lasers and Systems Conference (HPD)*, volume 85747, 25–26. oct 2015. ISBN 9781467391788. ISSN 2379-0385.

[82] Meijer, T, J D White, B Smeets, M Jeppesen, and R E Scholten. "Blue five-level frequency-upconversion system in rubidium." *Optics letters*, 31(7):1002–1004, 2006. ISSN 0146-9592.

[83] Mestdagh, J M, J Berlande, J Cuvellier, P de Pujo, and A Binet. "Fine-structure transitions in K (4P) induced by rare gases and diatomic molecules". *J. Phys. B: At. Mol. Phys.*, 15(3):439–450, 1982.

[84] Moran, Paul J., Ryan M. Richards, Christopher A. Rice, and Glen P. Perram. "Near infrared rubidium 62P3/2,1/2???62S1/2 laser". *Optics Communications*, 374:51–57, 2016. ISSN 00304018.

[85] Munster, P and J Marek. "Determination of cross sections of excitation transfer Rb (62P) between the fine-structure components of CS (72P) and Rb (72P) induced by collisions with rare-gas atoms". *J. Phys. B: At. Mol. Phys.*, 14(6):1009–1018, 1981.

[86] Nahar, Sultana Nurun and Steven T. Manson. "Photoionization of the 7d excited state of cesium". *Physical Review A*, 40(11):6300–6302, dec 1989. ISSN 10502947. URL https://link.aps.org/doi/10.1103/PhysRevA.40.6300.

[87] Newton, James H. and James F. Young. "Infrared Image Upconversion Using Two-Photon Resonant Optical Four-Wave Mixing in Alkali Metal Vapors". *IEEE Journal of Quantum Electronics*, 16(3):268–276, mar 1980. ISSN 15581713. URL http://ieeexplore.ieee.org/document/1070485/.

[88] Nikitin, E. E. "Theory of Nonadiabatic Collision Processes Including Excited Alkali Atoms". *Advances in Chemical Physics*, 317–377. John Wiley & Sons, Inc., 1975. ISBN 9780470143803. URL http://doi.wiley.com/10.1002/9780470143803.ch5.

[89] Oliker, Benjamin Q, John D Haiducek, David A Hostutler, Greg A Pitz, Wolfgang Rudolph, and Timothy J Madden. "Simulation of Deleterious Processes in a Static-Cell Diode Pumped Alkali Laser". *Proceedings of SPIE*, 8962:89620B–89620B, 2014. ISSN 0277-786X; 978-0-8194-9875-5.

[90] Pascale, J. "Total cross sections for Na(32P1/232P3/2) + rare gas collisions". *The Journal of Chemical Physics*, 64(9):3538, 1976. ISSN 00219606. URL http://scitation.aip.org/content/aip/journal/jcp/64/9/10.1063/1.432721.

[91] Passerat De Silans, Thierry, Isabelle Maurin, Athanasios Laliotis, Pedro Chaves De Souza Segundo, and Daniel Bloch. "Extra sub-Doppler lines in the vicinity of the third-resonance 6S-8P transition of atomic Cs attributed to optically induced Cs dimers". *Physical Review A - Atomic, Molecular, and Optical Physics*, 83(4):43402, 2011. ISSN 10502947.

[92] Perram, G. P., S. J. Cusumano, R. L. Hengehold, and S. T. Fiorino. *An Introduction to Laser Weapons Systems*. Directed Energy Professional Society, 2010. ISBN 097936874X 9780979368745. URL https://books.google.com/books?id=0jLUZwEACAAJ.

[93] Perram, Glen P. "Alternative Wavelengths for Optically Pumped Alkali Lasers". *Proceedings of SPIE*, 8381:838109, 2012. ISSN 0277-786X; 978-0-8194-9059-9.

[94] Perram, Glen P. "Wavelength diversity in optically pumped alkali vapor lasers", 2017. URL http://proceedings.spiedigitallibrary.org/proceeding.aspx?doi=10.1117/12.2256256.

[95] Perram, Glen P, Salvatore J Cusumano, Robert L Hengehold, and Steven T Fiorino. *An Introduction to Laser Weapon Systems*. Directed Energy Professional Society, 2010.

[96] Perram, Glen P., Michael A. Marciniak, and Matthew Goda. "High-energy laser weapons: technology overview", 2004. URL http://proceedings.spiedigitallibrary.org/proceeding.aspx?articleid=843845.

[97] Petersen, A. B. and R. J. Lane. "A diode-pumped Rb laser at 398 nm". volume 6871, 68711Q. 2008. ISBN 9780819470461. ISSN 0277786X. URL http://proceedings.spiedigitallibrary.org/proceeding.aspx?doi=10.1117/12.773979.

[98] Pimbert, M. "Transfert d'excitation électronique, par collision atomique, entre niveaux élevés d'un atome de césium". *Journal de Physique*, 33(4):331–343, 1972. ISSN 0302-0738. URL http://www.edpsciences.org/10.1051/jphys:01972003304033100.

[99] Pitre, Bruce, A G A Rae, and L Krause. "Sensitized Fluorescence in Vapor of Alkali Metals: VI. Emergy Transfer in Collisions Between Rubidium and Inert Gas Atoms". *Canadian Journal of Physics*, 44(4):731–740, apr 1966. ISSN 0008-4204. URL http://dx.doi.org/10.1139/p66-063.

[100] Pitz, Greg A, Charles D Fox, and Glen P Perram. "Pressure broadening and shift of the cesium D_2 transition by the noble gases and N_2, H_2, HD, D_2, CH_4, C_2H_6, CF_4, and He_3 with comparison to the D_1 transition". *Physical Review A*, 82(4):042502, 2010.

[101] Pitz, Greg A, Sara Glass, Brian Kamer, Wade L Klennert, and David A Hostutler. "Atmospheric propagation properties of various laser system". *Proceedings of SPIE*, 8380:83800V–83800V, 2012. ISSN 0277-786X; 978-0-8194-9058-2.

[102] Pitz, Greg A., Donald M. Stalnaker, Eric M. Guild, Benjamin Q. Oliker, Paul J. Moran, Steven W. Townsend, and David A. Hostutler. "Advancements in flowing diode pumped alkali lasers". *Proc. SPIE*, 9729:972902, 2016. ISSN 1996756X. URL http://proceedings.spiedigitallibrary.org/proceeding.aspx?doi=10.1117/12.2217078.

[103] Pitz, Greg A, Clifford V Sulham, E Acosta, and Glen P Perram. "Two red photon absorption in alkalis producing infrared and blue beams". *AIAA Plasmadynamics and Lasers Conference, 41st*, volume 4876. 2010. ISBN 9781600867453.

[104] Rabinowitz, P., S. Jacobs, and G. Gould. "Continuous Optically Pumped Cs Laser". *Applied Optics*, 1(4):513, 1962. ISSN 0003-6935. URL http://ao.osa.org/abstract.cfm?URI=ao-1-4-513.

[105] Rafac, R. J., C. E. Tanner, A. E. Livingston, K. W. Kukla, H. G. Berry, and C. A. Kurtz. "Precision lifetime measurements of the 6p 2P1_2 3_2 states in atomic cesium". *Physical Review A*, 50(3):R1976, 1994.

[106] Rice, Christopher A and Glen P Perram. "Atmospheric transmission for cesium DPAL using TDLAS", 2012. URL http://dx.doi.org/10.1117/12.906394.

[107] Rotondaro, Matthew D and Glen P Perram. "Role of rotational-energy defect in collisional transfer between the 52P1/2,3/2 levels in rubidium". *Physical Review A*, 57(5):4045–4048, 1998.

[108] Sasso, A., W. Demtröder, T. Colbert, C. Wang, E. Ehrlacher, and J. Huennekens. "Radiative lifetimes, collisional mixing, and quenching of the cesium 5DJ levels". *Physical Review A*, 45(3):1670–1683, 1992. ISSN 10502947.

[109] Schawlow, A. L. and C. H. Townes. "Infrared and Optical Masers". *Physical Review*, 112(6):1940–1949, 1958. ISSN 0031-899X. URL http://link.aps.org/doi/10.1103/PhysRev.112.1940.

[110] Seaton, Mj. "Quantum defect theory". *Reports on Progress in Physics*, 46(2):167–257, 1983. ISSN 0034-4885. URL http://iopscience.iop.org/0034-4885/46/2/002.

[111] Sell, J F, M a Gearba, B D DePaola, and R J Knize. "Collimated blue and infrared beams generated by two-photon excitation in Rb vapor". *Optics Letters*, 39(3):528, 2014. ISSN 0146-9592. URL http://www.ncbi.nlm.nih.gov/pubmed/24487857{%}5Cnhttps://www.osapublishing.org/abstract.cfm?URI=ol-39-3-528.

[112] Sell, J F, M A Gearba, B M Patterson, D Byrne, G Jemo, T C Lilly, R Meeter, and R J Knize. "Collisional excitation transfer between Rb(5P) states in 50-3000 Torr of He-4". *Journal of Physics B-Atomic Molecular and Optical Physics*, 45(5):55202, 2012. ISSN 0953-4075.

[113] Sharma, A., N. D. Bhaskar, Y. Q. Lu, and W. Happer. "Continuous-wave mirrorless lasing in optically pumped atomic Cs and Rb vapors". *Applied Physics Letters*, 39(3):209–211, 1981. ISSN 00036951. URL http://scitation.aip.org/content/aip/journal/apl/39/3/10.1063/1.92681.

[114] Siara, I, E S Hrycyshyn, and L Krause. "Sensitized fluorescence in vapors of alkali atoms. XIII. 62P1/2-62P3/2 excitation transfer in rubidium, induced in collisions with noble gas atoms". *Can. J. Phys*, 50(16):1826–1832, 1972.

[115] Siara, I N, H S Kwong, and L Krause. "Sensitized Fluorescence in Vapors of Alkali Atoms XIV. Temperature Dependence of Cross Sections for 72P1/272P3/2 Mixing in Cesium, Induced in Collisions with Noble Gas Atoms". *Canadian Journal of Physics*, 52(11):945–949, jun 1974. ISSN 0008-4204. URL http://www.nrcresearchpress.com/doi/abs/10.1139/p74-129.

[116] Simsarian, JE, LA Orozco, GD Sprouse, and WZ Zhao. "Lifetime measurements of the 7 p levels of atomic francium". *Physical Review A*, 57(4):2448, 1998.

[117] Sorokin, P. P., J. J. Wynne, and J. R. Lankard. "Tunable coherent ir source based upon four-wave parametric conversion in alkali metal vapors". *Applied Physics Letters*, 22(7):342–344, 1973. ISSN 00036951.

[118] Steck, Daniel A. "Cesium D Line Data". *Theoretical Division*, 4710(7):1–31, 2010. ISSN 00036951. URL papers2://publication/uuid/3652516F-351D-4309-AF4A-4EC5C8825574{%}5Cnhttp://steck.us/alkalidata/.

[119] Sulham, C. V., G. A. Pitz, and G. P. Perram. "Blue and infrared stimulated emission from alkali vapors pumped through two-photon absorption". *Applied Physics B: Lasers and Optics*, 101(1-2):57–63, 2010. ISSN 09462171.

[120] Supronowicz, J., J. B. Atkinson, and L. Krause. "Fine-structure mixing in 72D and 82D Rb atoms, induced in collisions with ground-state atoms and molecules". *Physical Review A*, 30(1):112–118, 1984. ISSN 10502947.

[121] Supronowicz, J., J. B. Atkinson, and L. Krause. "62D fine-structure mixing in rubidium induced in collisions with ground-state Rb and noble-gas atoms and with N2 molecules". *Physical Review A*, 31(4):2691–2694, apr 1985. ISSN 0556-2791. URL https://link.aps.org/doi/10.1103/PhysRevA.31.2691.

[122] Takeuchi, Eric (Daylight Solutiions Inc). "Daylight Defense Selected To Develop Ultraviolet Laser for Aircraft Survivability Equipment", 2014. URL http://www.daylightsolutions.com/about/news-releases/daylight-defense-selected.htm.

[123] Tam, A C, T Yabuzaki, S M Curry, M Hou, and W Happer. "Inelastic Cross-Sections in Cs(n2dj)+cs(62s1/2) Collisions". *Physical Review A*, 17(6):1862–1868, 1978. ISSN 1050-2947.

[124] Theodosiou, Constantine E. "Lifetimes of alkali-metalatom Rydberg states". *Physical Review A*, 30(6):2881–2909, dec 1984. ISSN 0556-2791. URL http://link.aps.org/doi/10.1103/PhysRevA.30.2881{%}5Cnhttp://pra.aps.org/abstract/PRA/v30/i6/p2881{_}1{%}5Cnhttp://pra.aps.org/pdf/PRA/v30/i6/p2881{_}1.

[125] Vadla, Cedomil, Vlasta Horvatic, and Kay Niemax. "Radiative transport and collisional transfer of excitation energy in Cs vapors mixed with Ar or He". *Spectrochimica Acta - Part B Atomic Spectroscopy*, 58(7):1235–1277, 2003. ISSN 05848547.

[126] Vasilyev, A. A., I. M. Savukov, M. S. Safronova, and H. G. Berry. "Measurement of the 6s-7p transition probabilities in atomic cesium and a revised value for the weak charge Qw". *Physical Review A*, 66(2):020101, aug 2002. ISSN 1050-2947. URL http://link.aps.org/doi/10.1103/PhysRevA.66.020101.

[127] Volz, U and H Schmoranzer. "Precision lifetime measurements on alkali atoms and on helium by beam–gas–laser spectroscopy". *Physica Scripta*, 1996(T65):48, 1996.

[128] Wang, Hongyan, Zining Yang, Weihong Hua, Xiaojun Xu, and Qisheng Lu. "Choice of alkali element for DPAL scaling, a numerical study". *Optics Communications*, 296:101–105, 2013. ISSN 00304018. URL http://dx.doi.org/10.1016/j.optcom.2013.01.025.

[129] Willers, Cornelius J and Maria S Willers. "Simulating the DIRCM engagement : component and system level performance". 8543:1–16, 2012.

[130] Wolnikowski, J., J. B. Atkinson, J. Supronowicz, and L. Krause. "7D322-7D522 excitation transfer in rubidium induced in collisions with ground-state Rb and noble-gas atoms". *Physical Review A*, 25(5):2622–2628, 1982. ISSN 10502947.

[131] Wu, Sheldon SQ, Thomas F Soules, Ralph H Page, Scott C Mitchell, V Keith Kanz, and Raymond J Beach. "Resonance transition 795-nm rubidium laser using ^{3}He buffer gas". *Optics Communications*, 281(5):1222–1225, 2008.

[132] Xu, Dongdong, Fei Chen, Jin Guo, Mingzhen Shao, and Jijiang Xie. "Investigation on 447.3 nm blue-violet laser by extra-cavity frequency doubling of a diode-pumped cesium vapor laser". *Optics and Laser Technology*, 83:119–124, 2016. ISSN 00303992. URL http://dx.doi.org/10.1016/j.optlastec.2016.04.003.

[133] Ya-Juan, Wang, Pan Bai-Liang, Zhu Qi, and Yang Jing. "A kinetic model for diode pumped Rubidium vapor laser". *Optics Communications*, 284(16-17):4045–4048, 2011. ISSN 00304018. URL http://www.sciencedirect.com/science/article/pii/S0030401811004081.

[134] Ye, Jun, Steve Swartz, Peter Jungner, and John L Hall. "Hyperfine structure and absolute frequency of the ^{87}Rb $5P_{3/2}$ state". *Optics Letters*, 21(16):1280–1282, 1996.

[135] Zameroski, Nathan D, Gordon D Hager, Wolfgang Rudolph, and David A Hostutler. "Experimental and numerical modeling studies of a pulsed rubidium optically pumped alkali metal vapor laser". *Journal of the Optical Society of America B-Optical Physics*, 28(5):8–10, 2011. ISSN 0740-3224.

[136] Zhdanov, B V and R J Knize. "Diode Pumped Alkali Lasers". *Proceedings of SPIE*, 8187:818707, 2011. ISSN 0277-786X; 978-0-81948-815-2.

[137] Zhdanov, B V, J Sell, and R J Knize. "Multiple laser diode array pumped Cs laser with 48 W output power". *Electronics Letters*, 44(9):48–49, apr 2008. ISSN 00135194.

[138] Zhdanov, Boris and R J Knize. "Diode-pumped 10 W continuous wave cesium laser." *Optics Letters*, 32(15):2167–2169, aug 2007. ISSN 0146-9592. URL http://www.ncbi.nlm.nih.gov/pubmed/17671572.

[139] Zhdanov, Boris V and Randy J Knize. "Review of alkali laser research and development". *Optical Engineering*, 52(2):21010, feb 2013. ISSN 0091-3286. URL http://dx.doi.org/10.1117/1.OE.52.2.021010.

[140] Zhdanov, Boris V., Matthew D. Rotondaro, Michael K. Shaffer, and Randall J. Knize. "Efficient potassium diode pumped alkali laser operating in pulsed mode". *Optics Express*, 22(14):17266, jul 2014. ISSN 1094-4087. URL https://www.osapublishing.org/oe/abstract.cfm?uri=oe-22-14-17266.

[141] Zhdanov, Boris V., Adam Stooke, Gregory Boyadjian, Adam Voci, and R. J. Knize. "Rubidium vapor laser pumped by two laser diode arrays". *Optics Letters*, 33(5):414, mar 2008. ISSN 0146-9592. URL https://www.osapublishing.org/abstract.cfm?URI=ol-33-5-414.

[142] Zhdanov, BV, J Sell, and RJ Knize. "Multiple laser diode array pumped Cs laser with 48 W output power". *Electronics Letters*, 44(9):582–584, 2008.

[143] Zheng, Neng Wu and Tao Wang. "Transition probabilities for Ne II". *Spectrochimica Acta - Part B Atomic Spectroscopy*, 58(7):1319–1324, 2003. ISSN 05848547. URL http://www.sciencedirect.com/science/article/pii/S0584854703000533.

[144] Zollars, B. G., H. A. Schuessler, J. W. Parker, and R. H. Hill. "Inelastic collisions between selectively excited rubidium 6D2-state atoms and noble-gas atoms: Fine-structure-state mixing". *Physical Review A*, 28(3):1329–1337, 1983. ISSN 10502947.

[145] Zweiback, Jason and William F Krupke. "28W average power hydrocarbon-free rubidium diode pumped alkali laser". *Optics Express*, 18(2):1444, jan 2010. ISSN 1094-4087. URL https://www.osapublishing.org/oe/abstract.cfm?uri=oe-18-2-1444.

REPORT DOCUMENTATION PAGE

Form Approved
OMB No. 0704–0188

1. REPORT DATE *(DD–MM–YYYY)*	2. REPORT TYPE	3. DATES COVERED *(From — To)*
22–03–2018	Dissertation	Sept 2012–Mar 2018

4. TITLE AND SUBTITLE

Two-Photon Excitation of Cesium Alkali Metal Vapor 7^2D, 8^2D Kinetics and Spectroscopy

5a. CONTRACT NUMBER

5b. GRANT NUMBER

5c. PROGRAM ELEMENT NUMBER

6. AUTHOR(S)

Davila, Ricardo C., Civilian, USAF

5d. PROJECT NUMBER

5e. TASK NUMBER

5f. WORK UNIT NUMBER

7. PERFORMING ORGANIZATION NAME(S) AND ADDRESS(ES)

Air Force Institute of Technology
Graduate School of Engineering and Management (AFIT/EN)
2950 Hobson Way
Wright-Patterson AFB, OH 45433-7765

8. PERFORMING ORGANIZATION REPORT NUMBER

AFIT-ENP-DS-18-M-076

9. SPONSORING / MONITORING AGENCY NAME(S) AND ADDRESS(ES)

Missile Defense Agency (MDA)
Bldg. 5222, Martin Road
Redstone Arsenal, AL 35898-0001

10. SPONSOR/MONITOR'S ACRONYM(S)

11. SPONSOR/MONITOR'S REPORT NUMBER(S)

12. DISTRIBUTION / AVAILABILITY STATEMENT

DISTRIBUTION STATEMENT A:
APPROVED FOR PUBLIC RELEASE; DISTRIBUTION UNLIMITED

13. SUPPLEMENTARY NOTES

14. ABSTRACT

Pulsed excitation on the two-photon Cs $6^2S_{1/2} \rightarrow 7^2D_{3/2,5/2}$ transition results in time-resolved fluorescence at 697 *nm* and 672 *nm*. The rates for fine structure mixing between the $7^2D_{3/2,5/2}$ states have been measured for helium and argon rare gas collision partners. The mixing rates are very fast, $1.26 \pm 0.05 \times 10^{-9}$ $cm^3/(atom\ sec)$ for He and $1.52 \pm 0.05 \times 10^{-10}$ $cm^3/(atom\ sec)$ for Ar, driven by the small energy splitting and large radial distribution for the valence electron. The quenching rates are considerably slower, $6.84 \pm 0.09 \times 10^{-11}$ $cm^3/(atom\ sec)$ and $2.65 \pm 0.04 \times 10^{-11}$ $cm^3/(atom\ sec)$ for He and Ar, respectively. The current results are placed in context with similar rates for other alkali-rare gas collision pairs using adiabaticity arguments.
Pulsed excitation on the two-photon Cs $6\,^2S_{1/2} \rightarrow 8\,^2D_{3/2,5/2}$ transition results in time-resolved fluorescence at 601 *nm*. The rates for fine structure mixing between the $8\,^2D_{3/2,5/2}$ states have been measured for helium and argon rare gas collision partners. The mixing rates are very fast, $2.6 \pm 0.2 \times 10^{-9}$ $cm^3/(atom\ s)$ for He and $5.2 \pm 0.4 \times 10^{-10}$ $cm^3/(atom\ s)$ for Ar, about 2-3 times faster than for the Cs $7\,^2D_{5/2} \rightleftharpoons 7\,^2D_{3/2}$ relaxation. The quenching rates are also rapid, $1.07 \pm 0.04 \times 10^{-10}$ $cm^3/(atom\ s)$ and $9.5 \pm 0.7 \times 10^{-11}$ $cm^3/(atom\ s)$ for He and Ar, respectively. The rapid fine structure rates are explained by the highly impulsive nature of the collisions and the large average distance of the valence electron from the nucleus. Quenching rates (inter-multiplet transfer) are likely enhanced by the closely spaced, $9\,^2P$ levels.
Stimulated emission on the ultraviolet and blue transitions in Cs has been achieved by pumping via two-photon absorption for the pump transition $6^2S_{1/2} \rightarrow 7^2D_{5/2,3/2}$. The performance of the optically-pumped cesium vapor laser operating in ultraviolet and blue has been extended to 650 nJ/pulse for 387 nm, 1.3 μJ/pulse for 388 nm, 200 nJ/pulse for 455 nm and 500 nJ/pulse for 459 nm. Emission performance improves dramatically as the cesium vapor density is increased and no scaling limitations associated with energy pooling or ionization kinetics have been observed.

15. SUBJECT TERMS

DPAL, Cesium, Helium, Argon, Fluorescence, Rates, Temperature

16. SECURITY CLASSIFICATION OF:			17. LIMITATION OF ABSTRACT	18. NUMBER OF PAGES	19a. NAME OF RESPONSIBLE PERSON
a. REPORT	b. ABSTRACT	c. THIS PAGE			Dr. Glen P. Perram (ENP)
U	U	U	U	119	19b. TELEPHONE NUMBER *(include area code)* (937) 255-3636 x4504 Glen.Perram@afit.edu